The Planetary Science Journal, 6:51 (42pp), 2025 February https://doi.org/10.3847/PSJ/adaa78


# Rover Science Autonomy in Planetary Exploration: Field Analog Tests

Eldar Z. Noe Dobrea[1,2,15], Maria E. Banks[3], Roger N. Clark[1], David Wettergreen[4], Alberto Candela[5], Amanda Hendrix[1], Caitlin Ahrens[3,6], Ernie Bell[3,6], Abigail Breitfeld[4], Thomas F. Bristow[2], Sanlyn Buxner[1], Margaret Hansen[4], Gregory M. Holsclaw[7], Paul Knightly[8], Georgiana Kramer[1], Nandita Kumari[9], Melissa D. Lane[10], Audrey Martin[11], McKayla L. Meier[12], Ruby Patterson[13], Neil Pearson[1], Thomas Prettyman[1], Gregg A. Swayze[14], David Vaniman[1], Srinivasan Vijayarangan[4], Faith Vilas[1], and Shawn P. Wright[1]

[1] Planetary Science Institute, 1700 East Fort Lowell Rd., STE 106, Tucson, AZ 85719, USA; eldar@psi.edu
[2] M/S 245-3, NASA Ames Research Center, Moffett Blvd., Mountain View, CA 94035, USA
[3] NASA Goddard Space Flight Center, 8800 Greenbelt Rd., Greenbelt, MD 20771, USA
[4] The Robotics Institute, Carnegie Mellon University, 5000 Forbes Ave., Pittsburgh, PA 15213, USA
[5] Jet Propulsion Laboratory, 4800 Oak Grove Dr., La Cañada Flintridge, CA 91011, USA
[6] University of Maryland, College Park, MD 20742, USA
[7] University of Colorado, Boulder, CO 80309, USA
[8] Northern Arizona University, S San Francisco St., Flagstaff, AZ 86011,USA
[9] Stony Brook University, 100 Nicolls Rd., Stony Brook, NY 11794, USA
[10] Fibernetics LLC, 10 Southview Ln., Lititz, PA 17543, USA
[11] University of Central Florida, 4000 Central Florida Blvd., Orlando, FL 32816, USA
[12] University of Florida, Gainsville, Florida 32611, USA
[13] University of Houston, 4302 University Dr., Houston, TX 77004, USA
[14] U.S. Geological Survey, Federal Ave., Denver, CO 80225, USA
*Received 2024 October 8; revised 2025 January 1; accepted 2025 January 3; published 2025 February 26*

## Abstract

A strategy for planetary exploration using a rover capable of science autonomy is presented. We encoded into a rover a set of driving hypotheses pertaining to the geologic origin of a field site and equipped the rover with the instrumentation needed to measure the observables related to the hypotheses, as well as the software tools to analyze them to a relatively high level of confidence. We investigated the effects of different exploration strategies that make use of rover science autonomy and compared the operational efficiency and science yield of three geological exploration scenarios: (1) standard human-directed exploration, (2) rover-directed exploration, and (3) astronaut/rover collaborative exploration. We show that exploration with a rover capable of science autonomy is operationally more efficient than the human-directed strategy, resulting in higher rates of data collection and hence a greater science yield per command cycle. Additionally, we explored and developed astronaut/rover collaborative exploration strategies and present a basic framework for effective planetary exploration that leverages the expertise of a science team, the efficiency of a science-autonomous rover, and the contextual abilities of astronauts.

*Unified Astronomy Thesaurus concepts:* Rovers (1409)

## 1. Introduction

Current planetary robotic exploration employs, for the most part, a tight command and execution loop where a team of operators commands a robot on navigation and measurement sequences on a step-by-step basis. As the robot collects and transmits data back to Earth, scientists interpret it, identify additional measurements needed to further the exploration goals, and send new commands for the robot to execute. Consequently, rover exploration missions are characterized by frequent reformulation and replanning throughout the investigation (A. N. Hock et al. 2007).

This cycle of command, execution, data transmission, analysis, and decision-making can be slow and significantly limited by data transmission rates and volume. A complete assessment of a field area is rare, and activities are therefore decided with limited knowledge of a site. Consequently, important observations may be missed.

As autonomous systems become more capable, new paradigms for robotic exploration become more attractive. A. Candela et al. (2017, 2020) established the foundation of a new approach to robotic exploration that more accurately mimics the evolving understanding and activities of a field scientist. In this paradigm, robotic activities are not uniquely prescribed by each iteration of commands sent from the operator but are instead open-ended and responsive to ongoing observations, even without iterative feedback from an operator. Operational, data analysis, decision-making, and route-planning responsibilities are shared by the rover and the scientists/operators. In the context of human/robotic collaborative exploration, this approach transforms the existing relationship into one where humans and robots share data analysis abilities and decision-making responsibilities to fill in knowledge gaps and make discoveries.

A. Candela et al. (2017) introduced the science hypothesis map, a probabilistic structure that represents the driving hypotheses of a mission, tracking the shifting likelihoods and associated confidence of each hypothesis as the robotic explorer acquires new information. The hypothesis map enables the robot to learn from the data it acquires and interprets and to use that knowledge to plan new activities. This acceleration of analysis and decision-making improves the rate

[15] Corresponding author.

and productivity of discovery. The use of the hypothesis map in rover science autonomy was also applied and demonstrated by D. R. Thompson et al. (2018) in the context of enhancing remote-sensing data sets.

Here we built on the work of A. Candela et al. (2017, 2020) and D. R. Thompson et al. (2018) by applying the hypothesis map concept to autonomous geologic exploration. We provided a rover with the ability to constrain mineralogy using spectral measurements and to use the mineralogical interpretations to generate a probabilistic model of geologic origins, which it used to plan and execute activities for the end goal of constraining the geologic origin(s) of a field site. We compared the operational efficiency and science yield of three geologic exploration scenarios: (1) human-directed exploration, (2) rover-directed exploration, and (3) astronaut/rover collaborative exploration.

This work is a component of the research funded by the Toolbox for Research and Exploration (TREX) project, a node of NASA's Solar System Exploration Research Virtual Institute (SSERVI) (Hendrix et al. 2025, in preparation).

### 1.1. Expected Benefits

We emphasize three primary benefits to be expected from rover science autonomy. First, it improves operations efficiency by reducing the number of communication cycles. Second, it improves science yield and rate of discovery, particularly in cases where the data volume that is collected exceeds the volume that can be reasonably transmitted back to Earth. In our paradigm, the rover can acquire more data than it will transmit because it can analyze the data it acquires, use these analyses to weigh the hypotheses, and transmit the relevant subset of the data or transmit the data in order of relevance. The knowledge gained is thus constrained by the rover's data processing rate rather than the data transmission rate. Third, formalizing hypotheses (as maps) and their relationship to raw data (as a measurement model) leads to a quantifiable experimental design with direct traceability to mission objectives.

## 2. Methods

We installed onto the Carnegie Mellon Zoë rover a suite of data analysis, interpretation, and decision-making software (Section 3.1) and equipped it with UVIS-IR (0.35–14 $\mu$m) spectrometers (Section 3.3) to collect data that it could use to test the driving geological hypotheses. Field tests were performed over two field seasons at three different sites (two in year 1 in Arizona, and one in year 2 in Utah; Section 4). A science team composed of experts in planetary spectroscopy and geology was tasked with developing a set of hypotheses regarding the geologic origin of each field site using remote-sensing images and hyperspectral data (Section 3.5) and encoding these into a hypothesis map (Section 3.1). The hypothesis map was then uploaded to the rover, which then used it to explore each field site. Three different exploration scenarios were explored and compared (Section 3.6) using exploration metrics defined in Section 3.7.

## 3. Exploration Architecture

### 3.1. Rover Science Autonomy Tools

Rover science autonomy uses onboard machine learning, decision-making, and data analysis tools to apply a set of driving hypotheses that enable a rover to examine a field site autonomously. Under this paradigm, the rover plans traverses, acquires measurements, performs data analysis, and uses the knowledge acquired from the results to plan further activities. Because it is not limited by data transmission rates and data volumes, a rover capable of science autonomy can acquire and analyze significantly more data than it can transmit back to Earth. The rover therefore contacts the operator only periodically to offer updates, to request new directions, or when the robotic explorer encounters circumstances that fall outside the realm of expected observables. The data transmitted by the rover can be a subset of the total data volume collected, where data critical to the interpretation of information are transmitted as a whole, and superfluous information is either compressed using more volume-efficient formats or simply summarized.

Central to the rover's decision-making and data analysis capabilities are (1) the hypothesis map, (2) the Tetracorder expert system, and (3) the science interpretation algorithm.

#### 3.1.1. The Hypothesis Map

The hypothesis map is the basis for decision-making and reporting undertaken by the rover. It is a probabilistic spatial model on the rover's computer that encodes a set of hypotheses to be explored and is updated as new information becomes available. To this end, the hypothesis map relies on Bayesian inference and information theory principles. In the hypothesis map, the set of hypotheses are all the possible classifications of individual locations; for example, the possible geologic origins of a site, where discrete conditional probabilities of each geologic origin are contained in the model. Crucially, the hypothesis map also represents the evolving likelihood of the classification for each spatial unit. As the rover explores a field site, it performs measurements, which it interprets in the context of the available hypotheses. These interpreted observations impact the likelihood of each hypothesis. The rover uses this updated hypothesis map to select the next destination for analysis (henceforth "science stops") and plan its traverse. The hypothesis map also allows the system to react to unanticipated events that occur while the robot is out of contact (D. R. Thompson et al. 2011). Communication with the remote science team can occur at any point in the process, whether periodically or at points where the rover has (a) a summary of observations of the mapping area, (b) identified sample collection sites, or (c) performed an observation that cannot be fit into the hypothesis map. If (c) occurs, the hypothesis map needs to be reformulated by the science team, leading to an iterative process between hypothesis formulation and field exploration.

The formulation of the hypothesis map is dependent on the nature of the investigation. In this application, the rover's task was to constrain the geologic origins of different photogeologic units at a field site. The hypothesis map was encoded as a data cube consisting of stacked maps of the field site, with each layer corresponding to a possible geologic origin, and the value of each pixel quantifying the relative probability of the geologic origin at the pixel location. The likelihood of a possible geologic origin was estimated from the number of diagnostic minerals relevant to a particular formation origin identified within the geologic unit; the higher the nonzero number, the greater the likelihood (Figure 1). As the rover observed the terrain using its instrument suite and analyzed the data, the interpretation of measurements increased the likelihood of some geologic origins in a local area while decreasing

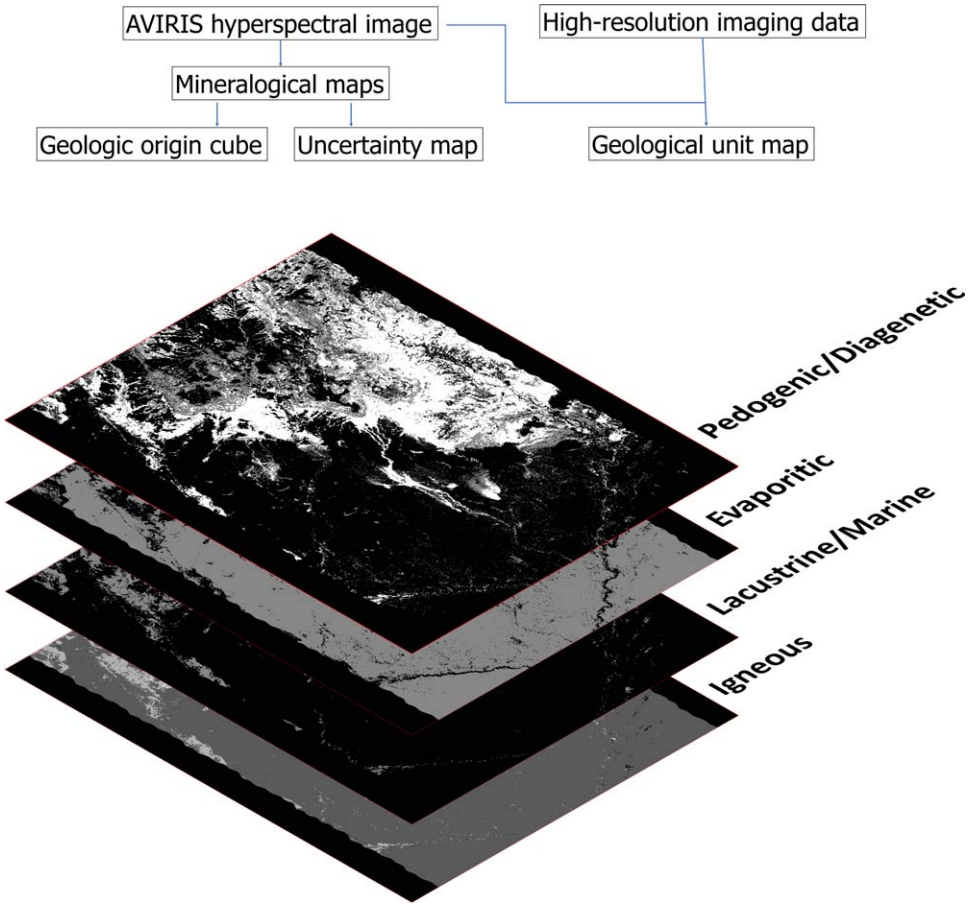


**Figure 1.** Generation of the initial hypothesis map. Top: flowchart summarizing the data and data products used to produce the geologic origin cube, uncertainty map, and photogeologic map. Bottom: conceptual image of the geologic origin cube. The *x*- and *y*-axes correspond to spatial dimensions on the map, and each plane represents a different geologic origin. The likelihood of a geologic origin for a location increases with pixel value. Conversely, uncertainty increases with the number of layers having a value greater than 0 at a location. For any particular pixel, the more layers having a value. The rover disambiguates the geologic origin for each terrain by visiting regions of high uncertainty. Six different geologic origins were considered (four are shown for illustrative purposes). As the rover queries the terrain, it updates the hypothesis map and then uses the updated map to plan the next leg of the traverse.

others. The initial probabilistic cube encoded onto the rover for our terrestrial field work was generated from mineralogical maps derived using Tetracorder (see below) from hyperspectral images obtained with the NASA Airborne Visible/Infrared Imaging Spectrometer (AVIRIS; R. O. Green et al. 1998).

In addition to the geologic origins cube, an uncertainty map was generated that spatially encoded the number of nonzero potential geologic origins (e.g., an *x*, *y* pixel location with value greater than zero in two or more planes of the geologic origin map). The rover's job was to plan a traverse that visited the areas of greater uncertainty to obtain more data, which would thus reduce the uncertainty in the area and other areas within the same photogeologic unit.

The track the rover subtends in the map is narrow and very localized, so while the rover can do a good job at disambiguation at the locations where it performs measurements, projecting the results onto the rest of the map requires that terrains are classified into groups so that the results at a specific location can be extrapolated to other locations on the map. Methods that were considered to classify and group terrains included spectral classification maps derived from the AVIRIS data (e.g., principal components, spectral angle mapping, band-depth mapping) and photogeologic mapping. In the end, a photogeologic map was prepared using a combination of high-resolution imagery from Google Earth and parameterized data derived from the hyperspectral images (Figure 2).

### *3.1.2. Tetracorder*

Tetracorder (R. N. Clark et al. 2003, 2024; R. N. Clark 2024) is a framework for applying algorithms commanded by an expert system that determines the best answers in data groups covering different conditions. When applied to spectra, Tetracorder analyzes multiple spectral regions independently, identifying the compositions expressed in each spectral region, called a group. Each analysis can invoke additional analyses to test for special cases and further analyze a specific condition in more detail. For a single spectrum, the analysis takes a fraction of a second. Tetracorder also analyzes imaging spectrometer data, and unlike other algorithms, compute time increases linearly with added compounds, enabling thousands of materials to be searched for with current computer technology.

With over 100 person-years of development by scientists at the United States Geological Survey, the Planetary Science Institute, and elsewhere, Tetracorder has a demonstrated track record, being used throughout the solar system and in terrestrial studies, including rapid response during disasters (R. N. Clark et al. 2001, 2003, 2015, 2016). Tetracorder is open source (https://github.com/PSI-edu/spectroscopy-Tetracorder). During the TREX field campaign, the Tetracorder expert system


**Figure 2.** Photogeological map of site 3, Yellow Cat Flat. Each unit is numbered and depicted in a different color.

employed over 30,000 lines of instructions to analyze visible–near-infrared (VNIR) to shortwave infrared (SWIR) spectra (0.35–5 $\mu$m) for pure minerals, intimate and areal mineral mixtures, coatings, and molecular mixtures for hundreds of minerals and other compounds using 28 spectral groups.

An identification example of an AVIRIS spectrum is shown in Figure 3. Several absorption bands are tested (after continuum removal; Figure 3(a)) and fitted to the observed reference spectra using a modified least-squares procedure (Figure 3(b)). Clearly the best fit is kaolinite KGa-2 in this example, and Tetracorder would identify the presence of kaolinite for this spectrum. If there were other components contributing to the 2.2 $\mu$m absorption feature, the fit would not be as good, which would trigger Tetracorder to also test intimate and areal mixtures to find the best mixture solution. Other spectral regions would also be analyzed for additional compounds. While the concepts in Tetracorder are mature and proven, spectroscopic interpretations are still limited by available laboratory spectral libraries. For this work, Tetracorder used USGS spectral library splib06 (R. N. Clark et al. 2007) with supplements.

#### 3.1.3. Science Interpretation Algorithm

The science interpretation algorithm provides the autonomous science rover with the ability to interpret the available data in the context of the hypothesis map. In our study, the algorithm used a set of nested lookup tables relating mineralogy to potential geologic origin(s) (Figure 4). This table allowed the rover to compute likelihoods of geologic origins given minerals (that are found in the scene) and to update the hypothesis map accordingly using Bayesian inference.

Often the relationship between individual mineralogy and geologic origin is not unique, as multiple geologic origins can result in the formation of the same mineral; however, the detection of multiple minerals (or a mineralogical assemblage) pointing to the same origin improves constraints. The ability of Tetracorder to query multiple wavelength regions enabled the identification of multiple minerals from a single spectrum and hence improved confidence in the geologic interpretation.

Geological origins were grouped into six classifications based on similarity geological processes (Table 1). We chose to separate low-grade metamorphic processes from higher-temperature hydrothermal processes because the implications of these two different processes are significant from a geological standpoint.

The geologic origin tables used in this work are given in Appendix A (year 1) and Appendix B (year 2). Whereas these two tables are superficially similar, the results from the first field expedition informed the production of the table for the second field expedition. One major issue that was encountered in year 1 was that, due to the fact that computing time increased quadratically with number of mineral entries, only a subsample of minerals were selected for the table in year 1. This subset proved to be insufficient. As a consequence, it was decided to include a significantly larger number of minerals. In order to get around the issues with computing time, minerals were classified using a set of nested lookup tables. The first table (Appendix B.1) associated the mineral spectrum with a class defined on the basis of similarity of formation (e.g., the multiple alunite entries correspond to the hydrothermal_pedogenic_alunite class) in the second table (Appendix B.2), which associated the classes with one or more specific origins.

### 3.2. Rover

In this work we used the exploration robot Zoë (Figure 5) developed at Carnegie Mellon University (D. S. Wettergreen et al. 2005; N. A. Cabrol et al. 2007). Zoë is 2 m long and can move up to 1 m $s^{-1}$ under solar power. Zoë's front and rear axles pivot freely and are steered by the differential velocity of the four wheels (M. Wagner et al. 2005). It drives variable-radius arcs and reliably surmounts obstacles of up to 25 centimeters in height.

Zoë carries a computer with an Intel i7 processor with a base frequency of 2.8 GHz and four cores, as well as 4 GB of DDR4 memory, running Ubuntu Linux. In general, computation time was not a limiting factor for the rover's field analyses.

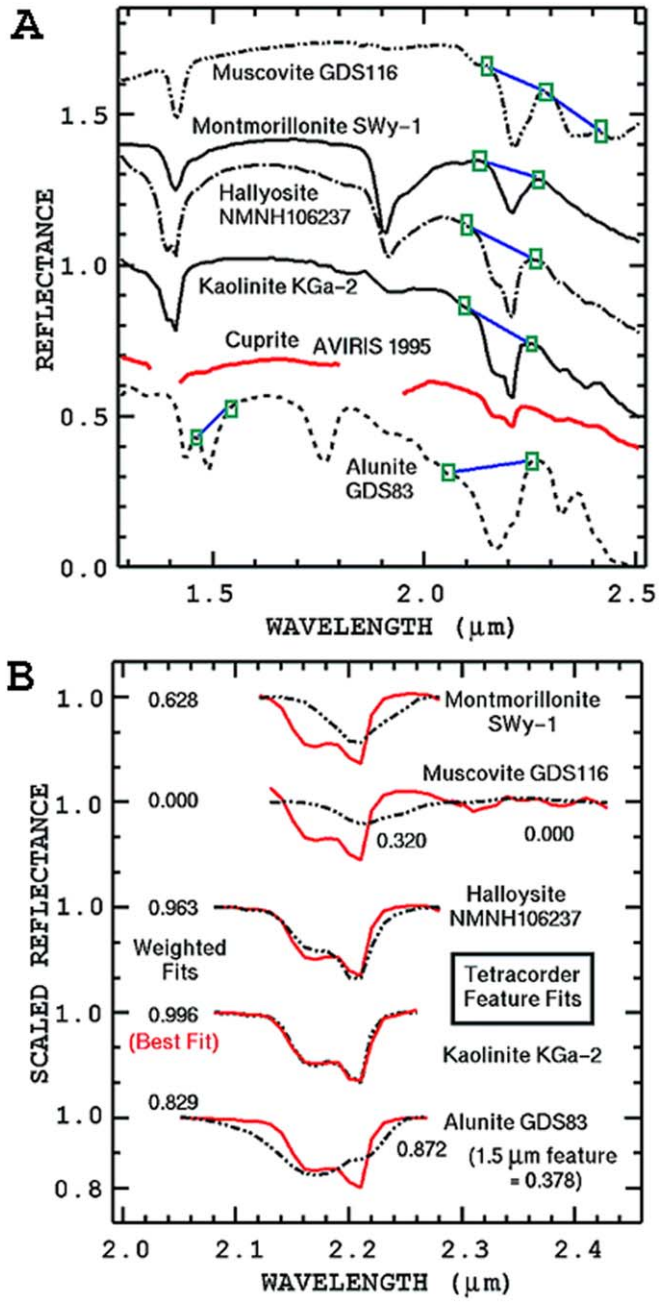


**Figure 3.** Tetracorder fitting procedure. (a) A few examples are shown out of hundreds of compounds and mixtures that are continuum removed and fitted (b) to the unknown spectrum (red) using a modified least-squares procedure. Green boxes are the continuum wavelengths for the specific 2.2 $\mu$m feature in each library spectrum. Blue lines represent the continuum used for continuum removal. In this example, this spectral region only shows absorption due to kaolinite, but other regions may show absorptions due to other compounds, enabling many compounds to be found in a spectrum. From R. N. Clark et al. (2003), public domain images.

Depending on the complexity of each path planner, the planning process for each waypoint required less than a minute to execute.

Zoë employs an onboard navigation system that incorporates GPS and a compass with an inertial measurement unit and wheel odometry to estimate position and orientation. This localization was used to determine geographic coordinates whenever it collected a VNIR spectrum. Zoë uses planar homography to convert from geographic coordinates (latitude and longitude) to map pixel coordinates (row and column), enabling the spatial registration of in situ spectra with the hypothesis map.

### 3.3. Instruments

A suite of instruments that included remote-sensing, contact, and sample analysis instruments (Table 2) was used during these investigations. These instruments included a visible stereo imager, a VNIR (0.3–2.5 $\mu$m) point spectrometer with mast-mounted foreoptics, a gamma-ray spectrometer (GRS) covering 300 keV–4 MeV (T. H. Prettyman et al. 2023), a set of handheld contact-probe spectrometers with a combined spectral range of 0.178–15.4 $\mu$m, a high-resolution handheld camera for sample imaging, and a portable X-ray diffractometer.

The mast-mounted stereo camera pair (analogous to the science PanCams on the Mars Exploration Rovers; J. F. Bell et al. 2003; S. W. Squyres et al. 2003) and spectrometer foreoptics were mounted at 2 m height on an actuated pan-tilt base with full 360° rotation. The VNIR spectrometer, an Analytical Spectral Devices (ASD) Fieldspec 3, sampled at 1.4 nm intervals in the 350–1050 nm range and 2 nm intervals in the 1000–2500 nm range. Its foreoptic lens was fixed to the pan-tilt servo unit on the rover mast and had a 1° field of view (FOV). The rover periodically aimed the spectrometer foreoptics at a Spectralon white reference target fixed to the rover deck to compensate for changes in ambient illumination by renormalizing the spectra to the white reference.

Handheld point spectrometers included an Agilent 4300 Handheld Fourier transform infrared (FTIR) spectrometer (C. Hutengs et al. 2018), a second ASD Fieldspec 3, and a UV point spectrometer (178–963 nm at 0.76 nm spectral sampling). The Agilent FTIR interrogated the SWIR to mid-infrared (MIR) spectral region (2.5–15.4 $\mu$m) at a spectral sampling interval of $\sim$3.7 cm$^{-1}$ and a resolution of $\sim$8 cm$^{-1}$.

A commercial off-the-shelf (COTS) Canon 80D digital single-lens reflex (DSLR), equipped with a cropped red-green-blue (RGB) complementary metal-oxide-semiconductor (CMOS) sensor and a 180 mm macrophotography lens, was used to acquire high-resolution images of the targets measured by the point spectrometers. Images were acquired at a spatial resolution of approximately 4 $\mu$m pixel$^{-1}$ and an FOV of 1.7 cm $\times$ 2.5 cm.

A portable X-ray diffraction (XRD) Olympus Terra, a commercial analog of the ChemMin instrument aboard the Mars Science Laboratory, was also used in the field to acquire XRD patterns of selected targets at science stops.

The mast-mounted imagers and VNIR spectrometer acquired data in prescribed sequences (the spectrometer acquired data during traverses and at science stops), whereas the GRS was in continuous-acquisition mode. The contact-probe spectrometers, handheld camera, and XRD measured specific sample targets at science stops. Spectral data from the FTIR and the two VNIR spectrometers were uploaded to the rover for Tetracorder analysis and hypothesis map testing at these stops. Data from the VNIR spectrometers and the SWIR region (2.5–4.3 $\mu$m) of the FTIR were used by the rover for hypothesis testing. Data from the other instruments were provided to the science team for additional analysis.

### 3.4. Rover Commander

Definition of science stops, traverses, and observation sequences to be executed by the rover was performed by the

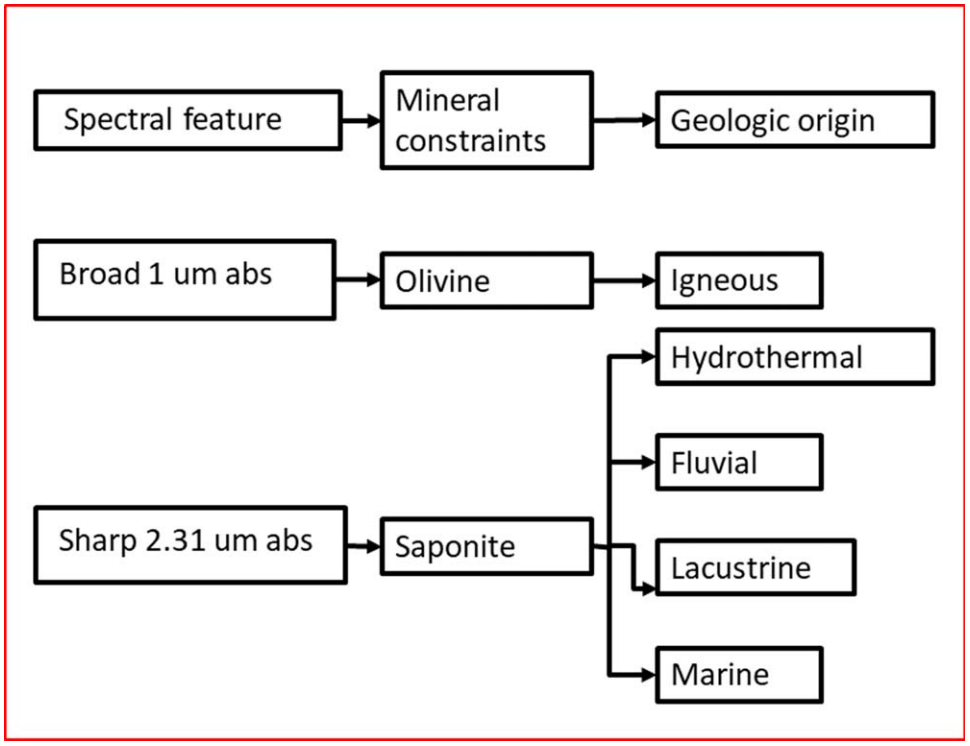


**Figure 4.** Science interpretation algorithm to constrain geologic origin. Detection of minerals (where abs = absorption) with few possible origins or multiple minerals with similar origins increases the confidence in geologic origin, whereas detection of single minerals with multiple possible origins increases the uncertainty.

**Table 1**
Classification of Geologic Origins

| Geological Origin | Description |
|---|---|
| Fluvio-lacustrine/marine | Minerals deposited in fluvio-lacustrine and marine settings. |
| Evaporitic/playa deposits | Minerals deposited in evaporitic and playa-like environments, including salts. |
| Metamorphic | Minerals produced in metamorphic or low-temperature hydrothermal environments (e.g., greenschist facies). |
| Hydrothermal | Mineral assemblages produced in hydrothermal environments. |
| Pedogenic/diagenic/weathering | Minerals produced in post-depositional near-surface environments or as weathering rinds. |
| Igneous | Minerals produced as a result of intrusive or extrusive igneous processes. |

science team using the Rover Commander tool. Rover Commander is a home-grown browser-based tool that enables scientists to generate plans and define measurement sequences for rover operations in the field. For easy implementation and maintenance, Rover Commander was developed using off-the-shelf components and frameworks like Google Maps API.

A primary objective of Rover Commander was to establish a flexible online environment where scientists could graphically devise new workflows for the rover's field tasks. To achieve this capability, we distilled a comprehensive list of fundamental operations that the rover could execute and made them accessible through the Rover Commander interface. Using these operations as building blocks, scientists could define various reusable workflows and operation sequences (e.g., measurement sequences). For instance, when exploring the Yellow Cat site, the science team devised a specific command sequence called CliffView to collect spectral and imaging data along a vertical transect of a nearby escarpment, using angular increments defined by the science team.

Another crucial aim of Rover Commander was to facilitate collaborative brainstorming and deliberation among scientists regarding potential locations for rover field experiments. Recognizing that scientists could be geographically dispersed during the planning process, we developed the LiveMarker feature. This functionality enabled scientists to place markers at proposed science stops and instantly displayed them on the screens of other scientists logged into the Rover Commander interface.

The versatility of Rover Commander allowed it to be implemented flexibly in response to the requirements of each scenario. In the human-directed scenarios (1 and 3), Rover Commander was used to identify science stops, establish traverse paths, and define observation sequences. During the rover-directed exploration, the science team used Rover Commander to suggest desired waypoints and defined observation sequences.

### *3.5. Science Team*

The science team consisted of a group of five experts in the fields of planetary spectroscopy and geology. The overall goal of the science team was to work with the rover to interpret the geology of the field sites. The specifics of the science team's role varied with mission scenario (Section 3.6), but in general the science team fulfilled roles in hypothesis development, operational planning, and data analysis.

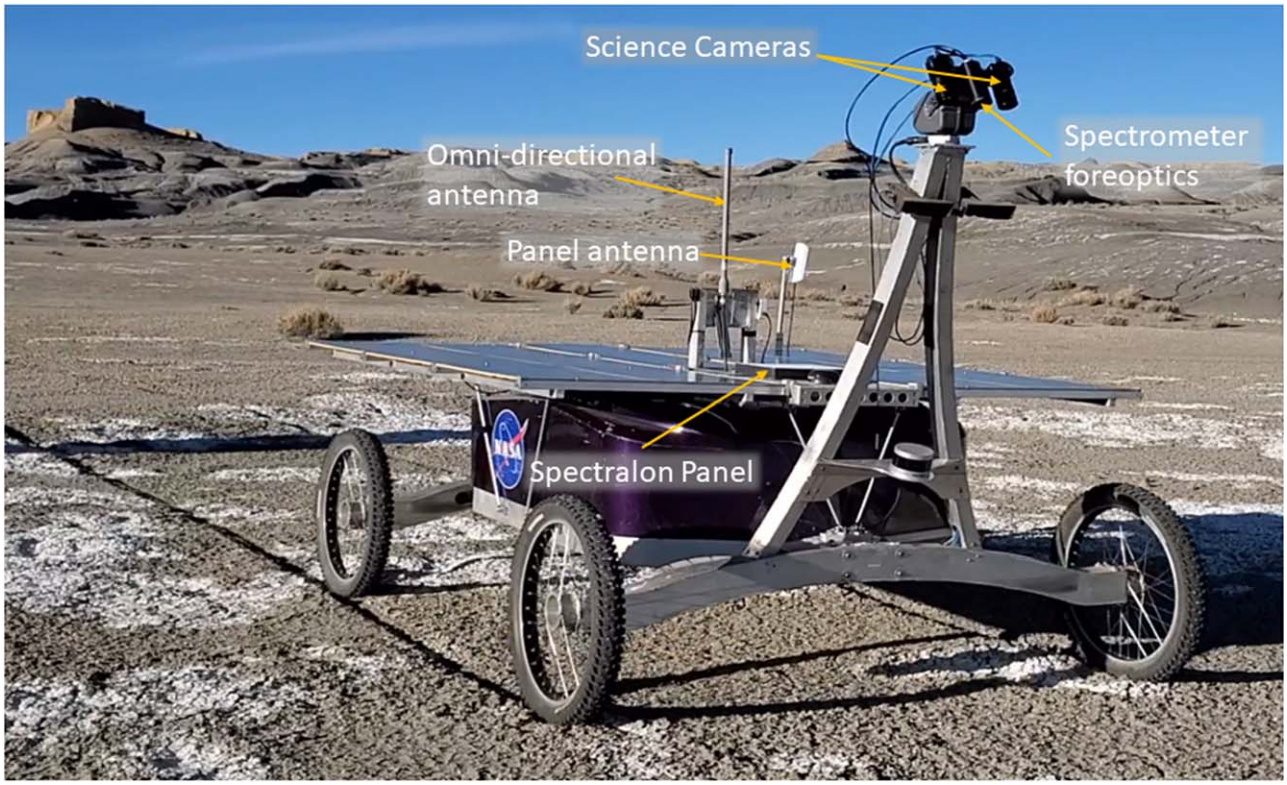


**Figure 5.** Zoë traversing efflorescent salt patches on clay-bearing deposits of the Blue Canyon, AZ—2021 October. The science cameras and spectrometer foreoptics are shown on the mast. A panel antenna allowed communication with a ground station at distances of up to 2 km.

**Table 2**
Instruments

| Data Set | Pixel Scale or FOV/IFOV | Spectral Range (Bands) | Spectral Sampling/Resolution |
|---|---|---|---|
| | Rover Mounted | | |
| NavCams | … | RGB (450, 550, 620 nm) | N/A |
| Science Cams. | $14.^{\circ}3 \times 10.^{\circ}5$ (1024 × 1024 pixel) 90 $\mu$rad pixel$^{-1}$[a] | RGB (450, 550, 620 nm) | N/A |
| ASD Fieldspec 3 | 1° | 0.35–2.5 $\mu$m (2151 bands) | 1.4–2 nm/10 nm |
| GRS | 1–2 m | 300 keV–4 MeV | 4 keV ch$^{-1}$/<60 keV |
| | Contact | | |
| Micro-Imager[a] | 20 $\mu$m pixel$^{-1}$ | RGB (450, 550, 620 nm) | N/A |
| UVS | 5–10 mm | 0.178–0.963 $\mu$m (1036 bands) | 0.76 nm/1.6 nm |
| FTIR | 5 mm | 2.5–15.4 $\mu$m (900 bands) | 8 cm$^{-1}$/8 cm$^{-1}$ |
| ASD Fieldspec 3 | 5 mm | 0.35–2.5 $\mu$m (2151 bands) | 1.2 nm/10 nm |
| | Sample Analysis | | |
| Olympus Terra XRD | … | $2\theta = 5°$–$55°$ | $2\theta = 0.^{\circ}05$ |

**Note.**
[a] Added to the instrument suite in the second season to acquire images of the contact-probe targets for analysis by the science team.

(1) *Hypothesis development*: the team formulated geological hypotheses about a field site based on remote-sensing and hyperspectral data.
(2) *Operational planning*: the science team identified key science stops, defined observation sequences, and established traverse paths.
(3) *Data analysis*: during rover deployment, the team interpreted data transmitted by the rover, updated hypothesis maps, and refined exploration goals.

The science team worked remotely from a mission science center and did not visit the field site before or during field activities. Transmission of data from the rover to the science center and all communications with the field team were performed via satellite. Once field activities had concluded and the science team had finalized their interpretations and report, they visited the site for edification purposes and to gain a firsthand understanding of the limitations of the exploration strategies they had employed.

Science team members were selected on the basis of expertize in the function and data analysis of at least one of the instruments and a solid background in geology. One scientist was assigned as a lead for each instrument on the rover, and an additional science team member fulfilled the role of documentarian. The role of the instrument leads was to verify the integrity of the downlinked data and to perform the analysis of the data. A team lead coordinated analysis and discussions within the team and served as the point of contact between the science team and the field team.

**Table 3**
Scenario Comparison Summary

| Scenario 1: Human-directed Exploration | Scenario 2: Rover-directed Exploration | Scenario 3: Astronaut/Rover Collaborative Exploration |
|---|---|---|
| 1. Science stops and traverses identified by science team | 1. Rover is provided with priori hypothesis and uncertainty maps developed by science team before field expedition. | 1. Science team selects science stops for astronaut and rendezvous stops. |
| 2. Preestablished measurement sequences | 2. Preestablished start and end locations. | 2. Rover drives directly to each stop and waits for astronaut to arrive (year 1) or drives to rendezvous point via a rover-defined traverse that includes rover-selected science stops (year 2). |
| 3. One set of preestablished contact measurements performed (FTIR, UVS, XRD). | 3. Science stops and traverse determined by rover. | 3. Astronaut traverses to stops but has the option of diverting from nominal route to perform observations. Year 1: astronaut can change location of science stop and command rover to meet at new stop or to perform new activities in real time. Year 2: astronauts and rover proceed via two separate contemporaneous EVAs. |
| 4. Science team analyzes the data and requests additional contact and sampling measurements at that science stop. | 4. Preestablished measurement sequences | 4. Astronaut performs tasks that cannot be accomplished by the rover. |
| 5. Once done, rover is commanded on to the next science stop. | 5. One set of preestablished contact measurements performed (FTIR, UVS, XRD). | 5. Astronaut uses rover at rendezvous spots to perform measurements and analysis of astronaut-collected samples. |
| | 6. Rover analyzes data acquired during traverse and at arrival to science stop. | |
| | 7. Rover updates hypothesis and uncertainty maps, identifies next science stop, and recalculates traverse. | |
| | 8. At end of day, rover transmits results and updated hypothesis map to science team, which assesses information and can update the hypothesis map before the next day. | |

### *3.6. Mission Scenarios*

We explored three different operational mission scenarios: (1) human-directed rover exploration, (2) rover-directed exploration, and (3) astronaut/rover collaborative exploration. The purpose of this study was to compare the operational efficiency and science yield of these scenarios. A science team was tasked in each scenario to assess the geologic history of the site using the tools available to them. Table 3 summarizes and compares all three scenarios, while Tables 4–6 delineate each scenario at higher granularity.

#### *3.6.1. Scenario 1—"Human-directed Exploration"*

This scenario sought to emulate the paradigm of directed rover exploration typically used currently in planetary exploration (i.e., Mars Exploration Rovers, Mars 2020, Mars Science Laboratory). In this paradigm, a team of remote scientists and operators commanded the rover on a step-by-step basis. The rover executed each command and returned data to the science team, which analyzed the data and decided on the next command to be sent to the rover.

In preparation for this scenario, the science team produced photogeologic and mineralogical maps using remote-sensing data consisting of high-resolution imagery in Google Earth and AVIRIS hyperspectral imaging data of the site. The photogeologic units were defined on the basis of geomorphic and mineralogical associations. All pixels within a unit were assumed to share the same set of geologic origin probabilities, and all measurements performed by the rover within a unit contributed to the geologic interpretation of that unit (Figure 1).

The science team then established a set of working hypotheses about the geologic origin of the photogeologic units and developed a plan for exploration of the site. The plan included the identification of desired science stops (target destinations where the rover performed measurements using its instrument suite), traverses between these stops, and measurement sequences to be performed at the science stops and during traverses.

The stops were selected to sample as many of the different photogeologic (from visible imaging) and mineralogic (from imaging spectroscopy) units identified by the team as possible. At each of these stops, the rover performed a series of prescribed measurements using a mast-mounted VNIR (0.35–2.5 $\mu$m) spectrometer and a visible color imaging camera and then transmitted the data back to the science team (prescribed spectral measurements were also collected during traverses between stops and transmitted along with the measurements performed at the stop). The science team then had the option to request additional measurements using the contact-probe spectrometers and the XRD instrument. Close-up images were acquired at each of the contact-probe targets. Once these measurements were performed, the rover traversed on to

**Table 4**
Scenario 2: Rover-directed Exploration Command Cycle

| |
|---|
| 1. Science Team |
| • Generates geological origin cube, uncertainty map, and photogeologic map using aerial images and AVIRIS hyperspectral data. |
| • Provides geologic origin lookup table. |
| • Provides observation sequences to execute during traverse and at science stops. |
| • Provides initial desired science sites, specified to ±5 m, with minimum spacing of 50 m between science stops (site 3 only). |
| 2. Rover |
| • Identifies science stops and plans out traverses on the basis of uncertainty map, terrain, and resource consumption. |
| • Traverses to science stop while executing measurement sequences defined by the science team. |
| • Performs Tetracorder analysis using data acquired with ASD and shortwave portion of FTIR. |
| • Uses geological origin lookup table to associate mineralogy with geologic origin and modify the likelihood of that origin for the geologic unit. |
| 3. Science Team |
| • Analyzes data returned by the rover. |
| • Analyzes spectra of measurements containing new minerals as identified by rover, reexamines hyperspectral cube pixels updated in the mineralogical origin map to assess rover's interpretation, and updates geological map based on results. |
| • Sends updated geologic origin map to rover, as well as new science stops to visit (if any). |
| Scenario 1. Human-directed Exploration Command Cycle |
| 1. Science team: |
| • Defines science stops and observation sequences for rover to execute during directed traverse and at science sites. |
| 2. Rover: |
| • Traverses to science stop and performs prescribed measurements. |
| • Transmits raw data and analyses back to science team. |
| 3. Science team: |
| • Analyzes data returned by rover, decides on next set of rover activities and observations at each science stop. |
| • Requests additional measurements to be performed at science stops with contact-probe instruments. |
| 4. Rover: |
| • Acquires additional measurements with contact probes. |
| • Transmits data back to science team and begins traverse to next science stop. |

the next science stop. Analysis of the returned science data by the science team took on the order of hours to complete. We budgeted 3 days for scenario 1 at each of the three field sites. The command cycle for scenario 1 is delineated in Table 4.

#### *3.6.2. Scenario 2—"Rover-directed Exploration"*

This scenario sought to test our rover-directed exploration paradigm and compare it with the exploration paradigm of scenario 1. In preparation for this scenario, the science team generated a hypothesis map (geologic origin cube and uncertainty map derived from 0.38–2.5 $\mu$m imaging spectroscopy data at approximately 18 m pixel$^{-1}$; see Section 3.1) that served as a prior geologic origin distribution that would be updated with rover-collected data. This map and the photogeologic map prepared prior to scenario 1 were provided to the rover. During each traverse, the rover collected data and updated its hypothesis map based on the minerals that were found and the likelihood that they correspond to different geologic origins. At each science stop, the rover computed the most recent uncertainty map using the hypothesis map to select the next science stops and plan a traverse to it. The rover

**Table 5**
Scenario 1: Human-directed Exploration Command Cycle

| |
|---|
| 1. Science team: |
| • Defines science stops and observation sequences for rover to execute during directed traverse and at science sites. |
| 2. Rover: |
| • Traverses to science stop and performs prescribed measurements. |
| • Transmits raw data and analyses back to science team. |
| 3. Science team: |
| • Analyzes data returned by rover, decides on next set of rover activities and observations at each science stop. |
| • Requests additional measurements to be performed at science stops with contact-probe instruments. |
| 4. Rover: |
| • Acquires additional measurements with contact probes. |
| • Transmits data back to science team and begins traverse to next science stop. |

selected science stops by identifying the location of greatest uncertainty within a 50 m radius from the current stop (we also performed tests using a radius of 100 m for comparison purposes). During the second season, we also enabled the science team to suggest science stops before the start of the scenario. These stops could be similar to those selected for scenario 1. If the rover found itself within 50 m of the suggested science stop, it prioritized visiting this stop.

During the traverse to and at each of the science stops, the rover performed a series of prescribed measurements using the mast-mounted VNIR spectrometer and imager. Additionally, contact-probe spectrometers were used to perform measurements at science stops. To avoid any human-induced prejudice, the contact-probe target position at science stops was prescribed by a focus point 20 cm directly in front of the center of the rover's front side. After measurements were performed at each science stop, the rover used its onboard data analysis suite to analyze the spectra from the mast-mounted and contact VNIR spectrometers and from the short-wavelength end (2.5–5 $\mu$m) of the FTIR spectrometer to determine mineralogy, assign potential geologic origins associated with the minerals in each spectrum, and update the hypothesis and uncertainty maps.

During the first field season, the data were immediately transmitted to the science team for analysis. The science team then had the option of requesting contact-probe spectra of additional targets at the science stop. The total number of allowable contact-probe targets was limited to the cumulative total of probe targets measured during scenario 1. This allowed the science team to perform their own analysis in parallel to the rover. The science team did not look at the updated hypothesis map at each science stop, however. This strategy was not repeated in the second field season because the cadence at which the rover communicated with the science team hindered the progress of the rover and did not allow for a complete test of the rover science autonomy. In the second field season, we instead opted to have the rover transmit at the end of the day all of the data accumulated from multiple science stops along with the updated hypothesis map. The science team was then tasked to look at the updated hypothesis map and verify it against the data that were acquired. The science team then had the option of updating the hypothesis map as well and of sending it back to the rover to use on the next day's command cycle.

To allow for some degree of comparison with scenario 1 while attempting to control the number of free parameters, the

**Table 6**
Scenario 3: Astronaut/Rover Collaborative Exploration Cycle

| Year 1 | Year 2 |
|---|---|
| 1. Science Team | |
| • Defines rendezvous/science stops for rover and astronaut. | • Defines science stops for the astronauts and rendezvous stops for rover and astronaut to meet. |
| • Provides observation sequences and activities to execute during traverse and at science sites. | • Provides geologic origin lookup table for rover. |
| | • Provides observation sequences and activities to execute during traverse and at rendezvous stops. |
| 2. Rover | |
| • Rover operated in a way more directly comparable to our human-directed exploration: | • Rover operated in a way more directly comparable to our rover-directed exploration: |
| • Traverses directly to science-team-selected science stops. | • Selects science stops to investigate between rendezvous stops and plans out traverses based on uncertainty map, terrain, and resource consumption. |
| • GRS data acquired continuously along traverse; other instruments acquired data at science stops as directed by the science team and astronaut. | • Performs Tetracorder analysis using data acquired with ASD and shortwave portion of FTIR. |
| • Transmits raw data back to science team. | • Uses geological origin lookup table to associate mineralogy with geologic origin and modify the likelihood of that origin for the geologic unit. |
| • Rover instruments and in situ science analysis capabilities used for measurements of astronaut-collected samples with real-time results communicated to the astronaut. | • GRS data acquired continuously along traverse; mast-mounted ASD data and other instrument data collected during traverses and at science stops as defined by science team. Instrument acquired data collected at rendezvous stops as directed by the science team and astronauts. |
| | • Transmits raw data back to science team. |
| | • Rover instruments and in situ science analysis capabilities used for measurements of astronaut-collected samples with real-time results communicated to the science team. |
| 3. Astronaut | |
| • Has flexibility to adjust traverse path in real time to thoroughly explore the local geology. | |
| • Performs tasks that cannot be accomplished by the rover (e.g., accessing rough terrain, digging trenches, and collecting samples). | |
| • Uses rover's instrument suite to perform measurements and analysis of samples collected along traverse at rendezvous spots. | |
| One astronaut working collaboratively with the rover throughout the EVA. | Two astronauts working together separately from the rover along the traverse but collaboratively at rendezvous stops. |
| • Traverses to science/rendezvous stop but has the option of diverting from rover route in real time to perform observations and/or collect samples that may address science questions | • Proceeds on a traverse separate from the rover to science-team-selected EVA science stops conducting tasks coordinated with the science team. |
| • Can change location of science stops and command rover divert from its path to new locations. | • Cannot redirect the rover to new locations or complete new collaborative tasks with rover in real time. |
| 4. Science Team | |
| • Analyzes data returned by the rover and astronaut(s); makes real-time assessment of new or unexpected information and decides if actionable within the EVA time frame. | • Analyzes spectra of measurements containing new minerals as identified by rover, reexamines hyperspectral cube pixels updated in the mineralogical origin map to assess rover's interpretation, and updates geological map based on results. |
| • Requests additional rover and astronaut collaborative measurements and activities at science stops and/or on astronaut traverse. | • Sends updated geologic origin map to rover. |
| | • Requests additional observations/activities along astronaut traverse as needed. |

following parameters were constrained to be the same as those performed during scenario 1:

1. start and end locations for the traverse;
2. total number of science stops along each traverse;
3. total number of measurements acquired with the contact-probe spectrometers; and
4. prescribed measurement sequences executed with the remote-sensing instruments at each science stop. This last requirement was relaxed in the second field season.

The command cycle for scenario 2 is delineated in Table 5. For the first two sites (Black Point Lava Flow and Blue Canyon), both of which were explored during the first field season, only one command cycle was performed during the scenario 2 (rover-directed) exploration, and the science team had an opportunity to review the findings from the rover's data at the end of scenario 2 before writing their report. For the Yellow Cat Flat site, which was explored in the second field season, an additional command cycle was performed, with the science team reviewing the rover's updated hypothesis map and the collected data before issuing a new hypothesis map and a new set of desired science stops back to the rover.

#### *3.6.3. Scenario 3—"Astronaut/Rover Collaborative Exploration"*

This scenario sought to design, implement, and test different methods of collaborative exploration between astronauts and a rover capable of science autonomy. They were members of the science team and performed the same roles as the other members of the science team during scenarios 1 and 2. The astronauts selected for this scenario were planetary scientists

**Table 7**
Exploration Metrics

| Parameter | Metric |
|---|---|
| Operational efficiency | Number of science stops visited |
| | Distance traveled or time required to visit a number of sites |
| Science yield | Rate of data acquisition |
| Added value of astronaut/rover collaboration | Improvement in data acquisition rate |
| | Improvement in geological interpretation of visited sites |
| | Number of additional science stops visited |
| | Additional data collected by the astronaut(s) (samples, imaging at vantage points inaccessible to rover, etc.) |

with expertize on geology, who have been working on preparation and planning for Artemis. For field sites 1 (Black Point Lava Flow) and 2 (Blue Canyon), the rover was commanded to drive to science-team-selected science stops, where it would wait to be joined by a deployed astronaut. The rover did not use a hypothesis map and drove directly to science-team-selected science stops. The astronaut independently traversed to the same science stops along a route of their determination, responding to their observations of the local geology and adjusting their exact path as necessary in real time to investigate science questions, collect samples, and complete activities coordinated with the science team (M. Banks et al. 2024, in preparation). Astronaut activities focused on tasks that could not be completed by the rover but were needed to fill gaps in the scientific understanding of the geology. The rover and astronaut rendezvoused at each science stop to complete collaborative observations and tasks before proceeding to the next. Additionally, the astronaut could choose to alter science stop locations in real time during their traverse and direct the rover to divert from its path to these locations for science activities. The approach for the first two sites (Black Point Lava Flow and Blue Canyon; year 1) was more directly comparable to our "human-directed exploration" (scenario 1) with the addition of one astronaut (M. Banks et al. 2024, in preparation).

For field site 3 (Yellow Cat Flat), visited in our second field season, we changed our approach to leverage the rover's autonomous capabilities to enhance overall science return and maximize extravehicular activity (EVA) efficiency. This approach had the benefit of being more directly comparable to the "rover-directed exploration" (scenario 2) with the addition of a team of two astronauts. At Yellow Cat Flat, the rover functioned essentially as it did in scenario 2 ("rover-directed exploration") and used the hypothesis map to define its own traverse and science stops with a prescribed start and end point and the maximum total distance budget it could drive for the overall EVA. The science team selected several locations to serve as "rendezvous stops" (approximately two to three stops per EVA). The rover was directed to wait at these rendezvous stops for the astronauts so it could acquire in situ measurements of the astronaut-collected samples and transmit the data to the science team for analysis in real time during the EVA (M. Banks et al. 2024, in preparation). This approach provided a trade-off in which the astronauts and science team no longer had the ability to redirect the rover to new locations or complete some collaborative tasks in real time during the traverse but benefited from the autonomous science capabilities of the rover, which provided additional science return from the independent rover traverse path, and enhanced astronaut flexibility and freedom to explore independently.

For all three sites (both year 1 and year 2), the astronaut(s) had the flexibility to adjust their exact path in real time using geologist-trained eyes to thoroughly explore the local geology, collect samples from locations inaccessible by the rover, and navigate to topographic highs to gain essential perspective views and geologic context. Prime objectives of the astronaut (s) included accessing terrain and reaching outcrops not navigable by the rover, digging trenches, and collecting samples—actions the rover was not equipped to do. Rendezvous stops were strategically chosen at areas of interest where the astronaut(s) could conduct collaborative activities with the rover (e.g., digging a trench for rover measurements of subsurface materials, scans of outcrops, including spectral and XRD measurements as well as GRS spectral accumulations, etc.). The rover instruments and in situ science analysis capabilities were used for measurements of astronaut-collected samples with real-time results communicated both to the astronaut (sites 1 and 2) and to the science team (site 3); a relatively quick assessment of these results enabled real-time assimilation of new or unexpected information that was actionable within the EVA time frame (M. Banks et al. 2024, in preparation).

The "astronaut/rover collaborative exploration" approach used specifically at the Yellow Cat Flat site (site 3) resulted in two separate contemporaneous EVAs of the same field site with both the astronauts and robot operating in a way that was responsive to ongoing observations, even without the iterative feedback from human operators. The command cycle for scenario 3 is delineated in Table 6.

### *3.7. Exploration Metrics*

We established metrics to compare the rover-directed exploration with the human-directed exploration (Table 7). Our objective was to compare the operational efficiency and the science yield for all three scenarios, including providing insight regarding the value added by astronaut/rover collaborative exploration subsequent to the rover-directed exploration.

### *3.8. Independence of Science Team Assessment*

Given that there was only one science team tasked for all three scenarios, cross-contamination of knowledge between scenarios was unavoidable. We attempted to minimize the cross-contamination between scenarios by executing scenario 1 first (human directed), followed by scenario 2 (rover directed). The traverse decisions and hypothesis testing were performed by the science team in scenario 1 and primarily by the rover in scenario 2, so it was possible to execute scenario 2 without much contamination from scenario 1 as long as the hypothesis map built by the science team was developed and locked in before execution of scenario 1. The only instance where information learned from scenario 1 could influence scenario 2

**Table 8**
Data Sets Available to the Science Team for Preparatory Work

| Data Set | Pixel Scale | Spectral Range (Bands)/Resolution |
|---|---|---|
| Google Earth Aerial Imagery | ∼0.5 m pixel$^{-1}$ | RGB (3 bands) |
| AVIRIS | Site 1: 15.3 m pixel$^{-1}$ | 0.35–2.5 $\mu$m (224 bands), |
| | Site 2: 15.1 m pixel$^{-1}$ | 10 nm channel$^{-1}$ |
| | Site 3: ∼16 m pixel$^{-1}$ | |
| ASTER | VNIR 15 | VNIR: 0.52–0.86 $\mu$m (3 bands) |
| | SWIR: 30 m pixel$^{-1}$ | SWIR: 1.6–2.4 $\mu$m (6 bands) |
| | TIR: 90 m pixel$^{-1}$ | TIR: 8.12–11.65 $\mu$m (5 bands) |
| ASTER DTM | 30 m pixel$^{-1}$ | |

was at the Yellow Cat Flat site (second field season), where a second cycle of scenario 2 was executed.

There was no way during scenario 3 (astronaut/rover collaborative exploration) to prevent the science team from using the knowledge acquired during scenarios 1 and 2, so instead we opted to focus on understanding the added value of a follow-up astronaut sortie that addressed questions developed during the knowledge gathering of scenarios 1 and 2.

### 3.9. Preparation

Preparatory work by the science team included analysis of remote-sensing data sets (Table 8) to identify photogeologic units within each future field site and establish hypotheses relating to the geology of each unit. In parallel, AVIRIS hyperspectral images were processed using the Tetracorder expert system (R. N. Clark et al. 2003, 2024), hereafter "Tetracorder," to generate mineral maps, which were in turn used to prepare a geologic origin cube and associated uncertainty map.

The photogeologic units were defined by a science team using a combination of the mineralogical maps derived from hyperspectral images acquired with AVIRIS and from high-resolution visible color aerial images. All pixels within a unit were assumed to share the same set of geologic origin probabilities, and all measurements performed by the rover within a unit contributed to the geologic interpretation of that unit (Figure 1).

Once the pre-field analysis was performed, the science team identified desired science stops and defined a traverse for the rover in order to visit these required points for investigation. These science stops were selected on the basis of spectral or mineralogic "hot spots" (spatially coherent regions of high parameter or mineralogical parameter value), or photogeologically interesting areas.

Finally, the science team defined sequences of observations that the rover would perform with its remote-sensing suite at science stops and during traverses between them.

Figure 2 shows the photogeologic map obtained from Google Earth data produced for site 3 (Yellow Cat Flat) overlaid on high-resolution imaging data. The units shown in these maps were delineated by the science team based on several criteria, including terrain color (RGB), morphology, stratigraphy, and mineralogic distribution.

## 4. Field Sites

Three field sites were selected based on their science value, degree of complexity, and traversability. We visited the first two sites during the first field season and the third site a year later during the second field season. Lessons were learned with each site visit, and consequently, operations were incrementally amended for each site as learned lessons were applied to improve operations. A team geologist performed an independent field survey of the sites to establish a knowledge base, against which the science team's findings in each scenario were compared. This geologist did not form part of the science team tasked in scenarios 1–3.

Site 1, selected for its traversability and geologic simplicity, provided both the science and rover teams a training ground to practice operations and science analysis. The site consisted of three major geologic units with very little intra-unit variability. It was also mostly flat with few obstacles that could complicate traversability. However, some escarpments in the northwest section did present some challenges for the rover. Site 2 was more challenging from both operational and scientific perspectives and provided a more robust test of the autonomous science system. The site consisted of two major units with significant intra-unit variability and relief. Traversability of this site was challenging for the rover in all scenarios. Finally, site 3 presented a medium-level difficulty in terms of traversability and geologic complexity. It consisted of two major units with some intra-unit variability exposed on escarpments along the perimeter of the site and easily surmountable hummocks within the site. Site 3 also had virtually no vegetation cover, enabling better mineralogy to be derived compared to sites 1 and 2, where vegetation sometimes masked soils on rover traverses.

### 4.1. Site 1—Black Point Lava Flow

Three geologic units with members make up the region surrounding Black Point Lava Flow in northern Arizona (Figure 6). The lowest and youngest member observed at the field site was a generally flat-lying light-tan fossiliferous limestone to dolostone containing silica nodules, identified as the Harrisburg Member of the Lower Permian Kaibab Formation (E. D. McKee 1938; C. W. Cheevers and R. R. Rawson 1979). The Kaibab Formation was tilted at varying strikes and dips in the southwest portion of the field area, indicating faulting or folding. Above this unit were two members of the Lower Triassic Moenkopi Formation. The lowest of these two members was a fine-grained red sandstone to siltstone with ripple marks, identified as the Wupatki Member (E. D. McKee 1954; E. M. Shoemaker 1960). The Wupatki was observed to be generally flat lying, forming hummocky hills, and had at least one sinkhole identified in the field area. Farther up the section was a medium-to-coarse-grained red sandstone identified as the Shnabkaib Member of the Moenkopi Formation (E. D. McKee 1954). In the field site area, the Shnabkaib was generally characterized as a discontinuous cliff-forming unit with cross-stratified beds. At the top of

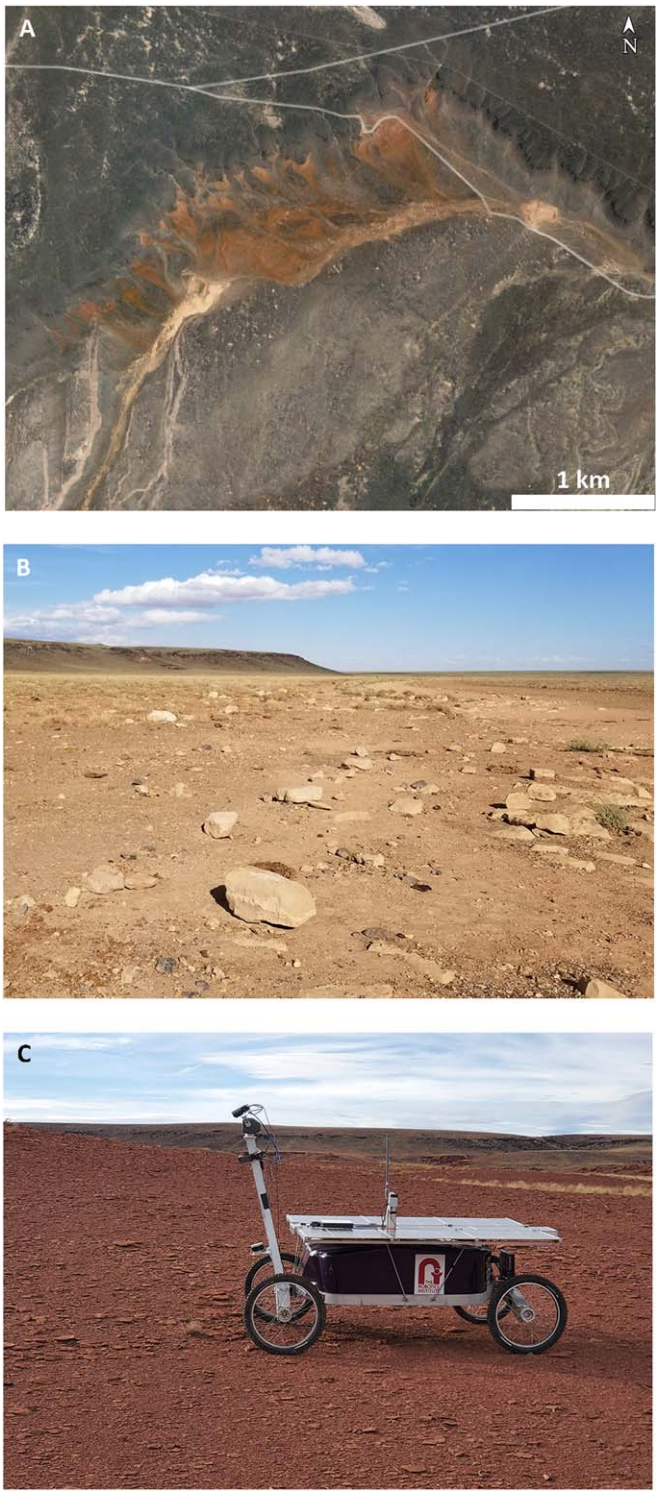


**Figure 6.** Site 1. (a) RGB color composite image of the site showing three dominant color units: the Black Point Lava Flow near the top, the reddish Moenkopi shale left of center, and the tan Kaibab rocks at the bottom. North is up. (b) View of the Black Point Lava Flow in the distance from the Kaibab formation. The boulder in the foreground is about 30 cm across. (c) The rover on red Moenkopi shale.


**Figure 7.** Site 2. (a) RGB composite of the Blue Canyon. Yellow inset location of inset. (b) Inset showing the tan Dakota Sandstone at the bottom of the image and the dark, layered Mancos Shale at the top. North is to the top left. (c) The rover traversing rugged terrain in the Mancos Shale.

the sections was a much younger, dark, generally vesicular basalt flow. The basalt flow was found to vary in thickness from 0.5 to 3 m in the field site area and formed a resistant capping unit. Phenocrysts from 1 mm to 5 cm of calcium–sodium plagioclase were commonly observed, and rare phenocrysts of olivine 1–2 mm in size were identified. Previous studies have determined that the Black Point Lava Flow unit is Pliocene in age (G. E. Ulrich & N. G. Bailey 1987; S. L. Hanson 2006).

### 4.2. Site 2—Blue Canyon

The Blue Canyon (AZ) field site area is characterized by two major units (Figure 7). The lowest is a white, medium-grained sandstone that transitions to shale and coal beds farther up the section, identified as Dakota Sandstone (Upper and Lower Cretaceous). At the field site area, the sandstone was observed to contain cross-bedding in areas, as well as kaolinite cementation, and included large amounts of iron concretions ranging in size from 1 to 10 cm. This white sandstone graded into beds of siltstone to fine sandstone with some beds of carbon-rich siltstone and lignite coal. The siltstone layers contained ripples, shell fossils, and fossilized wood. Exposed portions of the coal bedding were inferred to have caught on fire, exhibiting locally altered shale areas that contained a natural impure glass slag. Areas where unignited coal beds had been exposed exhibited weathering to sulfate minerals of jarosite, alunite, and gypsum (mineralogy confirmed with VNIR and MIR spectroscopy), likely due to weathering (oxidation) of sulfides in the coal and geochemical interactions with carbonate beds. This unit dominated the western edge of the field area and formed a monocline with varying dip and a generally north strike. Toward the central and eastern sides of the field site the bedding dip shallowed with more of the siltstones and coal layers preserved and capped by a younger second unit. This younger second unit was identified as the Mancos Shale (Upper Cretaceous; J. W. Harshbarger et al. 1958; D. D. Haynes & R. J. Hackman 1978) and was mainly characterized by dark, gray, expansive clays with thin beds of fossiliferous carbonate and salts. Highly broken fossils of Gryphaea, ammonites, coral, and shark teeth were found in these layers. The highly broken nature of these fossils and the fine-grained nature of the lithified sediments surrounding them suggest that this unit was deposited in the deeper ocean with shell fragments transported and deposited during storm events.

### 4.3. Site 3—Yellow Cat Flat

The Yellow Cat Flat (UT) field area consisted of three main geologic units: the Cretaceous Yellow Cat member (Kcmy) of the Cedar Mountain Formation; the Jurassic, Brushy Basin member of the Morrison Formation (JMB); and the Jurassic Saltwash member of the Morrison formation (JMS) (Figure 8). Within the field area were veins of amorphous silica and several twentieth-century uranium mines, suggesting that this region underwent low-grade mineral alteration (H. H. Doelling & P. A. Kuehne 2013).

JMB dominated the central portion of the field area and generally consisted of flat-lying montmorillonitic clays with lenses of chert, sandstone, and siltstone. Additionally, in the far southwest portion of the field area, there were outcrops of conglomerates. JMB is a sedimentary unit whose deposition is thought to have occurred in a fluvial-lacustrine setting, with the lacustrine setting tending toward playas. JMB is made up of up to 50% by volume altered vitric ash, in the form of aluminum smectite (T. Bell 1986).

JMS was primarily located in the southeast portion of the field area and was made up of resistant, fine-grained, quartz-arenite sandstones that overlay siltstone. It is considered to be fluvial in origin (A. R. Kirk & S. M. Condon 1986b, 1986a). Kcmy mainly forms cliff walls in the north and northwest portions of the field area and consists of alternating beds of siltstone, sandstone, and mudstone. This material was predominantly observed by our investigation as float near the base of the steep escarpments. The mudstones originated as floodplains deposits and show evidence of pedogenesis (R. M. Joeckel et al. 2023).

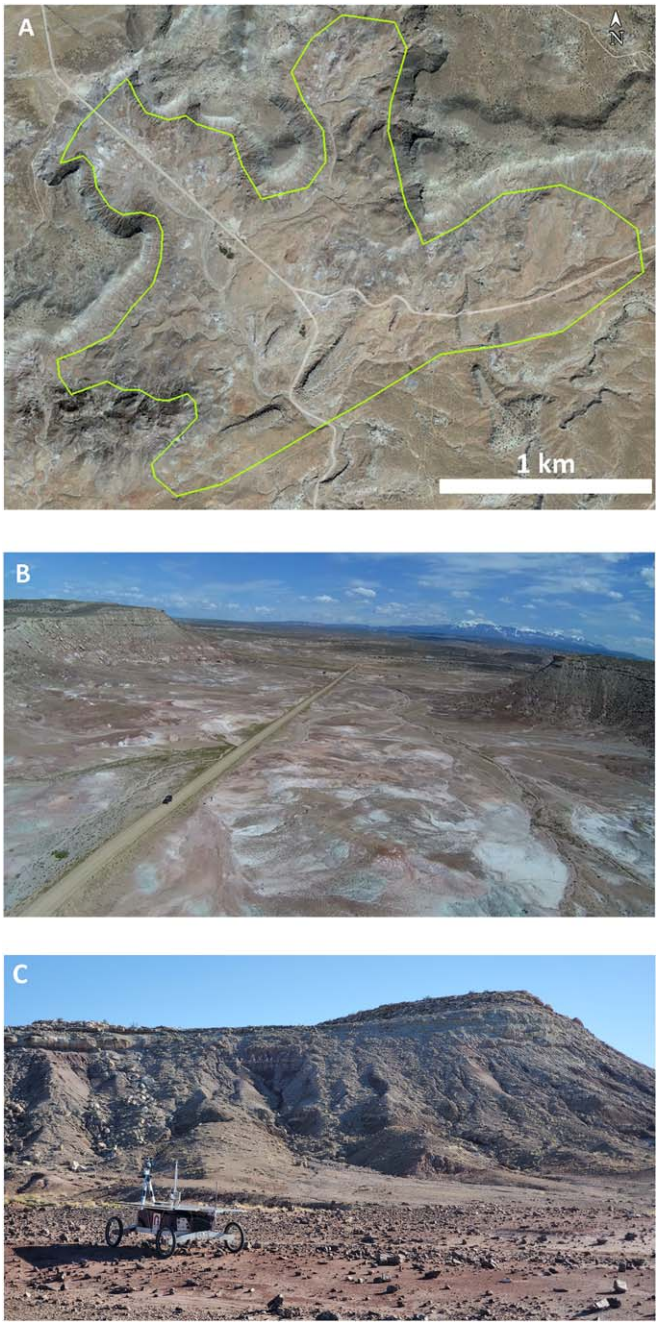


**Figure 8.** (a) RGB composite of the Yellow Cat Flat. The yellow outline denotes the site boundaries. (b) Aerial view of the northwest portion of the field site, showing strong color variability exposed at the site. (c) Eastward view across the field site to the cliff-forming Yellow Cat member.

## 5. Results and Discussion

We compared the geologic origin hypothesis evolution for each unit between exploration scenarios 1 (human-directed) and 2 (rover directed) to assess the accuracy in geologic interpretation provided by each scenario. For scenario 2, the

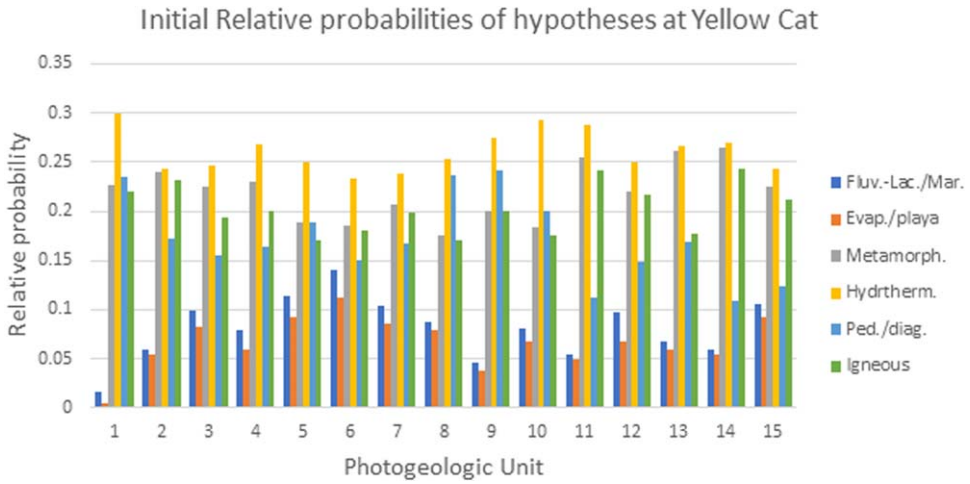


**Figure 9.** Initial relative probabilities, all units.

initial hypothesis map produced by the science team used by the rover was generated using Tetracorder and the Geologic Origin table, so the hypotheses were described probabilistically. This hypothesis map was also used by the science team as their priori for scenario 1. Figure 9 plots the relative probabilities of each geologic origin hypothesis encoded into the initial hypothesis map. It is notable that for each individual unit multiple hypotheses have similar weights and hence the relative initial uncertainty is high. As new data were acquired and analyzed during each scenario, additional information constrained the geologic origin of each unit, thus decreasing the relative uncertainty. This progressive analysis strategy is illustrated for scenario 2 in Figures 10 and 11 for the rover-directed exploration scenario.

Figure 10 shows an example of the evolution of competing geologic origin hypotheses of some units during our rover-directed exploration (scenario 2) at site 3 (Yellow Cat Flat) as new measurements were acquired, and Figure 11 shows the locations of each measurement. The hypothesis map was updated at each science stop after measurements were acquired and the spectra were analyzed. It is notable that probabilities trended toward stable values within a few tens of measurements, with one hypothesis (typically fluvio-lacustrine/marine) usually becoming distinctly dominant. Figure 12 shows the final relative probabilities of the photogeologic units visited by the rover during scenario 2 at site 3. For most units, the final relative probability of the fluvio-lacustrine/marine hypothesis markedly exceeded that of other hypotheses. However, we note that most units are not entirely dominated by a single hypothesis; hydrothermal and pedogenic/diagenetic origin hypotheses are weighted toward 10%–20% likelihood in many of the units that were visited. Our experience in the field taught us that hypothesis maps that converged toward more than one hypothesis occurred at locations where post-depositional processes altered the sediments; for example, diagenetic and low-grade metamorphic processes altered the fluvially deposited sediments explored at site 3 (Figure 10).

Table 9 compares results from scenario 1 (human-directed) and scenario 2 (rover-directed) exploration. All hypotheses within a 5% probability of the maximum probability value for the photogeologic unit are listed and are considered to be viable. Both the science-team-directed exploration and rover-directed exploration scenarios constrained the number of competing hypotheses toward the correct interpretation relative to that published in the literature.

### 5.1. Operational Efficiency and Science Yield

We are interested in understanding how the operational efficiency and science yield are affected in each scenario. Table 10 lists the total simulation time for each scenario at site 3 (year 2), as well as the rate of data acquisition, distance traveled per hour, and number of science stops performed per hour. While most aspects of our different scenarios are difficult to quantify, we found these parameters to be most easily quantifiable for comparison purposes. We outline the results here for site 3 (Yellow Cat Flat). Our metric for science yield is taken here to be represented by the rate of data acquisition, and the operational efficiency is given by the track length traveled per hour.

The rover-directed exploration covered greater distance and visited more stops per hour (had higher operational efficiency) in comparison to the human-directed exploration. For example, distance traveled per hour by the rover was roughly doubled in the rover-directed exploration. This result was anticipated, as it would be expected that operational efficiency will decrease whenever science team analysis and decision-making processes require time between operations. Operational efficiency was greatly enhanced in the astronaut/rover collaborative exploration, particularly due to the separate contemporaneous EVA traverses. It should be noted that the rover experienced some operational issues during scenario 3 (astronaut/rover collaborative exploration) at site 3 (Yellow Cat Flat) that prevented it from moving for significant periods of time, and thus it did not travel the distance it would have under nominal conditions. Under nominal operations, distance traveled would have been similar to that for scenarios 2 and 2b (Table 10). We note that while the rover was not able to function nominally, the astronauts could continue along their traverse collecting data, demonstrating an advantage of the two separate but complementary traverses.

In terms of science yield, the rate of data acquisition (and hence potential discovery) is greater in the rover-directed exploration scenario compared to the human-directed exploration. This yield difference is particularly apparent in the increased acquisition of imaging and spectra with the mast-mounted spectrometer (Table 10). We note that the number of contact-probe measurements was constrained to be the same between scenarios 1 and 2. As can be expected, the science yield was highest for the astronaut/rover collaborative exploration (see Section 6.1 for further discussion). Although the additional data gain did not influence the final conclusions regarding

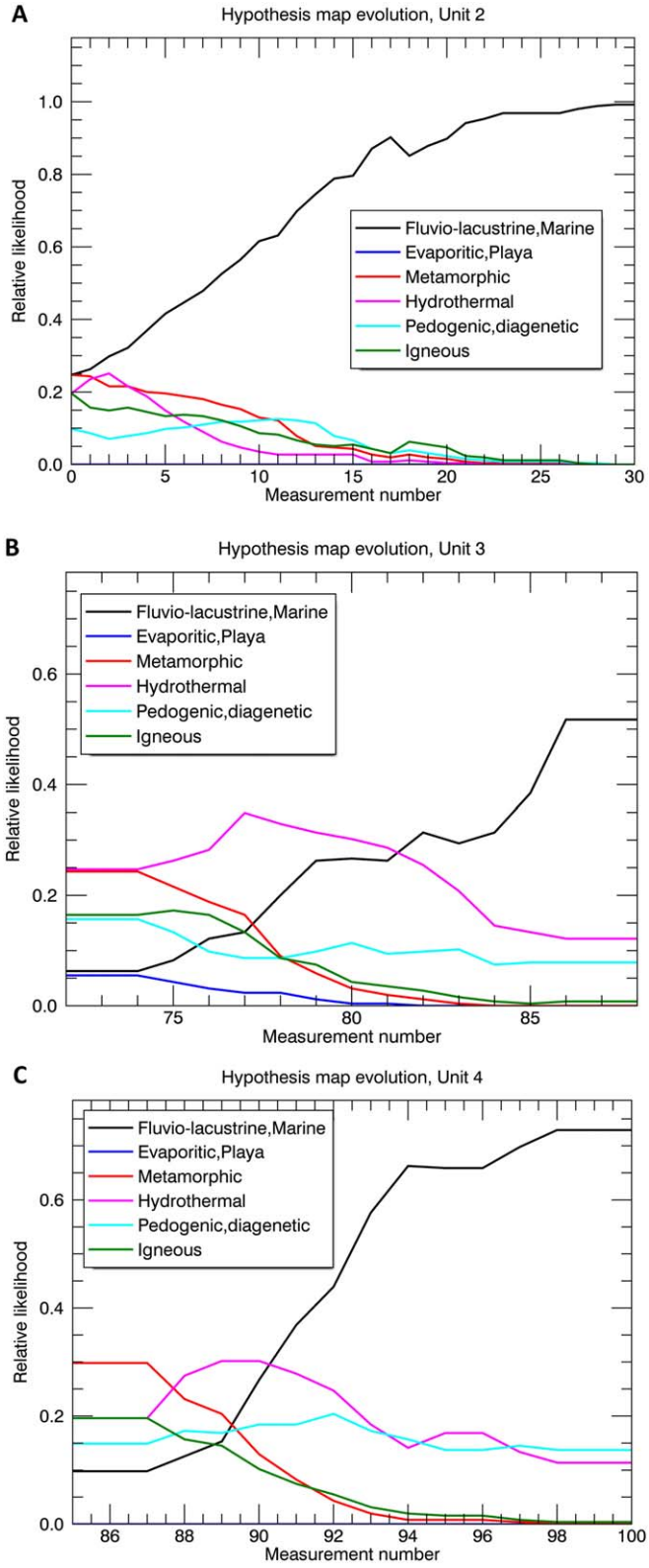


**Figure 10.** Changes in the relative likelihood of competing geologic origin hypotheses in response to measurements performed by the rover in scenario 2 (rover-directed exploration). (a) Evolution of hypotheses for unit 2. (b) Evolution of hypotheses for unit 3. (c) Evolution of hypotheses for unit 4. Note the rapid growth of the likelihood for the fluvio-lacustrine/marine hypothesis in all cases.

geologic origin (probabilities converged within 10–20 measurements), the additional observations, samples, data, images, and measurements that were acquired during the rover-directed

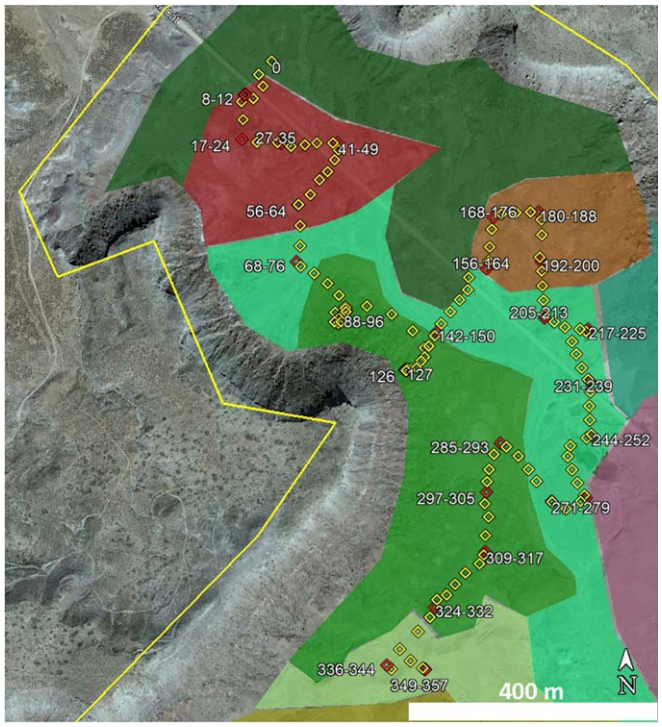


**Figure 11.** Locations of measurements performed by the rover during scenario 2b at Yellow Cat Flat site (site 3; year 2). Yellow diamonds represent measurements performed during traverses; red diamonds represent measurements performed at science stops. Numbers indicate the measurement performed by the rover with the mast-mounted ASD, starting at 0. For clarity, only measurements performed at science stops are indicated by the numbers.

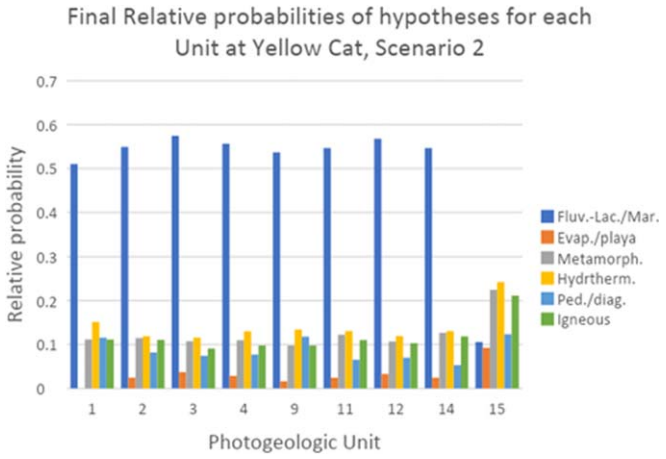


**Figure 12.** Scenario 2 (rover-directed exploration) final relative probabilities for visited units at the Yellow Cat Flat site 3 (year 2).

exploration and the astronaut/rover collaborative exploration represent an increase in the likelihood of new discoveries and capturing information that may be missed in human-directed rover exploration.

## 6. Discussion/Conclusions

Autonomous rover science exploration was shown to be operationally more efficient than our human-directed exploration in the decision/analysis loop, resulting in higher rates of data collection and science yield per command cycle, thus increasing the possibility of unexpected discoveries. Our field tests

**Table 9**
Comparison of Geological Interpretations by Scenario for Each Geologic Unit at Site 3

| Photogeologic Unit | 1 | 2 | 3 | 4 | 5 | 6 | 7 | 8 | 9 | 10 | 11 | 12 | 13 | 14 | 15 |
|---|---|---|---|---|---|---|---|---|---|---|---|---|---|---|---|
| Initial hypothesis[a] | Hyd | LgM, Hyd, Ign | LgM, Hyd | Lgm, Hyd | Hyd | Lgm, Hyd | LgM, Hyd, Ign | Hyd, Ped | Hyd, Ped | Hyd | Hyd, LgM, Ign | Hyd, Lgm, Ign | Hyd, LgM | Hyd, LgM, Ign | Hyd, Lgm, Ign |
| Scenario 1 all instr. final | Sed[b] → Hyd → LgM | Sed[b] → Hyd → LgM | Sed[b] → Hyd → LgM | Sed[b] → Hyd → LgM | Sed[b] → Hyd → LgM | | Sed[b] → Hyd → LgM | | | Sed[b] → Hyd → LgM | | | Sed[b] → Hyd → LgM | Sed[b] → Hyd → LgM | |
| Scenario 2a VNIR +FTIR final | FLM | FLM | FLM | FLM | | | | | | | FLM | FLM | | FLM | FLM, H, I |
| Scenario 3 final Geologist | Fluvio-lacustrine in origin, with evidence of some low-grade metamorphism and pedogenesis | | | | | | | | | | | | | | |
| Geologic unit | Jmb (L, M) | Kcmy/Jmb (L, M, P) | Jmb | Jmb | Jmb/Jms | Jmb (M,P) | Jms/Qea | Jmb/ Qea | Jmb | Jmb/Qea | Jmb/Jms | Jmb | Jms | Jmb /Jms | Jmb |

**Notes.**
[a] FLM = fluvio-lacustine/marine; Hyd = hydrothermal; LgM = low-grade metamorphic; PD = pedogenic/diagenetic; Ign = igneous.
[b] Science team used sedimentary annotation to indicate provenance of material but did not elaborate on possible depositional mechanism.

**Table 10**
Metrics (from R. N. Clark et al. 2024b, in preparation)

| Metric | 2022 Oct 17–19 | 2022 Oct 20–21 | 2022 Oct 28 | 2022 Oct 26–27 |
|---|---|---|---|---|
| Simulation time (hours) | 20.9 | 9.0 | 3.4 | 12.5 |
| | Observations per Hour | | | |
| | Scenario 1 | Scenario 2[a] | Scenario 2b[a] | Scenario 3 (rover only) |
| ASD1 spectra | 12.42 | 42.9 | 92.7 | 18.5 |
| ASD2 spectra | 2.9 | 5.4 | * | 4.2 |
| FTIR spectra | 2.7 | 4.5 | 7.6 | 4.2 |
| Rover-camera images | 11.5 | 42.0 | 63.2 | 9.8[c] |
| Close-up images | 1.9 | 4.2 | * | - |
| Micro_images | 1.5 | 4.5 | * | 2.8 |
| UV Spectra | 2.6 | 4.2 | * | 3.8 |
| Number of stops | 0.5 | 4.54 | 7.0 | 2.3 |
| Track length (km) | 0.4 | 0.59 | 0.87 | 0.24[d] |
| Astronaut (scenario 3 only): | | | | |
| Simulation time (hours) | | | | 18.1 |
| Track length (km) (average per hour including stops, sample collection, photos, and other activities) | - | - | - | 0.6 |
| Number of science stops per hour[b] | - | - | - | 2.8 |
| Number of samples (per hour) | - | - | - | 1.9 |
| Number of images (per hour) | - | - | - | 13.6 |

**Notes.**
ASD1 = rover spectrometer, 0.35–2.5 $\mu$m.
ASD2 = contact spectrometer, 0.35–2.5 $\mu$m.
FTIR = contact spectrometer, 2.5–15.4 $\mu$m. Dash = not done.
[a] In scenario 2, the rover used a search radius of 50 m to identify the region of greatest uncertainty in the updated uncertainty map (or science-team-selected science stop) and plan a traverse to it. In scenario 2b, we explored how the results would vary if the rover used a search radius of 100 m instead. Acquisition with the ASD2 contact, UV, close-up, and micro images could be obtained during each science stop but was not performed in scenario 2b.
[b] Includes only science stops directed by the science team (does not include interim stops for imaging, sample collection, and science observations).
[c] Due to the images that were being acquired by the astronauts, the rover was directed not to capture images at each stop in the same operation as it was in scenarios 2 and 2b.
[d] The rover experienced some operational downtimes during scenario 3 at this site that prevented it from moving for significant periods of time, and thus it did not travel the distance it would under nominal conditions. Under nominal operations, distance traveled would have been similar to that indicated for scenarios 2 and 2b. We note that while the rover was not able to function nominally, the astronauts could continue along their traverse collecting data, demonstrating an advantage of the two independently functioning but complementary traverses. Downtime was not included in the simulation time.

highlighted several important aspects of rover science autonomy that will help improve future autonomous field exploration. In particular, we found that despite the fact that a rover capable of science autonomy can accomplish higher operational efficiency and science yield than a human-directed rover per command cycle, iterative testing and updating of the hypothesis map by the rover and the science team in between command cycles are critical for its successful implementation. Such iterations are essential, as hypothesis map updates and decision-making are critically reliant on the accuracy of data analysis tools and the science interpretation table. During our first field season, an incomplete representation of the geologic origin of a single, repeatedly found mineral (kaolinite) resulted in a systematically incorrect assessment of geologic origin (hydrothermal, whereas pedogenic should have also been included in the interpretation). In this case, it became apparent that executing an additional scientist/rover cycle of hypothesis map updating would have led to the identification of the problem and its correction, allowing more accurate results to be obtained in the subsequent cycle.

### *6.1. Astronaut/Rover Collaboration*

Overall, the integration of EVA astronaut operations simultaneously with rover investigations, and in coordination with a science team, synergized well with the rover's autonomous capabilities. As compared to the rover-directed exploration alone, this human/robot collaboration allowed for (1) collection of samples; (2) an increase in the overall spatial coverage of the field area (rover + astronaut distance traveled; Table 10; Figure 13), which facilitated imaging and measurements of materials over a greater fraction of the field site; (3) an increased pace in the real-time evolution of the scientific hypotheses; and (4) the in situ assimilation of data and observations (M. Banks et al. 2024, in preparation).

An essential advantage of the astronaut/rover collaboration was the ability of the astronauts to perform tasks and to physically access locations that were beyond the capabilities of the rover yet were critical to the scientific interpretation of the exploration area. Complementarily, rovers hypothetically can access some areas that would be too dangerous for humans to explore. A second factor was the critical observational abilities of the geologically trained astronauts. Unlike the rover, astronauts were able to recognize the trade-offs between time and value of traversing to and assessing additional areas. Astronauts could select and collect representative samples for subsequent in situ analyses by the rover, and these samples are then available for later in-depth analyses with equipment at a deployed habitat or back on Earth. Importantly, the astronauts could track specific geologic features and layers across the field area and quickly assess an overall interpretation and characterization of the geologic origin/history of the site.

Real-time and rapid evolution of the scientific hypotheses was also a direct result of (1) the coordinated evaluations of astronaut observations and sampling between the astronauts

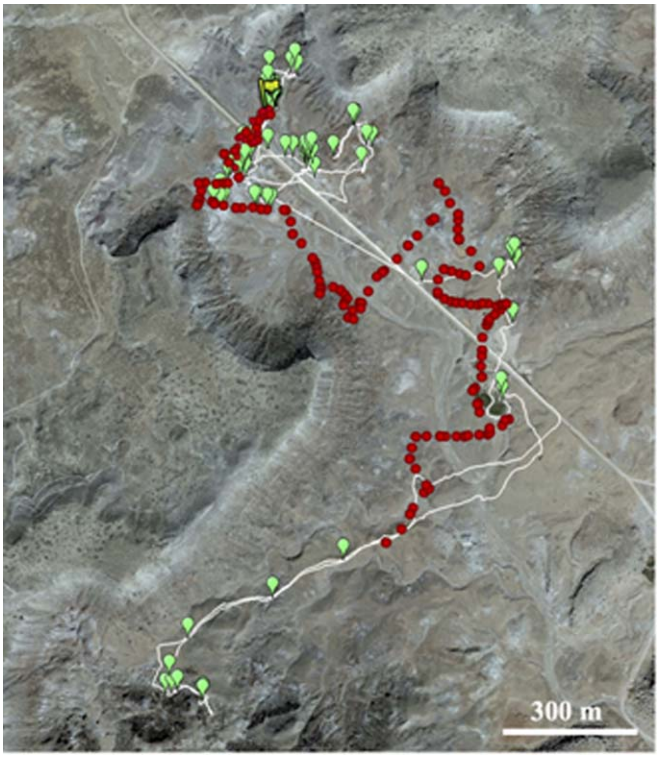


**Figure 13.** Path of the astronauts (white line) during scenario 3 (astronaut/rover collaborative exploration) superposed on a shaded-relief map of the Yellow Cat Flat site (site 3; year 2). Green markers indicate locations of science-team-selected astronaut science stops, locations of astronaut imaging, sample collection, and other activities. The rover traverse is marked with red circles. As can be seen in several locations, particularly the lower portion of the figure, the astronauts were able to navigate to and within topography that could not be traversed by the rover. Simultaneously, the rover was exploring nearby terrain, providing a separate but complementary set of EVA data to the science team. The astronaut and rover met up at several predetermined rendezvous stops for in situ measurements of astronaut-collected samples with rover instruments. Note that, due to operational complications during this scenario, the rover was not able to traverse to some of these points; the rendezvous was alternatively simulated by a member of the rover team and thus is not apparent in the rover traverse shown here. Each day the astronauts returned to a simulated habitat marked with the yellow flag.

and the science team and (2) the real-time in situ analysis of measurements acquired by the rover. The science team was able to be the focal point of the data flow from both the astronauts and the rover and to use discussions with the astronauts (which included real-time observational data) to facilitate an increase in the contextual understanding of the geology of the site at a faster pace than that achievable by the astronauts or rover operations alone.

In applications to lunar and planetary exploration, astronaut/rover collaborative exploration has the benefit of minimizing the astronauts' time of exposure to the hazards of EVAs, therefore reducing risk per scientific sortie. The remote-sensing, compositionally focused, rover-directed exploration performed in this work might miss gathering useful visual environmental clues and would be slowed significantly if the rover conducted any operations other than simple remote-sensing analyses (e.g., sample drilling/collection). If supported, our findings indicate that an astronaut/rover collaboration significantly increases both the operational efficiency and the total scientific return from a field site in comparison to an equivalent EVA duration without real-time coordinated astronaut/rover operations (M. Banks et al. 2024, in preparation).

### 6.2. Planetary Exploration Strategies

The three scenarios tested in this work are not necessarily mutually exclusive. As our investigation developed, it became apparent that an optimally efficient strategy for planetary exploration could be accomplished in three distinct stages:

1. Preparatory remote-sensing work leading to the generation of a hypothesis map by a science team.
2. Autonomous science exploration performed by a rover using the hypothesis map to provide a science team with new mineralogical insights (from Tetracorder) regarding the field site, and additional platform-based analyses that can be used to generate focused questions to be addressed by having an astronaut and rover visit specific sites.
3. Astronaut/rover collaborative exploration to address the newly posed questions by the science team.

### 6.3. Future Directions

As described in this work, hypothesis maps can provide marked improvements in operational efficiency and science yield. However, significant work remains to be done to explore the full potential of hypothesis maps. Directions for future development are described here.

#### 6.3.1. Diversity of Investigations

The hypothesis map is not limited to simple geologic exploration such as that tested in this work. Instead, the hypothesis map can be developed for any type of science autonomy given a hypothesis, a set of observables that addresses the hypothesis, the instrumentation to measure these observables, and the tools for a computer to analyze them to a relatively high level of confidence.

Continued extension of the Tetracorder analysis capabilities to include the ultraviolet and/or MIR spectral regions could significantly benefit mineral identification and hypothesis map development and improve constraints on geologic origin for any field site. Additionally, the Tetracorder system can also be utilized to analyze any type of patterned data, such as reflectance and emission spectra, Ramman spectra, XRD patterns, etc. Tailoring Tetracorder's data analysis capabilities to specific uses would allow the rover to extend its tool set to address a broader diversity of investigations.

For example, the VIPER mission will characterize the lateral and vertical distribution of ices in the lunar regolith around Mons Mouton, near the western rim of Nobile crater. The rover will carry a neutron spectrometer, an NIR (1.3–4 $\mu$m) spectrometer, and a mass spectrometer to constrain the composition and distribution of ices, as well as a drill to auger material from up to 1 m in depth (e.g., A. Colaprete et al. 2023). A hypothesis map and associated entropy map derived from ice stability predictions (e.g., M. Siegler et al. 2015; M. A. Siegler et al. 2022) could be used by the rover (or rover team) to plan traverses and select drill sites. Measurements with the instrument suite during traverses and at drill sites would allow the rover to update its hypothesis and entropy maps and plan new traverses and drill site locations that would further test the driving hypothesis.

#### 6.3.1.1. Unexpected Discoveries

New discoveries can be made by the rover in cases where measurements performed do not fall within the confines of the hypothesis map. Within the context of our investigation, such discoveries would be triggered by the identification of minerals that are not related to hypotheses in the geologic origins table. In our exercises, we used point spectrometers to acquire data, which is a slow technique that produces small amounts of data (each measurement with the mast-mounted spectrometer took 12 s, including stage movement). Hence, the rate of data production did not exceed the rate of transmission. However, greater rates of data acquisition would have been possible if a hyperspectral imager had been used, resulting in data acquisition rates that would exceed the data transmission budget. In such a case, rover science autonomy would allow for a more detailed exploration of the sites than would otherwise have been possible. We would expect this to result in a greater science yield and a greater opportunity for new discoveries. Such discoveries could be used as triggers to direct the rover to perform additional investigations autonomously.

#### 6.3.1.2. Human Exploration

In the context of future exploration of the solar system, robust robotic systems likely will play an important function, even as crewed missions take on a central role. We expect that not only will robotic systems assist astronauts in real-time field analyses and sample identification, selection, and collection; they also will be used to conduct initial exploration or reconnaissance of the site, carry and operate scientific analysis instruments (M. Banks et al. 2024, in preparation), complete repetitive planetary surface tasks, traverse to locations that are inaccessible to humans, and assist humans in the characterization and scientific exploration of human-accessible sites. The support that a rover could bring to human exploration would reduce many risks to astronauts (M. Banks et al. 2024, in preparation). The rover-assisted assessment of geological origin explored in this work is a demonstration of one of many possible applications of rover science autonomy. We envision that a capable rover, equipped with a well-developed science interpretation algorithm, robust data analysis tools, and a strategic hypothesis map, could be well utilized, not only in traditional scientific field exploration involving field personnel but also as a time-efficient and lower-cost scouting tool to improve the granularity of knowledge at a field site in advance of human exploration.

## Acknowledgments

This work was supported by the Solar System Exploration Virtual Institute (SSERVI16) Cooperative Agreement (NNH16 ZDA001N) (TREX). The research was carried out in part at the Jet Propulsion Laboratory, California Institute of Technology, under a contract with the National Aeronautics and Space Administration (80NM0018D0004). We thank the Hopi Tribe and Babbitt Ranches for their generous permission to use their land in support of our field exercises. We also thank the reviewers for their careful review and insightful comments.

## Appendix A
## Year 1 Geologic Origin Table

Table A1 contains the geologic origin lookup table used in the first field expedition to the Black-point lava flow and Blue Canyoun field sites. It relates individual entries in the USGS spectral library was used by the rover to potential geologic origins.

**Table A1**
Geologic Origin Lookup Table—Year 1—Sites 1 and 2

| Entry Name | Lacustrine/ Marine | Evaporitic/ Playa | Metamorphic | Hydrothermal | Pedogenic /Diagenic /Weathering (Include Secondary Coatings) | Igneous (Include Carbonatites) |
|---|---|---|---|---|---|---|
| actinolite.fd.gz | | | 1 | | 1 | |
| adularia_2.5um.fd.gz | | | | | | |
| alunite.33+kaol.33+musc.33.fd.gz | | | 1 | | 1 | |
| alunite.5+kaol.5.fd.gz | | | 1 | | 1 | |
| alunite.5+musc.5.fd.gz | | | 1 | | 1 | |
| alunite+kaolinite.muscovite.added.fd.gz | | 1 | | 1 | 1 | |
| alunite+musc+pyroph.fd.gz | | | 1 | | | 1 |
| alunite+pyroph.added.fd.gz | | | 1 | | | |
| alunite+pyrophyl.fd.gz | | | 1 | | | |
| amphibole.fd.gz | | | 1 | | | 1 |
| analcime.2.5um.fd.gz | | | | | | |
| anorthite_hs201.3b.fd.gz | | | | | | |
| borate_colemanite.fd.gz | 1 | 1 | | | | |
| borate_pinnoite.fd.gz | 1 | 1 | | | | |
| bytownite_hs106.3b.fd.gz | | | | | | |
| calcite.25+dolom.25+Na-mont.5.fd.gz | 1 | 1 | | | 1 | |
| calcite+0.2Na-mont.fd.gz | 1 | 1 | 1 | | 1 | 1 |
| calcite+0.5Ca-mont.fd.gz | 1 | 1 | 1 | | 1 | 1 |
| carbonate_aragonite.fd.gz | 1 | 1 | 1 | | | |
| carbonate_azurite.fd.gz | | | | | 1 | |
| carbonate_calcite_3.5um_curvc.fd.gz | 1 | 1 | 1 | | 1 | 1 |
| carbonate_calcite_3.5um.fd.gz | 1 | 1 | 1 | | 1 | 1 |
| carbonate_calcite.25+dolom.25+Ca-mont.5.fd.gz | 1 | 1 | 1 | | 1 | 1 |
| carbonate_calcite.fd.gz | 1 | 1 | 1 | | 1 | 1 |
| carbonate_calcite+0.2Ca-mont.fd.gz | 1 | 1 | 1 | | 1 | 1 |
| carbonate_calcite+0.2kaolwxl.fd.gz | 1 | 1 | 1 | | 1 | 1 |
| carbonate_calcite+0.3muscovite.fd.gz | 1 | 1 | 1 | | 1 | 1 |
| carbonate_calcite+dolomite.5.fd.gz | 1 | 1 | 1 | | 1 | 1 |
| carbonate_calcite0.7+kaol0.3.fd.gz | 1 | 1 | 1 | | 1 | 1 |
| carbonate_dolo+.5ca-mont.fd.gz | 1 | 1 | | | 1 | |
| carbonate_dolomite_3.5um_curvc.fd.gz | | | | | | |
| carbonate_dolomite_3.5um.fd.gz | | | | | | |
| carbonate_dolomite.5+Na-mont.5.fd.gz | 1 | 1 | | | 1 | |
| carbonate_dolomite.fd.gz | 1 | 1 | | | 1 | |
| carbonate_magnesite.fd.gz | | | | | 1 | 1 |
| carbonate_magnesite+hydromagnesite_curvc.fd.gz | | | | | | |
| carbonate_magnesite+hydromagnesite.fd.gz | | | | | | |
| carbonate_malachite.fd.gz | | | 1 | | | |
| carbonate_rhodochrosite.fd.gz | | | | | | |
| carbonate_rhodochrosite.fd.gz | | | 1 | | | |
| carbonate_siderite.fd.gz | | | 1 | | 1 | |
| carbonate_smectite_calcite.33+Ca-mont.67.fd.gz | | | | | | |
| carbonate_strontianite.fd.gz | 1 | 1 | | | 1 | |
| carbonate_trace_3.5um_curvc.fd.gz | | | | | | |
| carbonate_trace_3.5um.fd.gz | | | | | | |
| carbonate_witherite.fd.gz | | | 1 | | | |
| chloride_carnallite.fd.gz | | 1 | | | | |
| chlorite_clinochlore.fd.gz | | | 1 | | | |
| chlorite_clinochlore.fe.gds157.fd.gz | | | | | | |
| chlorite_clinochlore.fe.sc-cca-1.fd.gz | | | | | | |
| chlorite_clinochlore.nmnh83369.fd.gz | | | | | | |
| chlorite_cookeite-car-1.a.fd.gz | | | | | | |
| chlorite_cookeite-car-1.c.fd.gz | | | | | | |
| chlorite_thuringite.fd.gz | | | 1 | | | |
| chlorite-scarn.fd.gz | | | 1 | | | |
| chlorite.fd.gz | | | 1 | | | |
| chrysocolla.fd.gz | | | 1 | | 1 | |
| chrysotile.coarse-fibrous.fd | | | 1 | | | |
| chrysotile.fine-fibrous.fd | | | 1 | | | |

**Table A1**
(Continued)

| Entry Name | Lacustrine/ Marine | Evaporitic/ Playa | Metamorphic | Hydrothermal | Pedogenic /Diagenic /Weathering (Include Secondary Coatings) | Igneous (Include Carbonatites) |
|---|---|---|---|---|---|---|
| chrysotile.gypsum.wtc01-8.fd.gz | | 1 | 1 | | | |
| chrysotile.med-fine-fibrous.fd | | | 1 | | | |
| clay_hectorite.fd.gz | 1 | | | | 1 | |
| clintonite.fd | | | 1 | | | |
| copper_carbonate_azurite.fd.gz | | | | | 1 | |
| copper_carbonate_malachite.fd.gz | | | 1 | | 1 | |
| copper_chrysocolla.fd.gz | | | | | 1 | |
| copper_oxide_cuprite.fd.gz | | | | | 1 | |
| copper_precipitate_greenslime.fd.gz | | | | | | |
| copper_sulfate_bluefflor.fd.gz | | | | | | |
| datolite.fd.gz | | | | | | |
| diaspore.fd.gz | | | | | | |
| dick+musc+gyp+jar.amix.fd.gz | | | | | | |
| elbaite.fd.gz | | | | | | |
| epidote.fd.gz | | | 1 | | | |
| epidote.fd.gz | | | 1 | | | |
| eugsterite.2.5um.water.fd.gz | | | | | | |
| fe2+_chlor+muscphy.fd.gz | | | | | | |
| fe2+_chlorite.clinochlor.fd.gz | | | 1 | | | |
| fe2+_chlorite.Felow.clinochlor.fd.gz | | | 1 | | | |
| fe2+_chlorite.thuringite.fd.gz | | | 1 | | | |
| fe2+_chromite.fd.gz | | | 1 | | | 1 |
| fe2+_feldspar_albite.fd.gz | | | | 1 | | 1 |
| fe2+_feldspar_microcline.fd.gz | | | | | | 1 |
| fe2+_feldspar_orthoclase.fd.gz | | | | | | 1 |
| fe2+_feldspar.bytownite.fd.gz | | | | | | 1 |
| fe2+_goeth+musc.fd.gz | | | 1 | | | 1 |
| fe2+_olivine-fine-gr.fd.gz | | | 1 | | | 1 |
| fe2+_olivine-lrg-gr.fd.gz | | | | | | 1 |
| fe2+_pyroxene_augite.fd.gz | | | 1 | | | 1 |
| fe2+_pyroxene_clino_pigeonite.fd.gz | | | | | | 1 |
| fe2+_pyroxene_enstatite.fd.gz | | | 1 | | | 1 |
| fe2+_pyroxene_hedenbergite.fd.gz | | | 1 | | | |
| fe2+_pyroxene.bronzite.fd.gz | | | 1 | | | |
| fe2+_pyroxene.diopside.fd.gz | | | 1 | | | 1 |
| fe2+_pyroxene.hypersthene.fd.gz | | | | | | 1 |
| fe2+_wollastonite_hs348.3b.fd.gz | | | 1 | | | |
| fe2+fe3+_chlor+goeth.propylzone.fd.gz | | | | 1 | 1 | |
| fe2+fe3+_hematite_weathering.fd.gz | | | | | 1 | |
| fe2+fe3+_water_RTsludge.fd.gz | | | | | | |
| fe2+fe3+mix_with_hematite_br5b.fd.gz | | | | 1 | 1 | |
| fe3+_ferrihydrite.fd.gz | 1 | | | 1 | | |
| fe3+_goeth+jarosite.fd.gz | | | | 1 | 1 | |
| fe3+_goethite.coarsegr.ALL.fd.gz | 1 | | | 1 | 1 | |
| fe3+_goethite.coarsegr.fd.gz | 1 | | | 1 | 1 | |
| fe3+_goethite.fingr.fd.gz | 1 | | | 1 | 1 | |
| fe3+_goethite.lepidocrosite.fd.gz | | | | 1 | | |
| fe3+_goethite.medcoarsegr.mpc.trjar.fd.gz | | | 1 | 1 | | |
| fe3+_goethite.medgr.fd.gz | 1 | | | 1 | 1 | |
| fe3+_goethite.medgr.ws222.fd.gz | 1 | | | 1 | 1 | |
| fe3+_goethite.thincoat.fd.gz | | | | 1 | 1 | |
| fe3+_goethite+qtz.medgr.gds240.fd.gz | | | | 1 | | |
| fe3+_hematite.all.fd.gz | 1 | | | 1 | | |
| fe3+_hematite.fine.gr.all.fd.gz | 1 | | | 1 | | |
| fe3+_hematite.fine.gr.fe2602.fd.gz | 1 | | | 1 | | |
| fe3+_hematite.fine.gr.gds76.fd.gz | 1 | | | 1 | | |
| fe3+_hematite.fine.gr.ws161.fd.gz | 1 | | | 1 | | |
| fe3+_hematite.lg.gr.all.fd.gz | 1 | | | 1 | | |
| fe3+_hematite.lg.gr.br25a.fd.gz | 1 | | | 1 | | |
| fe3+_hematite.lg.gr.br34c.fd.gz | 1 | | | 1 | | |
| fe3+_hematite.med.gr.all.fd.gz | 1 | | | 1 | | |

**Table A1**
(Continued)

| Entry Name | Lacustrine/ Marine | Evaporitic/ Playa | Metamorphic | Hydrothermal | Pedogenic /Diagenic /Weathering (Include Secondary Coatings) | Igneous (Include Carbonatites) |
|---|---|---|---|---|---|---|
| fe3+_hematite.med.gr.br25b.fd.gz | 1 | | | 1 | | |
| fe3+_hematite.med.gr.gds27.fd.gz | 1 | | | 1 | | |
| fe3+_hematite.nano.BR34b2.fd.gz | 1 | | | 1 | | |
| fe3+_hematite.thincoat.fd.gz | | | | 1 | 1 | |
| fe3+_maghemite.fd.gz | | | 1 | | | |
| fe3+_smectite_nontronite.fd.gz | | | | | 1 | |
| fe3+_sulfate_jarosite_br34a2.fd.gz | | | | 1 | 1 | |
| fe3+_sulfate_kjarosite200.fd.gz | | | | 1 | 1 | |
| fe3+_sulfate_schwertmannite.fd.gz | | | | | 1 | |
| fe3+bearing1.fd.gz | | | | | | |
| fe3+copper-hydroxide_pitchlimonite.fd.gz | | | | 1 | | |
| fe3+fe2+_sulfate_copiapite.fd.gz | | | | | 1 | |
| fe3+fe2+_sulfate_coquimbite.fd.gz | | | | | 1 | |
| fe3+mix_AMD.assemb1.fd.gz | | | | | 1 | |
| fe3+mix_AMD.assemb1+2.fd.gz | | | | | 1 | |
| fe3+mix_AMD.assemb2.fd.gz | | | | | 1 | |
| fe3+mn_desert.varnish1.fd.gz | | | | | 1 | |
| fe3+mn_desert.varnish2.fd.gz | | | | | 1 | |
| feldspar_buddington.namont.fd.gz | | | | 1 | | |
| feldspar_buddington.namont2.fd.gz | | | | 1 | | |
| feldspar_buddingtonite_ammonium.fd.gz | | | 1 | | | |
| goethite_3.17um.fd.gz | 1 | | | 1 | 1 | |
| grossular_3.17um.fd.gz | | | 1 | | | |
| hornblende.fd.gz | | | 1 | | | 1 |
| howlite.fd.gz | | 1 | | | | |
| hydrogrossular.fd.gz | | | 1 | | | |
| hydroxide_brucite.fd.gz | | | 1 | 1 | 1 | |
| hydroxide_diaspore.fd.gz | | | 1 | | | |
| hydroxide_gibbsite.fd.gz | | | | | 1 | |
| inosilicate_pectolite.fd.gz | | | | 1 | | |
| jarosite_3.18um.fd.gz | | | | | 1 | |
| Kalun+kaol.intmx.fd.gz | | | | 1 | 1 | |
| kaol.75+alun.25.fd.gz | | | | | 1 | |
| kaol.75+pyroph.25.fd.gz | | | | 1 | | |
| kaolgrp_dickite.fd.gz | | | | 1 | 1 | |
| kaolgrp_halloysite.fd.gz | | | | 1 | 1 | |
| kaolgrp_kaolinite_pxl.fd.gz | | | | 1 | 1 | |
| kaolgrp_kaolinite_wxl.fd.gz | | | | 1 | 1 | |
| kaolin.3+smect.7.fd.gz | | | | | 1 | |
| kaolin.5+muscov.medAl.fd.gz | | | | 1 | | |
| kaolin.5+muscov.medhighAl.fd.gz | | | | 1 | | |
| kaolin.5+smect.5.fd.gz | | | | | 1 | |
| kaolin+musc.intimat.fd.gz | | | | 1 | | |
| kaolinite.3+.5+smectite.5+.7.added.fd.gz | | | | 1 | | |
| kaolinite+muscovite.added.fd.gz | | | | 1 | | |
| magnetite_hs195.3b.or.olivine.fd.gz | | | | | | 1 |
| magnetite.fd.gz | | | 1 | | | 1 |
| micagrp_biotite.fd.gz | | | 1 | | | 1 |
| micagrp_illite.fd.gz | | | | 1 | 1 | |
| micagrp_illite.gds4.fd.gz | | | | 1 | 1 | |
| micagrp_illite.roscoelite.fd.gz | | | | 1 | 1 | |
| micagrp_lepidolite.fd.gz | | | | 1 | | 1 |
| micagrp_margarite.fd.gz | | | | | 1 | |
| micagrp_muscovite-low-Al.fd.gz | 1 | | 1 | 1 | | 1 |
| micagrp_muscovite-med-Al.fd.gz | 1 | | 1 | 1 | | 1 |
| micagrp_muscovite-medhigh-Al.fd.gz | 1 | | 1 | 1 | | 1 |
| micagrp_muscoviteFerich.fd.gz | 1 | | 1 | 1 | | 1 |
| micagrp_paragonite.fd.gz | | | 1 | | | |
| microcline_hs103.3b.fd.gz | | | 1 | 1 | | 1 |
| mn_oxide_pyrolusite.fd.gz | 1 | | | | 1 | |
| Mn-Coating.fd.gz | | | | | | |

**Table A1**
(Continued)

| Entry Name | Lacustrine/ Marine | Evaporitic/ Playa | Metamorphic | Hydrothermal | Pedogenic /Diagenic /Weathering (Include Secondary Coatings) | Igneous (Include Carbonatites) |
|---|---|---|---|---|---|---|
| mn2+_rhodonite.fd.gz | | | 1 | 1 | | |
| musc+gyp+jar+dick.amix.fd.gz | | | | | | |
| musc+jarosite.intimat.fd.gz | | | | | | |
| musc+pyroph.fd.gz | | | 1 | 1 | | |
| muscovite+chlorite.fd.gz | | | 1 | 1 | | 1 |
| Na-alun+kaol.intmx.fd.gz | | | | | 1 | |
| naalun450c.2.5um.fd.gz | | | | | 1 | |
| neodymium_oxide_compete.fd.gz | | | | | | |
| neodymium_oxide1.fd.gz | | | | | | |
| nitrate_niter_3.6um_curvc.fd.gz | | 1 | | | 1 | |
| nitrate_niter_3.6um.fd.gz | | 1 | | | 1 | |
| nitrate_niter.fd.gz | | 1 | | | 1 | |
| nitrate_potassium.fd.gz | | 1 | | | 1 | |
| nitrate_sodium.fd.gz | | 1 | | | 1 | |
| oh_1.378_phyllo-ksg-chrysotile.fd.gz | | | 1 | 1 | | |
| oh_1.381_phyllo-ksg-dickite.fd.gz | | | | 1 | 1 | |
| oh_1.383_amphibole-richterite.fd.gz | | | 1 | 1 | | 1 |
| oh_1.385_phyllo-ksg-nacrite.fd.gz | | | | 1 | 1 | |
| oh_1.388_phyllo-chlorite.fd.gz | | | 1 | 1 | | 1 |
| oh_1.390_phyllo-ksg-endellite.fd.gz | | | | 1 | 1 | |
| oh_1.392_amphibole-tremolite.fd.gz | | | 1 | | | |
| oh_1.392_phyllo-ksg-lizardite.fd.gz | | | | | | |
| oh_1.392_smectite-saponite.fd.gz | 1 | | 0 | 1 | 1 | |
| oh_1.393_phyllo-serpentine.fd.gz | | | | | | |
| oh_1.393_phyllo-talc.fd.gz | | | 1 | 1 | | |
| oh_1.394_phyllo-pyrophyllite.fd.gz | | | 1 (met) | 1 | | |
| oh_1.395_phyllo-ksg-antigorite.fd.gz | | | 1 (met) | | | |
| oh_1.396_amphibole-actinolite.fd.gz | | | 1 (met) | | | 1 |
| oh_1.396_amphibole-uralite.fd.gz | | | 1 (met) | | | 1 |
| oh_1.397_mica-phlogopite.fd.gz | | | 1 (met) | | | 1 |
| oh_1.398_amphibole-smaragdit.fd.gz | | | 1 (met) | | | 1 |
| oh_1.398_phyllo-clinochlore.fd.gz | | | 1 (met) | 1 | | |
| oh_1.398-phyllo-kaolinite-wxl.fd.gz | | | | | 1 | |
| oh_1.400_phyllo-chlorgrp-cookeite.fd.gz | | | 1 | | | |
| oh_1.401_mica-lepidolite.fd.gz | | | | 1 | | 1 |
| oh_1.406_silica-opal.fd.gz | 1 | | | | 1 | |
| oh_1.408_mica-paragonite.fd.gz | | | 1 (met) | | | |
| oh_1.409_mica-lepidolite.fd.gz | | | | 1 | | 1 |
| oh_1.413_phyllo-kaolinite-pxl.fd.gz | | | | | 1 | |
| oh_1.432_phyllo-vermiculite.fd.gz | | | | 1 | 1 | |
| ohb_1.385_phyllo-nacrite.fd.gz | | | | 1 | 1 | |
| ohb_1.398_phyllo-kaolinite-wxl.fd.gz | | | | | 1 | |
| ohb_1.400_phyllo-cookeite.fd.gz | | | | 1 | | |
| ohb_1.406_nesosil-topaz.fd.gz | | | 1 (met) | 1 | | 1 |
| ohb_1.406_tectosil-opal.fd.gz | 1 | | | | 1 | |
| ohb_1.408_mica-paragonite.fd.gz | | | 1 (met) | | | |
| ohb_1.409_phyllo-lepidolite.fd.gz | | | | 1 | | 1 |
| ohb_1.409_smectite-sauconite.fd.gz | | | | | 1 | |
| ohb_1.410_kaolgrp-halloysite.fd.gz | | | | 1 | 1 | |
| ohb_1.410_mica-margarite.fd.gz | | | 1 | 1 | | 1 |
| ohb_1.410_mica-muscovite.fd.gz | 1 | | 1 | 1 | | 1 |
| ohb_1.410_phyllo-chrysocolla.fd.gz | | | 1 | 1 | | |
| ohb_1.411_smectite-montmor-swy.fd.gz | 1 | | | 1 | 1 | |
| ohb_1.413_kaolgrp-kaolinite-pxl.fd.gz | 1 | | 1 | | 1 | |
| ohb_1.413_nesosil-hydrogross.fd.gz | | | 1 | 1 | | |
| ohb_1.414_smectite-hectorite.fd.gz | | | | 1 | | |
| ohb_1.416_mica-illite.fd.gz | 1 | | | 1 | 1 | |
| ohb_1.416_mica-roscoelite.fd.gz | 1 | | 1 | 1 | | |
| ohb_1.416_phyllo-sepiolite.fd.gz | 1 | 1 | | 1 | 1 | |
| ohb_1.416_smectite-montmor-saz.fd.gz | 1 | | | 1 | 1 | |
| ohb_1.417_phyllo-palygorsk.fd.gz | 1 | | | 1 | | |

**Table A1**
(Continued)

| Entry Name | Lacustrine/ Marine | Evaporitic/ Playa | Metamorphic | Hydrothermal | Pedogenic /Diagenic /Weathering (Include Secondary Coatings) | Igneous (Include Carbonatites) |
|---|---|---|---|---|---|---|
| ohb_1.418_mica_muscovite.fd.gz | 1 | | 1 | 1 | | 1 |
| ohb_1.418_zeolite_mordonite.fd.gz | 1 | | | 1 | | |
| ohb_1.419_zeolite-clinpt.fd.gz | | | | 1 | | 1 |
| ohb_1.419_zeolite-stilbite.fd.gz | 1 | | | 1 | | |
| ohb_1.422_zeolite-heuland.fd.gz | | | | 1 | | |
| ohb_1.423_scapolute-meionite.fd.gz | | | 1 | | | |
| ohb_1.424_smectite-nontronite.fd.gz | 1 | | | 1 | | |
| ohb_1.424_zeolite-analcime.fd.gz | | | | | | 1 |
| ohb_1.425_scapolite-mizzonite.fd.gz | | | 1 | | | |
| ohb_1.425_sulfate-alunite.fd.gz | | | 1 | 1 | | 1 |
| ohb_1.429_sodalite-lazurite.fd.gz | | | 1 | | | |
| ohb_1.431_cyclosil-elbaite.fd.gz | | | 1 | | | 1 |
| ohb_1.431_zeolite-laumontite.fd.gz | | | | 1 | | 1 |
| ohb_1.432_phyllo-vermiculite.fd.gz | | | | 1 | 1 | 1 |
| ohb_1.435_tourmaline.fd.gz | 1 | | 1 | | | 1 |
| ohb_1.436_sulfate-eugsterite.fd.gz | | | | | 1 | |
| ohb_1.438_sulfate-alunite-na.fd.gz | | | 1 | 1 | | 1 |
| ohb_1.440_zeolite-scolecite.fd.gz | | | | 1 | 1 | 1 |
| ohb_1.447_sulfate-gypsum.fd.gz | 1 | 1 | | 1 | | |
| ohb_1.449_sulfate-schwertm.fd.gz | | | | 1 | | |
| ohb_1.450_sulfate-copiapite.fd.gz | | | | 1 | 1 | |
| ohb_1.451_hydroxide-gibbsite.fd.gz | 1 | | | 1 | | |
| ohb_1.455_zeolite-natrolite.fd.gz | | | | 1 | | 1 |
| ohc_1.451_hydroxide-gibbsite.fd.gz | 1 | | | 1 | | |
| ohc_1.455_zeolite-natrolite.fd.gz | | | | 1 | | 1 |
| ohc_1.464_sulfate-bloedite.fd.gz | | 1 | | | | |
| ohc_1.469_sulfate-jarosite-k.fd.gz | | | | 1 | 1 | |
| ohc_1.471_nesisil-datolite.fd.gz | | | 1 | | | |
| ohc_1.471_sulfate-jarosite-k.fd.gz | | | | 1 | 1 | |
| ohc_1.478_sulfate-jarosite-na90c.fd.gz | | | | 1 | 1 | |
| ohc_1.479_sulfate-jarosite-na200c.fd.gz | | | | 1 | 1 | |
| ohc_1.480_phyllo-prehnite.fd.gz | | | 1 | | | |
| olivine_fo18_ki3377.fd.gz | | | | | 1 | |
| olivine_fo60_ki3189.fd.gz | | | | | 1 | |
| olivine_fo66_ki3054.fd.gz | | | | | 1 | |
| olivine_fo80_ki3377.fd.gz | | | | | 1 | |
| olivine_fo89_gds70.a.fd.gz | | | | | 1 | |
| olivine_fo91_gds71.b.fd.gz | | | | | 1 | |
| organic_dry_long_grass-thick.fd.gz | | | | | | |
| organic_drygrass+.17Na-mont.fd.gz | | | | | | |
| organic_tce+montswy.fd.gz | | | | | | |
| organic_toluene+montswy.fd.gz | | | | | | |
| organic_trace_3.42um_aliphatic1_curvc.fd.gz | | | | | | |
| organic_trace_aliphatic1.fd.gz | | | | | | |
| organic_trichlor+montswy.fd.gz | | | | | | |
| organic_unleaded.gas+montswy.fd.gz | | | | | | |
| organic_vegetation-dry-grass-golden.fd.gz | | | | | | |
| organic_vegetation-dry-grass-long.fd.gz | | | | | | |
| organic_vegetation-dry-wood.fd.gz | | | | | | |
| palygorskite.fd.gz | | | | 1 | | |
| perchlorate_mg.fd.gz | | 1 | | | | |
| perchlorate_na.fd.gz | | 1 | | | | |
| phlogopite.fd.gz | | | | | | |
| phyllosilicate.clintonite.fd.gz | | | 1 | 1 | 1 | 1 |
| polyhalite.fd.gz | | 1 | | | | |
| portlandite.fd.gz | | 1 | 1 | 1 | | |
| prehnite.fd.gz | | | 1 | 1 | | |
| prehnite+.50chlorite.fd.gz | | | 1 | 1 | | 1 |
| prehnite+.67chlorite.fd.gz | | | 1 | 1 | | |
| prehnite+.75chlorite.fd.gz | | | 1 | 1 | | |
| prehnite+muscovite.fd.gz | | | 1 | 1 | | 1 |

**Table A1**
(Continued)

| Entry Name | Lacustrine/ Marine | Evaporitic/ Playa | Metamorphic | Hydrothermal | Pedogenic /Diagenic /Weathering (Include Secondary Coatings) | Igneous (Include Carbonatites) |
|---|---|---|---|---|---|---|
| pyroph.5+alunit.5.fd.gz | | | 1 | 1 | | |
| pyroph.5+mont0.5.fd.gz | | | 1 | 1 | | |
| pyroph+musc.added.fd.gz | | | 1 | 1 | | |
| pyroph+tr.musc.fd.gz | | | 1 | 1 | | |
| pyrophyllite.fd.gz | | | 1 | 1 | | |
| pyroxene.augite.fd.gz | | | | | | 1 |
| pyroxene.bronzite.fd.gz | | | | | | 1 |
| pyroxene.enstatite.fd.gz | | | | | | 1 |
| pyroxene.hypersthene.fd.gz | | | | | | 1 |
| pyroxene.pigeonite.fd.gz | | | | | | 1 |
| richterite.fd.gz | | | 1 | 1 | | |
| rivadavite.fd.gz | | 1 | | 1 | | |
| rutile_hs126.3b.fd.gz | | | | | | 1 |
| saponite.or.talc.fd.gz | 1 | | | 1 | 1 | |
| sepiolite.fd.gz | | 1 | | | | |
| serpentine_chrysotile.coarse-fibrous.fd.gz | | 1 | | | | |
| serpentine_chrysotile.fine-fibrous.fd.gz | | | 1 | | | |
| serpentine_chrysotile.med-fine-fibrous.fd.gz | | 1 | | | | |
| serpentine_cronstedtite.fd.gz | | | 1 | | | |
| sioh_chalcedony.fd.gz | 1 | | 1 | 1 | 1 | |
| sioh_hydrated_basaltic_glass.fd.gz | | | | | | 1 |
| smectite_ammonillsmec.fd.gz | | | | 1 | 1 | |
| smectite_beidellite_gds123.fd.gz | | | | 1 | 1 | |
| smectite_beidellite_gds124.fd.gz | | | | 1 | 1 | |
| smectite_montmorillonite_ca_swelling.fd.gz | | | 1 | 1 | | |
| smectite_montmorillonite_fe_swelling.fd.gz | | | 1 | 1 | | |
| smectite_montmorillonite_na_highswelling.fd.gz | | | 1 | 1 | | |
| smectite_nontronite_swelling.fd.gz | | | | 1 | 1 | |
| sphalerite_s26-341_1.5um.fd.gz | | | | 1 | | 1 |
| sulfate_alun35K65Na.low.fd.gz | | | | 1 | | |
| sulfate_alun66K34Na.low.fd.gz | | | | 1 | | |
| sulfate_alun73K27Na.low.fd.gz | | | | 1 | | |
| sulfate_alunite_int-comp.all.fd.gz | | | | 1 | | |
| sulfate_alunite_k.all.fd.gz | | | | 1 | | |
| sulfate_alunite_na.all.fd.gz | | | | 1 | | |
| sulfate_alunNa03.fd.gz | | | | 1 | | |
| sulfate_alunNa56450c.fd.gz | | | | 1 | | |
| sulfate_alunNa78.450c.fd.gz | | | | 1 | | |
| sulfate_ammonalunite.fd.gz | | | | | | |
| sulfate_ammonjarosite.fd.gz | | | | 1 | 1 | |
| sulfate_gypsum.fd.gz | | 1 | | 1 | 1 | |
| sulfate_jarosite-K.fd.gz | | | | 1 | 1 | |
| sulfate_jarosite-lowT.fd.gz | | | | 1 | 1 | |
| sulfate_jarosite-Na.fd.gz | | | | 1 | 1 | |
| sulfate_kalun150c.fd.gz | | 1 | | | | |
| sulfate_kalun250c.fd.gz | | 1 | | | | |
| sulfate_kalun450c.fd.gz | | 1 | | | | |
| sulfate_kieserite.fd.gz | 1 | | | | 1 | |
| sulfate_lazurite.fd.gz | | | 1 | | | |
| sulfate_mascagnite.fd.gz | | | | 1 | | |
| sulfate_mirabilite-wet_soil.fd.gz | | 1 | | | | |
| sulfate_na40alun400c.fd.gz | | | | 1 | | |
| sulfate_na63alun300c.fd.gz | | | | 1 | | |
| sulfate_na82alun100c.fd.gz | | | | 1 | | |
| sulfate_naalun150c.fd.gz | | | | 1 | | |
| sulfate_naalun300c.fd.gz | | | | 1 | | |
| sulfate_naalun450c.fd.gz | | | | 1 | | |
| sulfate_syngenite.fd.gz | 1 | 1 | 1 | | 1 | |
| sulfate_szomolnokite_heated.fd.gz | 1 | | | | 1 | |
| sulfate_szomolnokite.fd.gz | 1 | | | | 1 | |
| sulfate-mix_gyp+jar+musc.amix.fd.gz | | 1 | | 1 | | |

**Table A1**
(Continued)

| Entry Name | Lacustrine/ Marine | Evaporitic/ Playa | Metamorphic | Hydrothermal | Pedogenic /Diagenic /Weathering (Include Secondary Coatings) | Igneous (Include Carbonatites) |
|---|---|---|---|---|---|---|
| sulfate-mix_gyp+jar+musc+dick.amix.fd.gz | 1 | | 1 | | | |
| sulfate-mix_gypsum.trace.dust+debris-WTC01-2.fd.gz | 1 | | 1 | | | |
| sulfate-mix_gypsum.trace.dust+debris-WTC01-28.fd.gz | 1 | | 1 | | | |
| sulfate-mix_gypsum+jar+illite.intmix.fd.gz | 1 | 1 | | | | |
| sulfate+kaolingrp_natroalun+dickite.fd.gz | | | 1 | 1 | | |
| sulfide_cinnabar.fd.gz | | | | 1 | | |
| sulfide_copper_chalcopyrite.fd.gz | | | | 1 | | 1 |
| sulfide_pyrite.fd.gz | | | 1 | | 1 | 1 |
| sulfur.fd.gz | | | 1 | | | 1 |
| talc.all.fd.gz | | | 1 | | | |
| talc.crsgrnd.fd.gz | | | 1 | | | |
| talc.fngrnd.fd.gz | | | 1 | | | |
| talc+calcite.parkcity.fd.gz | | | 1 | | | |
| talc+carbonate.parkcity.fd.gz | | | 1 | | | |
| topaz.fd.gz | | | | | | 1 |
| tremolite.or.talc.fd.gz | | | 1 | | | |
| ulexite.fd.gz | | 1 | | | | |
| veg0.9um.band.fd.gz | | | | | | |
| veg1.2um.band.fd.gz | | | | | | |
| veg1.4um.band.fd.gz | | | | | | |
| vegetation.dry_nonphotosyn.fd.gz | | | | | | |
| vegetation.dry+green.fd.gz | | | | | | |
| vegetation.map.fd.gz | | | | | | |
| vegetation.weak.map.fd.gz | | | | | | |
| vegetation1.fd.gz | | | | | | |
| water_1.896_beryl.fd.gz | | | | | | 1 |
| water_1.902_silica-opal.fd.gz | 1 | | | | | 1 |
| water_1.903_smectite-saponite.fd.gz | | | | 1 | 1 | |
| water_1.906_montmor-na.fd.gz | 1 | | | | | |
| water_1.907_smectite-nontronite.fd.gz | | | | 1 | 1 | 1 |
| water_1.908_phyllo-illite.fd.gz | | | | | 1 | |
| water_1.908_smectite-beidell.fd.gz | 1 | | | | 1 | |
| water_1.909_mont-saz.fd.gz | | | | | 1 | |
| water_1.910_halloysite.fd.gz | | | | 1 | 1 | |
| water_1.910_stonwplaya.fd.gz | | 1 | | | | |
| water_1.910_zeolite-clinopt.fd.gz | | | | | | 1 |
| water_1.910_zeolite-mordonite.fd.gz | | | | | 1 | 1 |
| water_1.912_zeolite-analcime.fd.gz | | | | | 1 | 1 |
| water_1.916_nesosil-sillim.fd.gz | | | 1 | | 1 | |
| water_1.917_zeolite-heuland.fd.gz | | | | | 1 | 1 |
| water_1.918_perchlorate-mg.fd.gz | | | | | 1 | |
| water_1.920_sulfate-bassanite.fd.gz | | 1 | | | 1 | |
| water_1.923_chert.fd.gz | | | | | 1 | |
| water_1.924_perchlorate-na.fd.gz | | | | | 1 | |
| water_1.929_sulfate-epsomite.fd.gz | | 1 | | | | |
| water_1.931_narrow-cheatgrass.fd.gz | | | | | | |
| water_1.932_sulfate-eusgterite.fd.gz | | 1 | | | | |
| water_1.940_zeolite-natrolite.fd.gz | | | | 1 | | 1 |
| water_1.941_zeolite-natrolite.fd.gz | | | | 1 | 1 | |
| water_1.941_zeolite-scolecite.fd.gz | | | | | 1 | |
| water_1.942_sulfate-schwert.fd.gz | | | | | 1 | |
| water_1.943_sulfate-gypsum.fd.gz | 1 | 1 | | | | |
| water_1.944_sulfate-polyhalite.fd.gz | 1 | 1 | | | | |
| water_1.946_sulfate-copiapite.fd.gz | | | | | 1 | |
| water_1.951_sulfate-bloedite.fd.gz | 1 | 1 | | | | |
| water_1.960_sulfate-butler.fd.gz | | | | | 1 | |
| water_1.964_sulfate-feso4.fd.gz | | 1 | | | 1 | |
| water_1.971_sulfate-kainite.fd.gz | | 1 | | | | |
| water_1.980_salt-carnallite.fd.gz | 1 | 1 | | | | |

**Table A1**
(Continued)

| Entry Name | Lacustrine/ Marine | Evaporitic/ Playa | Metamorphic | Hydrothermal | Pedogenic /Diagenic /Weathering (Include Secondary Coatings) | Igneous (Include Carbonatites) |
|---|---|---|---|---|---|---|
| water_1.981_sulfate-coquimb.fd.gz | | | | | 1 | |
| water_1.991_sulfate-syngite.fd.gz | 1 | 1 | | | | |
| water_2.060_sulfate_szomoln.fd.gz | | | | | 1 | |
| water_2.073_sulfate-kieserite.fd.gz | 1 | 1 | | | | |
| water_2.093_sulfate_szomoln.fd.gz | | | | | 1 | |
| water_2.122_nh4-buddingt.fd.gz | | | | 1 | | |
| water_2.130_sulfate_kieserite.fd.gz | 1 | 1 | | | | |
| water_2.136_nh4-mascagnite.fd.gz | | | | | | 1 |
| water_broad_1.927_veg.fd.gz | | | | | | |
| water.high.chlorophyll.fd.gz | | | | | | |
| water.red.algae.fd.gz | | | | | | |
| water+mont0.5gpl.fd.gz | | | | | | |
| water+mont1.67gpl.fd.gz | | | | | | |
| water+mont16.5gpl.fd.gz | | | | | | |
| water+mont5.01gpl.fd.gz | | | | | | |
| white.crust.starkeyite.fd.gz | | 1 | | | | |
| zeolite_analcime.fd.gz | | | 1 | | | |
| zeolite_natrolite.fd.gz | | | 1 | | | |
| zoisite.fd.gz | | | 1 | | | |
| zunyite.fd.gz | | | 1 | | | |

## Appendix B

### *B.1. Year 2 Geologic Origin Table B1/B2*

Tables B1 and B2 contain the geologic origin lookup table used in the second field expedition to the Yellow Cat Flat field site. Table B1 relates individual entries from the USGS spectral library to minerals.

**Table B1**
Geologic Origin Lookup Table Part 1—Year 2—Site 2

| Flag/Ignore: #comment<br>0 = ignore 1 = use-with-rover | Group (In Expert System) | Mineral(s) | Entry Name |
|---|---|---|---|
| 1 | 2 | actinolite | actinolite.fd.gz |
| 0 | 6 | adularia | adularia_2.5um.fd.gz |
| 1 | 2 | hydroth_pedogen_alunite; kaolinite; muscovite | alunite.33+kaol.33+musc.33.fd.gz |
| 1 | 2 | hydroth_pedogen_alunite; kaolinite | alunite.5+kaol.5.fd.gz |
| 1 | 2 | hydroth_pedogen_alunite; muscovite | alunite.5+musc.5.fd.gz |
| 1 | 2 | hydroth_pedogen_alunite; kaolinite; muscovite | alunite+kaolinite.muscovite.added.fd.gz |
| 1 | 2 | hydroth_pedogen_alunite; muscovite; pyrophyllite | alunite+musc+pyroph.fd.gz |
| 1 | 2 | hydroth_pedogen_alunite; pyrophyllite | alunite+pyroph.added.fd.gz |
| 1 | 2 | hydroth_pedogen_alunite; pyrophyllite | alunite+pyrophyl.fd.gz |
| 1 | 2 | amphibole | amphibole.fd.gz |
| 0 | 6 | analcime | analcime.2.5um.fd.gz |
| 1 | 4 | anorthite | anorthite_hs201.3b.fd.gz |
| 1 | 2 | colemanite | borate_colemanite.fd.gz |
| 1 | 2 | pinnoite | borate_pinnoite.fd.gz |
| 1 | 4 | bytownite | bytownite_hs106.3b.fd.gz |
| 1 | 2 | calcite; dolomite; montmorillonite | calcite.25+dolom.25+Na-mont.5.fd.gz |
| 1 | 2 | calcite; montmorillonite | calcite+0.2Na-mont.fd.gz |
| 1 | 2 | calcite; montmorillonite | calcite+0.5Ca-mont.fd.gz |
| 1 | 2 | arqgonite | carbonate_aragonite.fd.gz |
| 1 | 2 | azurite | carbonate_azurite.fd.gz |
| 0 | 10 | calcite | carbonate_calcite_3.5um_curvc.fd.gz |
| 0 | 11 | calcite | carbonate_calcite_3.5um.fd.gz |
| 1 | 2 | calcite; dolomite; montmorillonite | carbonate_calcite.25+dolom.25+Ca-mont.5.fd.gz |
| 1 | 2 | calcite | carbonate_calcite.fd.gz |
| 1 | 2 | calcite; montmorillonite | carbonate_calcite+0.2Ca-mont.fd.gz |
| 1 | 2 | calcite; kaolinite | carbonate_calcite+0.2kaolwxl.fd.gz |
| 1 | 2 | calcite; muscovite | carbonate_calcite+0.3muscovite.fd.gz |
| 1 | 2 | calcite; dolomite | carbonate_calcite+dolomite.5.fd.gz |
| 1 | 2 | calcite; kaolinite | carbonate_calcite0.7+kaol0.3.fd.gz |
| 1 | 2 | dolomite; montmorillonite | carbonate_dolo+.5ca-mont.fd.gz |
| 0 | 10 | dolomite | carbonate_dolomite_3.5um_curvc.fd.gz |
| 0 | 11 | dolomite | carbonate_dolomite_3.5um.fd.gz |
| 1 | 2 | dolomite; montmorillonite | carbonate_dolomite.5+Na-mont.5.fd.gz |
| 1 | 2 | dolomite | carbonate_dolomite.fd.gz |
| 1 | 2 | magnesite | carbonate_magnesite.fd.gz |
| 0 | 10 | magnesite; hydromagnesite | carbonate_magnesite+hydromagnesite_curvc.fd.gz |
| 0 | 11 | magnesite; hydromagnesite | carbonate_magnesite+hydromagnesite.fd.gz |
| 1 | 2 | malachite | carbonate_malachite.fd.gz |
| 1 | 2 | rhodochrosite | carbonate_rhodochrosite.fd.gz |
| 1 | 2 | siderite | carbonate_siderite.fd.gz |
| 1 | 2 | calcite; montmorillonite | carbonate_smectite_calcite.33+Ca-mont.67.fd.gz |
| 1 | 2 | strontinite | carbonate_strontianite.fd.gz |
| 0 | 10 | carbonate | carbonate_trace_3.5um_curvc.fd.gz |
| 0 | 11 | carbonate | carbonate_trace_3.5um.fd.gz |
| 1 | 2 | witherite | carbonate_witherite.fd.gz |
| 1 | 2 | canallite | chloride_carnallite.fd.gz |
| 1 | 2 | clinochlore | chlorite_clinochlore.fd.gz |
| 1 | 2 | clinochlore | chlorite_clinochlore.fe.gds157.fd.gz |
| 1 | 2 | clinochlore | chlorite_clinochlore.fe.sc-cca-1.fd.gz |
| 1 | 2 | clinochlore | chlorite_clinochlore.nmnh83369.fd.gz |
| 1 | 2 | cookeite | chlorite_cookeite-car-1.a.fd.gz |
| 1 | 2 | cookeite | chlorite_cookeite-car-1.c.fd.gz |
| 1 | 2 | thuringite | chlorite_thuringite.fd.gz |
| 1 | 2 | chlorite | chlorite-scarn.fd.gz |
| 1 | 2 | chlorite | chlorite.fd.gz |
| 1 | 2 | chrysocolla | chrysocolla.fd.gz |
| 1 | 2 | chrysotile | serpentine_chrysotile.coarse-fibrous.fd |
| 1 | 2 | chrysotile | serpentine_chrysotile.fine-fibrous.fd |
| 1 | 2 | chrysotile; gypsum | chrysotile.gypsum.wtc01-8.fd.gz |

**Table B1**
(Continued)

| Flag/Ignore: #comment<br>0 = ignore 1 = use-with-rover | Group (In Expert System) | Mineral(s) | Entry Name |
|---|---|---|---|
| 1 | 2 | chrysotile | serpentine_chrysotile.med-fine-fibrous.fd |
| 1 | 2 | hectorite | clay_hectorite.fd.gz |
| 1 | 2 | clintonite | clintonite.fd |
| 1 | 1 | azurite | copper_carbonate_azurite.fd.gz |
| 1 | 1 | malachite | copper_carbonate_malachite.fd.gz |
| 1 | 1 | chrysocolla | copper_chrysocolla.fd.gz |
| 1 | 1 | cuprite | copper_oxide_cuprite.fd.gz |
| 0 | 1 | ? | copper_precipitate_greenslime.fd.gz |
| 0 | 1 | ? | copper_sulfate_bluefflor.fd.gz |
| 1 | 2 | cyanide | cyanide-CdK.fd.gz |
| 1 | 2 | cyanide | cyanide-KFe.fd.gz |
| 1 | 2 | cyanide | cyanide-NiK.fd.gz |
| 1 | 2 | cyanide | cyanide-trihydrate.fd.gz |
| 1 | 2 | cyanide | cyanide-ZnK.fd.gz |
| 1 | 2 | datolite | datolite.fd.gz |
| 1 | 5 | diaspore | diaspore.fd.gz |
| 1 | 2 | dickite; muscovite; gypsum; jarosite | dick+musc+gyp+jar.amix.fd.gz |
| 1 | 2 | elbaite | elbaite.fd.gz |
| 1 | 1 | epidote | epidote.fd.gz |
| 1 | 2 | epidote | epidote.fd.gz |
| 0 | 6 | eugsterite | eugsterite.2.5um.water.fd.gz |
| 1 | 1 | chlorite; muscovite | fe2+_chlor+muscphy.fd.gz |
| 1 | 1 | clinochlore | fe2+_chlorite.clinochlor.fd.gz |
| 1 | 1 | clinochlore | fe2+_chlorite.Felow.clinochlor.fd.gz |
| 1 | 1 | thuringite | fe2+_chlorite.thuringite.fd.gz |
| 1 | 1 | chromite | fe2+_chromite.fd.gz |
| 1 | 1 | albite | fe2+_feldspar_albite.fd.gz |
| 1 | 1 | microcline | fe2+_feldspar_microcline.fd.gz |
| 1 | 1 | orthoclase | fe2+_feldspar_orthoclase.fd.gz |
| 1 | 1 | bytownite | fe2+_feldspar.bytownite.fd.gz |
| 1 | 1 | goethite; muscovite | fe2+_goeth+musc.fd.gz |
| 1 | 1 | olivine | fe2+_olivine-fine-gr.fd.gz |
| 1 | 1 | olivine | fe2+_olivine-lrg-gr.fd.gz |
| 1 | 1 | augite | fe2+_pyroxene_augite.fd.gz |
| 1 | 1 | pigeonite | fe2+_pyroxene_clino_pigeonite.fd.gz |
| 1 | 1 | enstatite | fe2+_pyroxene_enstatite.fd.gz |
| 1 | 1 | hedenbergite | fe2+_pyroxene_hedenbergite.fd.gz |
| 1 | 1 | bronzite | fe2+_pyroxene.bronzite.fd.gz |
| 1 | 1 | diopside | fe2+_pyroxene.diopside.fd.gz |
| 1 | 1 | hypersthene | fe2+_pyroxene.hypersthene.fd.gz |
| 1 | 4 | wollastonite | fe2+_wollastonite_hs348.3b.fd.gz |
| 1 | 1 | chlorite; goethitte; propylzone | fe2+fe3+_chlor+goeth.propylzone.fd.gz |
| 1 | 1 | hematite_smallgrain | fe2+fe3+_hematite_weathering.fd.gz |
| 0 | 1 | ? | fe2+fe3+_water_RTsludge.fd.gz |
| 1 | 1 | hematite | fe2+fe3+mix_with_hematite_br5b.fd.gz |
| 0 | 1 | almandine | fe2+generic_almandine.fd.gz |
| 0 | 1 | riebeckite | fe2+generic_amphibole_riebeckite.fd.gz |
| 0 | 1 | axinite | fe2+generic_axinite.fd.gz |
| 0 | 1 | basalt | fe2+generic_basalt_br46b.fd.gz |
| 0 | 1 | ? | fe2+generic_br33a_bioqtzmonz_epidote.fd.gz |
| 0 | 1 | actinolite | fe2+generic_brd.br22c_actinolite.fd.gz |
| 0 | 1 | chlorite | fe2+generic_brd.br36a_chlorite.fd.gz |
| 0 | 1 | actinolite | fe2+generic_brd.br5a_actinolite.fd.gz |
| 0 | 1 | ? | fe2+generic_broad_br60b.fd.gz |
| 0 | 1 | siderite | fe2+generic_carbonate_siderite1.fd.gz |
| 0 | 1 | jadeite | fe2+generic_med.jadeite.fd.gz |
| 0 | 1 | actinolite | fe2+generic_nrw.actinolite.fd.gz |
| 0 | 1 | cummingtonite | fe2+generic_nrw.cummingtonite.fd.gz |
| 0 | 1 | actinolite | fe2+generic_nrw.hs-actinolite.fd.gz |
| 0 | 1 | staurolite | fe2+generic_staurolite.fd.gz |
| 0 | 1 | butlerite | fe2+generic_sulfate_butlerite.fd.gz |
| 0 | 1 | ? | fe2+generic_vbroad_br20.fd.gz |

**Table B1**
(Continued)

| Flag/Ignore: #comment<br>0 = ignore 1 = use-with-rover | Group (In Expert System) | Mineral(s) | Entry Name |
|---|---|---|---|
| 0 | 1 | ? | fe2+generic.all.fd.gz |
| 1 | 1 | ferrihydrite | fe3+_ferrihydrite.fd.gz |
| 1 | 1 | goethite; jarosite | fe3+_goeth+jarosite.fd.gz |
| 1 | 1 | goethite | fe3+_goethite.coarsegr.ALL.fd.gz |
| 1 | 1 | goethite | fe3+_goethite.coarsegr.fd.gz |
| 1 | 1 | goethite | fe3+_goethite.fingr.fd.gz |
| 1 | 1 | goethite; lepidocrosite | fe3+_goethite.lepidocrosite.fd.gz |
| 1 | 1 | goethite | fe3+_goethite.medcoarsegr.mpc.trjar.fd.gz |
| 1 | 1 | goethite | fe3+_goethite.medgr.fd.gz |
| 1 | 1 | goethite | fe3+_goethite.medgr.ws222.fd.gz |
| 1 | 1 | goethite | fe3+_goethite.thincoat.fd.gz |
| 1 | 1 | goethite; quartz | fe3+_goethite+qtz.medgr.gds240.fd.gz |
| 1 | 1 | hematite; hematite_smallgrain | fe3+_hematite.all.fd.gz |
| 1 | 1 | hematite_smallgrain | fe3+_hematite.fine.gr.all.fd.gz |
| 1 | 1 | hematite_smallgrain | fe3+_hematite.fine.gr.fe2602.fd.gz |
| 1 | 1 | hematite_smallgrain | fe3+_hematite.fine.gr.gds76.fd.gz |
| 1 | 1 | hematite_smallgrain | fe3+_hematite.fine.gr.ws161.fd.gz |
| 1 | 1 | hematite | fe3+_hematite.lg.gr.all.fd.gz |
| 1 | 1 | hematite | fe3+_hematite.lg.gr.br25a.fd.gz |
| 1 | 1 | hematite | fe3+_hematite.lg.gr.br34c.fd.gz |
| 1 | 1 | hematite | fe3+_hematite.med.gr.all.fd.gz |
| 1 | 1 | hematite | fe3+_hematite.med.gr.br25b.fd.gz |
| 1 | 1 | hematite | fe3+_hematite.med.gr.gds27.fd.gz |
| 1 | 1 | hematite_smallgrain | fe3+_hematite.nano.BR34b2.fd.gz |
| 1 | 1 | hematite_smallgrain | fe3+_hematite.thincoat.fd.gz |
| 1 | 1 | maghemite | fe3+_maghemite.fd.gz |
| 1 | 1 | nontronite | fe3+_smectite_nontronite.fd.gz |
| 1 | 1 | jarosite | fe3+_sulfate_jarosite_br34a2.fd.gz |
| 1 | 1 | jarosite | fe3+_sulfate_kjarosite200.fd.gz |
| 1 | 1 | schwertmannite | fe3+_sulfate_schwertmannite.fd.gz |
| 1 | 1 | pitchlimonite | fe3+copper-hydroxide_pitchlimonite.fd.gz |
| 1 | 1 | copiapite | fe3+fe2+_sulfate_copiapite.fd.gz |
| 1 | 1 | coquimbite | fe3+fe2+_sulfate_coquimbite.fd.gz |
| 1 | 1 | Fe3+ | fe3+mix_AMD.assemb1.fd.gz |
| 1 | 1 | Fe3+ | fe3+mix_AMD.assemb1+2.fd.gz |
| 1 | 1 | Fe3+ | fe3+mix_AMD.assemb2.fd.gz |
| 1 | 1 | Fe3+; manganese | fe3+mn_desert.varnish1.fd.gz |
| 1 | 1 | Fe3+; manganese | fe3+mn_desert.varnish2.fd.gz |
| 1 | 2 | buddingtonite; montmorillonite | feldspar_buddington.namont.fd.gz |
| 1 | 2 | buddingtonite; montmorillonite | feldspar_buddington.namont2.fd.gz |
| 1 | 2 | buddingtonite; montmorillonite | feldspar_buddingtonite_ammonium.fd.gz |
| 0 | 7 | goethite | goethite_3.17um.fd.gz |
| 0 | 7 | grossular | grossular_3.17um.fd.gz |
| 0 | 19 | snow | h20_ice_2.02um-77k-a.fd.gz |
| 1 | 2 | hornblende | hornblende.fd.gz |
| 1 | 2 | howlite | howlite.fd.gz |
| 0 | 10 | peroxide | hydrogen_peroxide.3.52um_curvc.fd.gz |
| 1 | 2 | grossular | hydrogrossular.fd.gz |
| 1 | 2 | brucite | hydroxide_brucite.fd.gz |
| 1 | 2 | diaspore | hydroxide_diaspore.fd.gz |
| 1 | 2 | gibbsite | hydroxide_gibbsite.fd.gz |
| 1 | 1 | pectolite | inosilicate_pectolite.fd.gz |
| 1 | 7 | jarosite | jarosite_3.18um.fd.gz |
| 1 | 2 | hydroth_alunite; kaolinite | Kalun+kaol.intmx.fd.gz |
| 1 | 2 | hydroth_pedogen_alunite; kaolinite | kaol.75+alun.25.fd.gz |
| 1 | 2 | pyrophyllite; kaolinite | kaol.75+pyroph.25.fd.gz |
| 1 | 2 | dickite | kaolgrp_dickite.fd.gz |
| 1 | 2 | halloysite | kaolgrp_halloysite.fd.gz |
| 1 | 2 | kaolinite | kaolgrp_kaolinite_pxl.fd.gz |
| 1 | 2 | kaolinite | kaolgrp_kaolinite_wxl.fd.gz |
| 1 | 2 | kaolinite; smectite | kaolin.3+smect.7.fd.gz |
| 1 | 2 | kaolinite; muscovite | kaolin.5+muscov.medAl.fd.gz |

**Table B1**
(Continued)

| Flag/Ignore: #comment<br>0 = ignore 1 = use-with-rover | Group (In Expert System) | Mineral(s) | Entry Name |
|---|---|---|---|
| 1 | 2 | kaolinite; muscovite | kaolin.5+muscov.medhighAl.fd.gz |
| 1 | 2 | kaolinite; smectite | kaolin.5+smect.5.fd.gz |
| 1 | 2 | kaolinite; muscovite | kaolin+musc.intimat.fd.gz |
| 1 | 2 | kaolinite; smectite | kaolinite.3+.5+smectite.5+.7.added.fd.gz |
| 1 | 2 | kaolinite; muscovite | kaolinite+muscovite.added.fd.gz |
| 1 | 4 | magnetite | magnetite_hs195.3b.or.olivine.fd.gz |
| 1 | 1 | magnetite | magnetite.fd.gz |
| 1 | 2 | biotite | micagrp_biotite.fd.gz |
| 1 | 2 | illite | micagrp_illite.fd.gz |
| 1 | 2 | illite | micagrp_illite.gds4.fd.gz |
| 1 | 2 | illite; roscoelite | micagrp_illite.roscoelite.fd.gz |
| 1 | 2 | lepidolite | micagrp_lepidolite.fd.gz |
| 1 | 2 | margarite | micagrp_margarite.fd.gz |
| 1 | 2 | muscovite | micagrp_muscovite-low-Al.fd.gz |
| 1 | 2 | muscovite | micagrp_muscovite-med-Al.fd.gz |
| 1 | 2 | muscovite | micagrp_muscovite-medhigh-Al.fd.gz |
| 1 | 2 | muscovite | micagrp_muscoviteFerich.fd.gz |
| 1 | 2 | paragonite | micagrp_paragonite.fd.gz |
| 1 | 4 | microcline | microcline_hs103.3b.fd.gz |
| 1 | 1 | pyrolusite | mn_oxide_pyrolusite.fd.gz |
| 1 | 1 | manganese | Mn-Coating.fd.gz |
| 0 | 1 | rhodonite | mn2+_rhodonite.fd.gz |
| 1 | 2 | muscovite; gypsum; jarosite; dickite | musc+gyp+jar+dick.amix.fd.gz |
| 1 | 2 | muscovite; jarosite | musc+jarosite.intimat.fd.gz |
| 1 | 2 | muscovite; pyrophyllite | musc+pyroph.fd.gz |
| 1 | 2 | muscovite; chlorite | muscovite+chlorite.fd.gz |
| 1 | 2 | hydroth_pedogen_alunite; kaolinite | Na-alun+kaol.intmx.fd.gz |
| 0 | 6 | hydroth_alunite | naalun450c.2.5um.fd.gz |
| 0 | 20 | neodymium_oxide | neodymium_oxide_compete.fd.gz |
| 0 | 21 | neodymium_oxide | neodymium_oxide1.fd.gz |
| 0 | 10 | niter | nitrate_niter_3.6um_curvc.fd.gz |
| 0 | 11 | niter | nitrate_niter_3.6um.fd.gz |
| 1 | 2 | niter | nitrate_niter.fd.gz |
| 1 | 2 | nitrate | nitrate_potassium.fd.gz |
| 1 | 2 | nitrate | nitrate_sodium.fd.gz |
| 0 | 13 | chrysotile | oh_1.378_phyllo-ksg-chrysotile.fd.gz |
| 0 | 13 | dickite | oh_1.381_phyllo-ksg-dickite.fd.gz |
| 0 | 13 | richterite | oh_1.383_amphibole-richterite.fd.gz |
| 0 | 13 | nacrite | oh_1.385_phyllo-ksg-nacrite.fd.gz |
| 0 | 13 | chlorite | oh_1.388_phyllo-chlorite.fd.gz |
| 0 | 13 | endellite | oh_1.390_phyllo-ksg-endellite.fd.gz |
| 0 | 13 | tremolite | oh_1.392_amphibole-tremolite.fd.gz |
| 0 | 13 | lizardite | oh_1.392_phyllo-ksg-lizardite.fd.gz |
| 0 | 13 | saponite | oh_1.392_smectite-saponite.fd.gz |
| 0 | 13 | serpentine | oh_1.393_phyllo-serpentine.fd.gz |
| 0 | 13 | talc | oh_1.393_phyllo-talc.fd.gz |
| 0 | 13 | pyrophyllite; kaolinite | oh_1.394_phyllo-pyrophyllite.fd.gz |
| 0 | 13 | antigorite | oh_1.395_phyllo-ksg-antigorite.fd.gz |
| 0 | 13 | actinolite | oh_1.396_amphibole-actinolite.fd.gz |
| 0 | 13 | uralite | oh_1.396_amphibole-uralite.fd.gz |
| 0 | 13 | phlogopite | oh_1.397_mica-phlogopite.fd.gz |
| 0 | 13 | smaragdite | oh_1.398_amphibole-smaragdit.fd.gz |
| 0 | 13 | clinochlore | oh_1.398_phyllo-clinochlore.fd.gz |
| 0 | 13 | | oh_1.398-phyllo-kaolinite-wxl.fd.gz |
| 0 | 13 | | oh_1.400_phyllo-chlorgrp-cookeite.fd.gz |
| 0 | 13 | | oh_1.401_mica-lepidolite.fd.gz |
| 0 | 13 | | oh_1.406_silica-opal.fd.gz |
| 0 | 13 | | oh_1.408_mica-paragonite.fd.gz |
| 0 | 13 | | oh_1.409_mica-lepidolite.fd.gz |
| 0 | 13 | | oh_1.413_phyllo-kaolinite-pxl.fd.gz |
| 0 | 13 | | oh_1.432_phyllo-vermiculite.fd.gz |
| 0 | 14 | | ohb_1.385_phyllo-nacrite.fd.gz |

**Table B1**
(Continued)

| Flag/Ignore: #comment<br>0 = ignore 1 = use-with-rover | Group (In Expert System) | Mineral(s) | Entry Name |
|---|---|---|---|
| 0 | 14 | | ohb_1.398_phyllo-kaolinite-wxl.fd.gz |
| 0 | 14 | | ohb_1.400_phyllo-cookeite.fd.gz |
| 0 | 14 | | ohb_1.406_nesosil-topaz.fd.gz |
| 0 | 14 | | ohb_1.406_tectosil-opal.fd.gz |
| 0 | 14 | | ohb_1.408_mica-paragonite.fd.gz |
| 0 | 14 | | ohb_1.409_phyllo-lepidolite.fd.gz |
| 0 | 14 | | ohb_1.409_smectite-sauconite.fd.gz |
| 0 | 14 | | ohb_1.410_kaolgrp-halloysite.fd.gz |
| 0 | 14 | | ohb_1.410_mica-margarite.fd.gz |
| 0 | 14 | | ohb_1.410_mica-muscovite.fd.gz |
| 0 | 14 | | ohb_1.410_phyllo-chrysocolla.fd.gz |
| 0 | 14 | | ohb_1.411_smectite-montmor-swy.fd.gz |
| 0 | 14 | | ohb_1.413_kaolgrp-kaolinite-pxl.fd.gz |
| 0 | 14 | | ohb_1.413_nesosil-hydrogross.fd.gz |
| 0 | 14 | | ohb_1.414_smectite-hectorite.fd.gz |
| 0 | 14 | | ohb_1.416_mica-illite.fd.gz |
| 0 | 14 | | ohb_1.416_mica-roscoelite.fd.gz |
| 0 | 14 | | ohb_1.416_phyllo-sepiolite.fd.gz |
| 0 | 14 | | ohb_1.416_smectite-montmor-saz.fd.gz |
| 0 | 14 | | ohb_1.417_phyllo-palygorsk.fd.gz |
| 0 | 14 | | ohb_1.418_mica_muscovite.fd.gz |
| 0 | 14 | | ohb_1.418_zeolite_mordonite.fd.gz |
| 0 | 14 | | ohb_1.419_zeolite-clinpt.fd.gz |
| 0 | 14 | | ohb_1.419_zeolite-stilbite.fd.gz |
| 0 | 14 | | ohb_1.422_zeolite-heuland.fd.gz |
| 0 | 14 | | ohb_1.423_scapolute-meionite.fd.gz |
| 0 | 14 | | ohb_1.424_smectite-nontronite.fd.gz |
| 0 | 14 | | ohb_1.424_zeolite-analcime.fd.gz |
| 0 | 14 | | ohb_1.425_scapolite-mizzonite.fd.gz |
| 0 | 14 | | ohb_1.425_sulfate-alunite.fd.gz |
| 0 | 14 | | ohb_1.429_sodalite-lazurite.fd.gz |
| 0 | 14 | | ohb_1.431_cyclosil-elbaite.fd.gz |
| 0 | 14 | | ohb_1.431_zeolite-laumontite.fd.gz |
| 0 | 14 | | ohb_1.432_phyllo-vermiculite.fd.gz |
| 0 | 14 | | ohb_1.435_tourmaline.fd.gz |
| 0 | 14 | | ohb_1.436_sulfate-eugsterite.fd.gz |
| 0 | 14 | | ohb_1.438_sulfate-alunite-na.fd.gz |
| 0 | 14 | | ohb_1.440_zeolite-scolecite.fd.gz |
| 0 | 14 | | ohb_1.447_sulfate-gypsum.fd.gz |
| 0 | 14 | | ohb_1.449_sulfate-schwertm.fd.gz |
| 0 | 14 | | ohb_1.450_sulfate-copiapite.fd.gz |
| 0 | 14 | | ohb_1.451_hydroxide-gibbsite.fd.gz |
| 0 | 14 | | ohb_1.455_zeolite-natrolite.fd.gz |
| 0 | 15 | | ohc_1.451_hydroxide-gibbsite.fd.gz |
| 0 | 15 | | ohc_1.455_zeolite-natrolite.fd.gz |
| 0 | 15 | | ohc_1.464_sulfate-bloedite.fd.gz |
| 0 | 15 | | ohc_1.469_sulfate-jarosite-k.fd.gz |
| 0 | 15 | | cmd.lib.setup.t5.2d5-group+basefilenames.txt |
| 0 | 15 | | ohc_1.471_sulfate-jarosite-k.fd.gz |
| 0 | 15 | | ohc_1.478_sulfate-jarosite-na90c.fd.gz |
| 0 | 15 | | ohc_1.479_sulfate-jarosite-na200c.fd.gz |
| 0 | 15 | | ohc_1.480_phyllo-prehnite.fd.gz |
| 1 | 4 | olivine | olivine_fo18_ki3377.fd.gz |
| 1 | 4 | olivine | olivine_fo60_ki3189.fd.gz |
| 1 | 4 | olivine | olivine_fo66_ki3054.fd.gz |
| 1 | 4 | olivine | olivine_fo80_ki3377.fd.gz |
| 1 | 4 | olivine | olivine_fo89_gds70.a.fd.gz |
| 1 | 4 | olivine | olivine_fo91_gds71.b.fd.gz |
| 0 | 10 | benzene | organic_3.237d_aromatic-benzene_cv.fd.gz |
| 1 | 2 | benzene; montmorillonite | organic_benzene+montswy.fd.gz |
| 1 | 0 | dry_grass | organic_dry_long_grass-thick.fd.gz |
| 1 | 2 | dry_grass | organic_drygrass+.17Na-mont.fd.gz |

**Table B1**
(Continued)

| Flag/Ignore: #comment<br>0 = ignore 1 = use-with-rover | Group (In Expert System) | Mineral(s) | Entry Name |
|---|---|---|---|
| 1 | 2 | fiberglass | organic_fiberglass-roofing.fd.gz |
| 1 | 1 | plastic | organic_green_plastic_tarp_1um.fd.gz |
| 1 | 0 | plastic | organic_green_plastic_tarp.fd.gz |
| 1 | 2 | paint | organic_paint-1.fd.gz |
| 1 | 2 | plastic | organic_plastic-hdpe.1.fd.gz |
| 1 | 2 | plastic | organic_plastic-pete.fd.gz |
| 1 | 2 | plastic | organic_plastic-pete2.fd.gz |
| 1 | 2 | plastic | organic_plastic-pete3.fd.gz |
| 1 | 2 | plastic | organic_plastic-pete4.fd.gz |
| 1 | 2 | plastic | organic_plastic-polystyrene.fd.gz |
| 1 | 2 | plastic | organic_plastic-tarp1.fd.gz |
| 1 | 2 | plastic | organic_plastic-vinyl.fd.gz |
| 1 | 2 | plastic | organic_plastic.grnhs.roof.fd.gz |
| 1 | 2 | tce; montmorillonite | organic_tce+montswy.fd.gz |
| 1 | 2 | toluene; montmorillonite | organic_toluene+montswy.fd.gz |
| 0 | 10 | aliphatic | organic_trace_3.42um_aliphatic1_curvc.fd.gz |
| 0 | 11 | aliphatic | organic_trace_aliphatic1.fd.gz |
| 1 | 2 | trichlor; montmorillonite | organic_trichlor+montswy.fd.gz |
| 1 | 2 | gas; montmorillonite | organic_unleaded.gas+montswy.fd.gz |
| 1 | 2 | dry_grass | organic_vegetation-dry-grass-golden.fd.gz |
| 1 | 2 | dry_grass | organic_vegetation-dry-grass-long.fd.gz |
| 1 | 2 | dry_wood | organic_vegetation-dry-wood.fd.gz |
| 1 | 0 | pvc | organic_white_pvc_pipe.fd.gz |
| 0 | 10 | pyridine | organic.3.24um.pyridine_curvc.fd.gz |
| 0 | 10 | nitrobenzene | organic.3.25um.nitrobenzene_curvc.fd.gz |
| 0 | 10 | pentene | organic.3.37um.pentene_curvc.fd.gz |
| 0 | 10 | nonyne | organic.3.41um.nonyne_curvc.fd.gz |
| 1 | 2 | palygorskite | palygorskite.fd.gz |
| 1 | 2 | perchlorate | perchlorate_mg.fd.gz |
| 1 | 2 | perchlorate | perchlorate_na.fd.gz |
| 1 | 2 | phlogopite | phlogopite.fd.gz |
| 1 | 2 | clintonite | phyllosilicate.clintonite.fd.gz |
| 1 | 2 | polyhalite | polyhalite.fd.gz |
| 1 | 2 | portlandite | portlandite.fd.gz |
| 1 | 2 | prehnite | prehnite.fd.gz |
| 1 | 2 | prehnite; chlorite | prehnite+.50chlorite.fd.gz |
| 1 | 2 | prehnite; chlorite | prehnite+.67chlorite.fd.gz |
| 1 | 2 | prehnite; chlorite | prehnite+.75chlorite.fd.gz |
| 1 | 2 | prehnite; chlorite | prehnite+muscovite.fd.gz |
| 1 | 2 | pyrophyllite; hydroth_pedogen_alunite | pyroph.5+alunit.5.fd.gz |
| 1 | 2 | pyrophyllite; montomorillonite | pyroph.5+mont0.5.fd.gz |
| 1 | 2 | pyrophyllite; muscovite | pyroph+musc.added.fd.gz |
| 1 | 2 | pyrophyllite; muscovite | pyroph+tr.musc.fd.gz |
| 1 | 2 | pyrophyllite | pyrophyllite.fd.gz |
| 1 | 5 | augite | pyroxene.augite.fd.gz |
| 1 | 5 | bronzite | pyroxene.bronzite.fd.gz |
| 1 | 5 | enstatite | pyroxene.enstatite.fd.gz |
| 1 | 5 | hypersthene | pyroxene.hypersthene.fd.gz |
| 1 | 4 | pigeonite | pyroxene.pigeonite.fd.gz |
| 1 | 1 | neodymium_oxide | ree_neodymium_oxide.fd.gz |
| 1 | 1 | samarium_oxide | ree_samarium_oxide.fd.gz |
| 1 | 2 | richterite | richterite.fd.gz |
| 1 | 2 | rivadavite | rivadavite.fd.gz |
| 1 | 4 | rutile | rutile_hs126.3b.fd.gz |
| 0 | 20 | samarium_oxide | samarium_oxide_compete.fd.gz |
| 0 | 22 | samarium_oxide | samarium_oxide1.fd.gz |
| 1 | 2 | saponite_or_talc | saponite.or.talc.fd.gz |
| 1 | 2 | sepiolite | sepiolite.fd.gz |
| 1 | 2 | chrysotile | serpentine_chrysotile.coarse-fibrous.fd.gz |
| 1 | 2 | chrysotile | serpentine_chrysotile.fine-fibrous.fd.gz |
| 1 | 2 | chrysotile | serpentine_chrysotile.med-fine-fibrous.fd.gz |
| 1 | 2 | cronstedtitte | serpentine_cronstedtite.fd.gz |

**Table B1**
(Continued)

| Flag/Ignore: #comment<br>0 = ignore 1 = use-with-rover | Group (In Expert System) | Mineral(s) | Entry Name |
|---|---|---|---|
| 1 | 2 | chalcedony | sioh_chalcedony.fd.gz |
| 1 | 2 | hydrated_basaltic_glass | sioh_hydrated_basaltic_glass.fd.gz |
| 1 | 2 | smectite; ammonillsmectite | smectite_ammonillsmec.fd.gz |
| 1 | 2 | beidellite | smectite_beidellite_gds123.fd.gz |
| 1 | 2 | beidellite | smectite_beidellite_gds124.fd.gz |
| 1 | 2 | montmorillonite | smectite_montmorillonite_ca_swelling.fd.gz |
| 1 | 2 | montomorillonite | smectite_montmorillonite_fe_swelling.fd.gz |
| 1 | 2 | montomorillonite | smectite_montmorillonite_na_highswelling.fd.gz |
| 1 | 2 | nontronite | smectite_nontronite_swelling.fd.gz |
| 1 | 0 | snow | snow.and.ice.fd.gz |
| 1 | 0 | snow | snow.melting.1a.fd.gz |
| 1 | 0 | snow | snow.melting.3.fd.gz |
| 1 | 0 | snow | snow.melting.8.fd.gz |
| 1 | 0 | snow | snow.melting16+0.5veg.fd.gz |
| 1 | 0 | snow | snow.melting1a+0.5veg.fd.gz |
| 1 | 0 | snow | snow.melting9+0.5veg.fd.gz |
| 1 | 0 | snow | snow.slush.16.fd.gz |
| 1 | 0 | snow | snow.slush.9.fd.gz |
| 1 | 4 | sphalerite | sphalerite_s26-341_1.5um.fd.gz |
| 1 | 2 | hydroth_pedog_alunite | sulfate_alun35K65Na.low.fd.gz |
| 1 | 2 | hydroth_pedog_alunite | sulfate_alun66K34Na.low.fd.gz |
| 1 | 2 | hydroth_pedog_alunite | sulfate_alun73K27Na.low.fd.gz |
| 1 | 2 | hydroth_pedog_alunite | sulfate_alunite_int-comp.all.fd.gz |
| 1 | 2 | hydroth_alunite | sulfate_alunite_k.all.fd.gz |
| 1 | 2 | hydroth_pedog_alunite | sulfate_alunite_na.all.fd.gz |
| 1 | 2 | hydroth_pedog_alunite | sulfate_alunNa03.fd.gz |
| 1 | 2 | hydroth_alunite | sulfate_alunNa56450c.fd.gz |
| 1 | 2 | hydroth_alunite | sulfate_alunNa78.450c.fd.gz |
| 1 | 2 | hydroth_alunite | sulfate_ammonalunite.fd.gz |
| 1 | 2 | ammonio_jarosite | sulfate_ammonjarosite.fd.gz |
| 1 | 2 | gypsum | sulfate_gypsum.fd.gz |
| 1 | 2 | jarosite | sulfate_jarosite-K.fd.gz |
| 1 | 2 | jarosite | sulfate_jarosite-lowT.fd.gz |
| 1 | 2 | jarosite | sulfate_jarosite-Na.fd.gz |
| 1 | 2 | hydroth_alunite | sulfate_kalun150c.fd.gz |
| 1 | 2 | hydroth_alunite | sulfate_kalun250c.fd.gz |
| 1 | 2 | hydroth_alunite | sulfate_kalun450c.fd.gz |
| 1 | 2 | kieserite | sulfate_kieserite.fd.gz |
| 1 | 1 | lazurite | sulfate_lazurite.fd.gz |
| 1 | 2 | mascagnite | sulfate_mascagnite.fd.gz |
| 1 | 2 | mirabilite | sulfate_mirabilite-wet_soil.fd.gz |
| 1 | 2 | hydroth_alunite | sulfate_na40alun400c.fd.gz |
| 1 | 2 | hydroth_alunite | sulfate_na63alun300c.fd.gz |
| 1 | 2 | hydroth_alunite | sulfate_na82alun100c.fd.gz |
| 1 | 2 | hydroth_alunite | sulfate_naalun150c.fd.gz |
| 1 | 2 | hydroth_alunite | sulfate_naalun300c.fd.gz |
| 1 | 2 | hydroth_alunite | sulfate_naalun450c.fd.gz |
| 1 | 2 | syngenite | sulfate_syngenite.fd.gz |
| 1 | 2 | szomolnokite | sulfate_szomolnokite_heated.fd.gz |
| 1 | 2 | szomolnokite | sulfate_szomolnokite.fd.gz |
| 1 | 2 | gypsum; jarosite; muscovite | sulfate-mix_gyp+jar+musc.amix.fd.gz |
| 1 | 2 | gypsum; jarosite; muscovite; dickite | sulfate-mix_gyp+jar+musc+dick.amix.fd.gz |
| 1 | 2 | gypsum; dust_WTC | sulfate-mix_gypsum.trace.dust+debris-WTC01-2.fd.gz |
| 1 | 2 | gypsum; dust_WTC | sulfate-mix_gypsum.trace.dust+debris-WTC01-28.fd.gz |
| 1 | 2 | gypsum; jarosite; illite | sulfate-mix_gypsum+jar+illite.intmix.fd.gz |
| 1 | 2 | kaolin; hydroth_pedogen_alunite; dickite | sulfate+kaolingrp_natroalun+dickite.fd.gz |
| 1 | 1 | cinnabar | sulfide_cinnabar.fd.gz |
| 1 | 1 | chalcopyrite | sulfide_copper_chalcopyrite.fd.gz |
| 1 | 1 | pyrite | sulfide_pyrite.fd.gz |
| 1 | 1 | sulfur | sulfur.fd.gz |
| 1 | 2 | talc | talc.all.fd.gz |
| 1 | 2 | talc | talc.crsgrnd.fd.gz |

**Table B1**
(Continued)

| Flag/Ignore: #comment<br>0 = ignore 1 = use-with-rover | Group (In Expert System) | Mineral(s) | Entry Name |
|---|---|---|---|
| 1 | 2 | talc | talc.fngrnd.fd.gz |
| 1 | 2 | talc; calcite | talc+calcite.parkcity.fd.gz |
| 1 | 2 | talc; calcite | talc+carbonate.parkcity.fd.gz |
| 1 | 2 | topaz | topaz.fd.gz |
| 1 | 2 | tremolite_or_talc | tremolite.or.talc.fd.gz |
| 1 | 2 | ulexite | ulexite.fd.gz |
| 0 | case-3 | vegetation | veg0.9um.band.fd.gz |
| 0 | case-4 | vegetation | veg1.2um.band.fd.gz |
| 0 | case-5 | vegetation | veg1.4um.band.fd.gz |
| 0 | 3 | vegetation | vegetation.dry_nonphotosyn.fd.gz |
| 1 | 0 | vegetation | vegetation.dry+green.fd.gz |
| 0 | 3 | vegetation | vegetation.dry+green.fd.gz |
| 0 | 3 | vegetation | vegetation.map.fd.gz |
| 0 | 3 | vegetation | vegetation.weak.map.fd.gz |
| 1 | 0 | vegetation | vegetation1.fd.gz |
| 0 | 19 | | water_1.896_beryl.fd.gz |
| 0 | 19 | | water_1.902_silica-opal.fd.gz |
| 0 | 19 | | water_1.903_smectite-saponite.fd.gz |
| 0 | 19 | | water_1.906_montmor-na.fd.gz |
| 0 | 19 | | water_1.907_smectite-nontronite.fd.gz |
| 0 | 19 | | water_1.908_phyllo-illite.fd.gz |
| 0 | 19 | | water_1.908_smectite-beidell.fd.gz |
| 0 | 19 | | water_1.909_mont-saz.fd.gz |
| 0 | 19 | | water_1.910_halloysite.fd.gz |
| 0 | 19 | | water_1.910_stonwplaya.fd.gz |
| 0 | 19 | | water_1.910_zeolite-clinopt.fd.gz |
| 0 | 19 | | water_1.910_zeolite-mordonite.fd.gz |
| 0 | 19 | | water_1.912_zeolite-analcime.fd.gz |
| 0 | 19 | | water_1.916_nesosil-sillim.fd.gz |
| 0 | 19 | | water_1.917_zeolite-heuland.fd.gz |
| 0 | 19 | | water_1.918_perchlorate-mg.fd.gz |
| 0 | 19 | | water_1.920_sulfate-bassanite.fd.gz |
| 0 | 19 | | water_1.923_chert.fd.gz |
| 0 | 19 | | water_1.924_perchlorate-na.fd.gz |
| 0 | 19 | | water_1.929_sulfate-epsomite.fd.gz |
| 0 | 19 | | water_1.931_narrow-cheatgrass.fd.gz |
| 0 | 19 | | water_1.932_sulfate-eusgterite.fd.gz |
| 0 | 19 | | water_1.940_zeolite-natrolite.fd.gz |
| 0 | 19 | | water_1.941_zeolite-natrolite.fd.gz |
| 0 | 19 | | water_1.941_zeolite-scolecite.fd.gz |
| 0 | 19 | | water_1.942_sulfate-schwert.fd.gz |
| 0 | 19 | | water_1.943_brick.fd.gz |
| 0 | 19 | | water_1.943_sulfate-gypsum.fd.gz |
| 0 | 19 | | water_1.944_sulfate-polyhalite.fd.gz |
| 0 | 19 | | water_1.946_sulfate-copiapite.fd.gz |
| 0 | 19 | | water_1.951_sulfate-bloedite.fd.gz |
| 0 | 19 | | water_1.960_sulfate-butler.fd.gz |
| 0 | 19 | | water_1.964_sulfate-feso4.fd.gz |
| 0 | 19 | | water_1.971_sulfate-kainite.fd.gz |
| 0 | 19 | | water_1.980_salt-carnallite.fd.gz |
| 0 | 19 | | water_1.981_sulfate-coquimb.fd.gz |
| 0 | 19 | | water_1.991_sulfate-syngite.fd.gz |
| 0 | 19 | | water_2.060_sulfate_szomoln.fd.gz |
| 0 | 19 | | water_2.073_sulfate-kieserite.fd.gz |
| 0 | 19 | | water_2.093_sulfate_szomoln.fd.gz |
| 0 | 19 | | water_2.122_nh4-buddingt.fd.gz |
| 0 | 19 | | water_2.130_sulfate_kieserite.fd.gz |
| 0 | 19 | | water_2.136_nh4-mascagnite.fd.gz |
| 0 | 19 | | water_broad_1.927_veg.fd.gz |
| 1 | 0 | water; chlorophyll | water.high.chlorophyll.fd.gz |
| 1 | 0 | water; chlorophyll | water.red.algae.fd.gz |
| 1 | 0 | water; montmorillonite | water+mont0.5gpl.fd.gz |

**Table B1**
(Continued)

| Flag/Ignore: #comment<br>0 = ignore 1 = use-with-rover | Group (In Expert System) | Mineral(s) | Entry Name |
|---|---|---|---|
| 1 | 0 | water; montmorillonite | water+mont1.67gpl.fd.gz |
| 1 | 0 | water; montmorillonite | water+mont16.5gpl.fd.gz |
| 1 | 0 | water; montmorillonite | water+mont5.01gpl.fd.gz |
| 1 | 2 | starkeyite | white.crust.starkeyite.fd.gz |
| 1 | 2 | analcime | zeolite_analcime.fd.gz |
| 1 | 2 | natrolite | zeolite_natrolite.fd.gz |
| 1 | 2 | zoisite | zoisite.fd.gz |
| 1 | 2 | zunyite | zunyite.fd.gz |
| 0 | 7 | goethite | goethite_3.17um |
| 0 | 7 | grossular | grossular_3.17um |
| 0 | 7 | jarosite | jarosite_3.18um |
| 0 | 8 | pyrophyllite | oh2.72um_ref_pyrophyllite |
| 0 | 8 | muscovite | oh2.75um_ref_muscovite_gds113 |
| 0 | 8 | illite | oh2.76um_ref_illite_gds4 |
| 0 | 8 | tourmaline | oh2.81um_ref_tourmaline |
| 0 | 8 | thenardite | oh2.83um_ref_thenardite |
| 0 | 8 | psilomelane | oh2.82um_ref_psilomelane |
| 0 | 10 | benzene | organic_3.237d_aromatic-benzene_curvc |
| 0 | 10 | aliphatic | organic_trace_3.42um_aliphatic1_curvc |
| 0 | 10 | calcite | carbonate_calcite_3.5um_curvc |
| 0 | 10 | dolomite | carbonate_dolomite_3.5um_curvc |
| 0 | 10 | carbonate | carbonate_trace_3.5um_curvc |
| 0 | 10 | carbonate | carbonate_trace-b_3.4um.curv |
| 0 | 10 | carbonate | carbonate_trace-c_3.4um.curvc |
| 0 | 10 | carbonate | carbonate_trace-c2b_3.4um.curvc |
| 0 | 10 | carbonate | carbonate_trace-calcdolo_3.4um.curvc |
| 0 | 10 | magnesite; hydromagnesite | carbonate_magnesite+hydromagnesite_curvc |
| 0 | 10 | niter | nitrate_niter_3.6um_curvc |
| 0 | 10 | co2_ice | co2_ice-on-moon62231.curvc |
| 0 | 10 | co2_ice | CO2_ice_g0.0300cm.curvc |
| 0 | 10 | co2_ice | CO2_ice_g0.1000cm.curvc |
| 0 | 10 | nonyne | organic.3.41um.nonyne_curvc |
| 0 | 10 | pentene | organic.3.37um.pentene_curvc |
| 0 | 10 | pyridine | organic.3.24um.pyridine_curvc |
| 0 | 10 | nitrobenzene | organic.3.25um.nitrobenzene_curvc |
| 0 | 10 | hydrogen_peroxide | hydrogen_peroxide.3.52um_curvc |
| 0 | 11 | benzene | organic_3.237d_aromatic-benzene_linc |
| 0 | 11 | aliphatic | organic_trace_aliphatic1_linc |
| 0 | 11 | calcite | carbonate_calcite_3.5um_linc |
| 0 | 11 | dolomite | carbonate_dolomite_3.5um_linc |
| 0 | 11 | carbonate | carbonate_trace_3.5um_linc |
| 0 | 11 | carbonate | carbonate_trace-b_3.4um_linc |
| 0 | 11 | carbonate | carbonate_trace-c_3.4um_linc |
| 0 | 11 | carbonate | carbonate_trace-c2b_3.4um.linc |
| 0 | 11 | carbonate | carbonate_trace-calcdolo_3.4um_linc |
| 0 | 11 | magnesite; hydromagnesite | carbonate_magnesite+hydromagnesite_linc |
| 0 | 11 | niter | nitrate_niter_3.6um_linc |
| 0 | 11 | co2_ice | co2_ice-on-moon62231_linc |
| 0 | 11 | co2_ice | CO2_ice_g0.0300cm_linc |
| 0 | 11 | co2_ice | CO2_ice_g0.1000cm_linc |
| 0 | 11 | nonyne | organic.3.41um.nonyne_linc |
| 0 | 11 | pentene | organic.3.37um.pentene_linc |
| 0 | 11 | pyridine | organic.3.24um.pyridine_linc |
| 0 | 11 | nitrobenzene | organic.3.25um.nitrobenzene_linc |
| 0 | 11 | hydrogen_peroxide | hydrogen_peroxide.3.52um_linc |
| 0 | 24 | calcite | carbonate_calcite_4um_linc |
| 0 | 24 | dolomite | carbonate_dolomite_4um_linc |
| 0 | 24 | ? | carbonate_trace_4um_linc |
| 0 | 24 | carbonate | carbonate_trace-b_4um_linc |
| 0 | 24 | carbonate | carbonate_trace-c_4um_linc |
| 0 | 24 | carbonate | carbonate_trace-calcdolo_4um_linc |
| 0 | 24 | magnesite; hydromagnesite | carbonate_magnesite+hydromagnesite_4umlinc |
| 0 | 24 | niter | nitrate_niter_4.1um_linc |

**Table B1**
(Continued)

| Flag/Ignore: #comment 0 = ignore 1 = use-with-rover | Group (In Expert System) | Mineral(s) | Entry Name |
|---|---|---|---|
| 0 | 26 | beryl | trapped-co2-4.24um_ref-beryl |
| 0 | 26 | cordierite | trapped-co2-4.26um_ref-cordierite |
| 0 | 26 | apatite | trapped-co2-4.265um_ref-apatite |
| 0 | 26 | microcline | trapped-co2-4.268um_ref-microcline |
| 0 | 26 | perthite | trapped-co2-4.272um_ref-perthite |
| 0 | 26 | apatite | trapped-co2-4.269um_ref-apatite |
| 0 | 26 | topaz | trapped-co2-4.31um_ref-topaz |
| 0 | 26 | sillimanite | trapped-co2-4.34um_ref-sillimanite |
| 0 | 27 | adularia | feldspar_adularia-4.5um |
| 0 | 27 | hydroth_pedogen_alunite | sulfate_alunite-na82-4.5um |
| 0 | 27 | hydroth_pedogen_alunite | sulfate_alunite-na83-4.5um |
| 0 | 27 | hydroth_pedogen_alunite | sulfate_alunite-na03-4.5um |
| 0 | 27 | hydroth_pedogen_alunite | sulfate_alunite–nh4-j-4.5um |
| 0 | 27 | hydroth_alunite | sulfate_alunite-400c-4.5um |
| 0 | 27 | hydroth_pedogen_alunite | sulfate_alunite-na56-4.5um |
| 0 | 27 | anhydrite | sulfate_anhydrite-4.5um |
| 0 | 27 | barite | sulfate_barite-4.5um |
| 0 | 27 | bassanite | sulfate_bassanite-4.5um |
| 0 | 27 | beidellite; montmorillonite | phyllosilicate_beidellite+montmor-4.5um |
| 0 | 27 | bloedite | sulfate_bloedite-4.5um |
| 0 | 27 | butlerite | sulfate_butlerite-4.5um |
| 0 | 27 | calcite | carbonate_calcite-4.67um |
| 0 | 27 | celestite | sulfate_celestite-4.5um |
| 0 | 27 | chabazite | zeolite_chabazitemix-4.5um |
| 0 | 27 | cyanide | cyanide_cyanide-cap-4.5um |
| 0 | 27 | cyanide | cyanide_cyanide-nik-4.5um |
| 0 | 27 | cyanide | cyanide_cyanide-znk-4.5um |
| 0 | 27 | dolomite | carbonate_dolomite-4.63um |
| 0 | 27 | elbaite | silicate_elbaite-4.5um |
| 0 | 27 | epsomite | sulfate_epsomite-4.5um |
| 0 | 27 | erionite | zeolite_erionitemix-4.5um |
| 0 | 27 | eugsterite | sulfate_eugsterite-4.5um |
| 0 | 27 | gypsum | sulfate_gypsum-4.5um |
| 0 | 27 | hematite; hematite_smallgrain | fe3+_hematite_a-4.5um |
| 0 | 27 | heulandite | zeolite_heulandite-4.5um |
| 0 | 27 | kainite | sulfate_kainite-4.5um |
| 0 | 27 | kieserite | sulfate_kieserite-4.5um |
| 0 | 27 | laumontite | zeolite_laumontite-4.5um |
| 0 | 27 | lepidolite | phyllosilicate_lepidolite-4.5um |
| 0 | 27 | magnesite; hydromagnesite | carbonate_magnesite-4.59um |
| 0 | 27 | mesolite | zeolite_mesolite-4.5um |
| 0 | 27 | mirabilite | sulfate_mirabilite-4.5um |
| 0 | 27 | natrolite | zeolite_natrolite-4.5um |
| 0 | 27 | natrolite | zeolite_natrolite-4.5um |
| 0 | 27 | polyhalite | sulfate_polyhalite-4.5um |
| 0 | 27 | rhodochrosite | carbonate_rhodochrosite-4.69um |
| 0 | 27 | sanidine | feldspar_sanidine-4.5um |
| 0 | 27 | scolecite | zeolite_scolecite-4.5um |
| 0 | 27 | sepiolite | phyllosilicate_sepiolite-4.5um |
| 0 | 27 | siderite | carbonate_siderite-4.65um |
| 0 | 27 | strontianite | carbonate_strontianite-4.70um |
| 0 | 27 | sngenite | sulfate_syngenite-4.5um |
| 0 | 27 | thenardite | sulfate_thenardite-4.5um |
| 0 | 27 | witherite | carbonate_witherite-4.74um |

### *B.2. Year 2 Geologic Origin Table B1/B2*

Tables B1 and B2 contain the geologic origin lookup table used in the second field expedition to the Yellow Cat Flat field site. Table B2 relates minerals to geologic origins.

**Table B2**
Geologic Origin Lookup Table Part 2—Year 2—Site 2

| Mineral(s) | Lacustrine/ Marine | Evaporitic/ Playa | Metamorphic | Hydrothermal | Pedogenic /Diagenic /Weathering (Include Secondary Coatings) | Igneous (Include Carbonatites) | Biogenic |
|---|---|---|---|---|---|---|---|
| actinolite | | | 1 | | | 1 | |
| adularia | | | | | | | |
| albite | | | 1 | 1 | | 1 | |
| aliphatic | | | | | | | |
| almandine | | | 1 | | | | |
| ammonillsmectite | | | | 1 | 1 | | |
| ammonio_jarosite | | | | 1 | 1 | | |
| amphibole | | | 1 | | | 1 | |
| analcime | | | | 1 | | 1 | |
| anorthite | | | | | | | |
| antigorite | 1 | 1 | 1 | | | | |
| augite | | | 1 | | | 1 | |
| axinite | | | | | | 1 | |
| azurite | | | | | 1 | | |
| beidellite | | | | | | | |
| benzene | | | | | | | |
| benzene; montmorillonite | | | | | | | |
| biotite | | | 1 | | | 1 | |
| bronzite | | | | 1 | | 1 | |
| brucite | | | 1 | 1 | 1 | | |
| buddingtonite | | | | 1 | | | |
| butlerite | | | | 1 | | | |
| bytownite | | | | | | 1 | |
| calcite | 1 | 1 | 1 | 1 | 1 | 1 | 1 |
| canallite | | 1 | | | | | |
| carbonate | 1 | 1 | 1 | 1 | 1 | | 1 |
| chalcedony | 1 | | 1 | 1 | | | |
| chalcopyrite | | | | 1 | | 1 | |
| chlorite | | | 1 | 1 | | | |
| chlorophyll | | | | | | | 1 |
| chromite | | | | | | 1 | |
| chrysocolla | | | | | 1 | | |
| chrysotile | | | 1 | 1 | | | |
| cinnabar | | | | 1 | | | |
| clinochlore | | | 1 | 1 | | | |
| clintonite | | | 1 | 1 | | | |
| clintonite | | | 1 | 1 | 1 | 1 | |
| colemanite | 1 | 1 | | | | | |
| cookeite | | | | | | 1 | |
| copiapite | | | | 1 | 1 | | |
| coquimbite | | | | | 1 | | |
| cronstedtitte | | | 1 | | | | |
| cummingtonite | | | 1 | | | | |
| cuprite | | | | | 1 | | |
| cyaniade | | | | | | | 1 |
| datolite | | | | 1 | | | |
| diaspore | | | | | 1 | | |
| dickite | | | | 1 | 1 | | |
| diopside | | | 1 | | | 1 | |
| dolomite | 1 | | | 1 | | | |
| dry_grass | | | | | | | 1 |
| dry_wood | | | | | | | 1 |
| dust_WTC | | 1 | | 1 | | | |
| elbaite | | | | | | 1 | |
| endellite | | | | 1 | 1 | | |
| enstatite | | | 1 | | | 1 | |
| epidote | | | 1 | | | | |
| eugsterite | | 1 | | | | | |
| Fe3+ | 1 | | 1 | 1 | 1 | 1 | |
| ferrihydrite | 1 | | | 1 | | | |
| fiberglass | | | | | | | |
| gas | | | | | | | |

**Table B2**
(Continued)

| Mineral(s) | Lacustrine/ Marine | Evaporitic/ Playa | Metamorphic | Hydrothermal | Pedogenic /Diagenic /Weathering (Include Secondary Coatings) | Igneous (Include Carbonatites) | Biogenic |
|---|---|---|---|---|---|---|---|
| gibbsite | | | | 1 | 1 | | |
| goethite | 1 | | | 1 | 1 | | |
| grossular | | | 1 | | | | |
| gypsum | | 1 | | 1 | 1 | | |
| halloysite | | | | 1 | | | |
| hectorite | 1 | | | | 1 | | |
| hedenbergite | | | 1 | | | | |
| hematite | | | | 1 | 1 | | |
| hematite_smallgrain | | | | 1 | 1 | | 1 |
| hornblende | | | 1 | | | 1 | |
| howlite | | 1 | | | | | |
| hydrated_basaltic_glass | | | | | | 1 | |
| hydroth_alunite | | | | 1 | | | |
| hydroth_pedog_alunite | | | | 1 | 1 | | |
| hypersthene | | | | | | 1 | |
| illite | | | 1 | 1 | | | |
| jadeite | | | 1 | | | | |
| jarosite | 1 | 1 | | 1 | 1 | | |
| kaolinite | | | | 1 | 1 | | |
| kaolinite | 1 | | | 1 | 1 | | |
| kieserite | | 1 | | | 1 | | |
| lazurite | | | 1 | | | | |
| lepidocrosite | 1 | | | 1 | 1 | | |
| lepidolite | | | | 1 | | 1 | |
| lizardite | | | | | | | |
| maghemite | | | 1 | | | | |
| magnesite | | | 1 | 1 | 1 | | |
| magnesite; hydromagnesite | | | 1 | 1 | 1 | | 1 |
| malachite | | | 1 | | 1 | | |
| manganese | | | | | 1 | | 1 |
| margarite | | | | | 1 | | |
| mascagnite | | | | 1 | | | |
| microcline | | | | | | 1 | |
| mirabilite | | 1 | | | | | |
| montmorillonite | 1 | | | 1 | 1 | | |
| muscovite | | | 1 | 1 | | 1 | |
| nacrite | | | | 1 | 1 | | |
| natrolite | | | | | | 1 | |
| neodymium_oxide | | | | | 1 | 1 | |
| niter | | | | | 1 | | |
| nitrate | | | | | | | |
| nitrobenzene | | | | | | | |
| nontronite | 1 | | | 1 | 1 | | |
| nonyne | | | | | | | |
| olivine | | | | | | 1 | |
| orthoclase | | | | | | 1 | |
| paint | | | | | | | |
| palygorskite | 1 | | | | 1 | | |
| paragonite | | | 1 | | | | |
| pectolite | | | | 1 | | | |
| pentene | | | | | | | |
| perchlorate | | 1 | | | | | |
| peroxide | | | | | | | |
| phlogopite | | | 1 | 1 | | 1 | |
| pigeonite | | | | | | 1 | |
| pinnoite | 1 | 1 | | | | | |
| pitchlimonite | | | | | 1 | | |
| plastic | | | | | | | |
| polyhalite | | 1 | | | | | |
| portlandite | | 1 | 1 | 1 | | | |
| prehnite | | | | 1 | | | |

**Table B2**
(Continued)

| Mineral(s) | Lacustrine/ Marine | Evaporitic/ Playa | Metamorphic | Hydrothermal | Pedogenic /Diagenic /Weathering (Include Secondary Coatings) | Igneous (Include Carbonatites) | Biogenic |
|---|---|---|---|---|---|---|---|
| propylzone | | | | 1 | 1 | | |
| pvc | | | | | | | 1 |
| pyridine | | | | | | | |
| pyrite | | | 1 | | 1 | 1 | |
| pyrolusite | 1 | | | | 1 | | |
| pyrophyllite | | | 1 | 1 | | | |
| quartz | | | | 1 | | 1 | |
| rhodochrosite | | | | 1 | | | |
| rhodonite | | | 1 | 1 | | | |
| richterite | | | 1 | 1 | | | |
| riebeckite | | | 1 | 1 | | | |
| rivadavite | | 1 | | 1 | | | |
| roscoelite | | | | 1 | 1 | | |
| rutile | | | | | | 1 | |
| samarium_oxide | | | | | 1 | 1 | |
| saponite | 1 | | | 1 | 1 | | |
| saponite_or_talc | 1 | | | 1 | 1 | | |
| schwertmannite | | | | | 1 | | |
| sepiolite | | 1 | | | | | |
| serpentine | | | 1 | 1 | | | |
| siderite | | 1 | | 1 | 1 | | |
| smaragdite | | | 1 | | | 1 | |
| smectite | 1 | 1 | 1 | 1 | 1 | | |
| snow | | | | | | | |
| sphalerite | | | | 1 | | 1 | |
| starkeyite | | 1 | | | | | |
| staurolite | | | 1 | | | | |
| strontinite | | | | 1 | | | |
| sulfur | | | 1 | | | 1 | 1 |
| syngenite | 1 | 1 | 1 | | 1 | | 1 |
| szomolnokite | 1 | | | | 1 | | |
| talc | | | 1 | 1 | | | |
| tce | | | | | | | |
| thuringite | | | 1 | 1 | | | |
| toluene | | | | | | | |
| topaz | | | | | | 1 | |
| tremolite | | | 1 | | | | |
| tremolite_or_talc | | | 1 | | | | |
| trichlor; montmorillonite | | | | | | | |
| ulexite | | 1 | | | | | |
| uralite | | | 1 | | | 1 | |
| vegetation | | | | | | | 1 |
| water | | | | | | | |
| witherite | | | | 1 | | | |
| wollastonite | | | 1 | | | | |
| zoisite | | | 1 | | | | |
| zunyite | | | 1 | 1 | | | |

## ORCID iDs

Amanda Hendrix https://orcid.org/0000-0002-0435-8224
Nandita Kumari https://orcid.org/0000-0001-5960-0914
Melissa D. Lane https://orcid.org/0000-0003-3264-3337
Audrey Martin https://orcid.org/0000-0003-3402-1339
Neil Pearson https://orcid.org/0000-0002-0183-1581
Faith Vilas https://orcid.org/0000-0003-4723-5870

## References

Bell, J. F., Squyres, S. W., Herkenhoff, K. E., et al. 2003, JGRE, 108, 8063
Bell, T. 1986, in A Basin Analysis Case Study: The Morrison Grants Uranium Region New Mexico, ed. C. E. Turner-Peterson, E. S. Santos, & N. S. Fishermen (Tulsa, OK: American Association of Petroleum Geologists)
Cabrol, N. A., Wettergreen, D., Warren-Rhodes, K., et al. 2007, JGRG, 112, G04S02
Candela, A., Kodgule, S., Edelson, K., et al. 2020, Planetary Rover Exploration Combining Remote and In Situ Measurements for Active Spectroscopic Mapping, in IEEE Int. Conf. on Robotics and Automation (ICRA) (Piscataway, NJ: IEEE)
Candela, A., Thompson, D. R., Noe Dobrea, E. Z., & Wettergreen, D. S. 2017, in IEEE Int. Conf. on Intelligent Robots and Systems (IROS) (Piscataway. NJ: IEEE)
Cheevers, C. W., & Rawson, R. R. 1979, Four Corners Geological Society 9th Field Conf. Guidebook, Publications of the Society: 1952 to 2010 (Durango, CO: Four Corners Geological Society), 105, https://archives.datapages.com/data/fcgs/data/015/015001/105_four-corners150105.htm
Clark, R. N. 2024, PSI-edu/spectroscopy-tetracorder: Tetracorder 5.27 with expert systems to 5.27e + specpr, spectral libraries, and radiative transfer models, v5.27.0, Zenodo, doi:10.5281/zenodo.11204505
Clark, R. N., Green, R. O., Swayze, G. A., et al. 2001, U.S. Geological Survey Open File Report OFR-01-0429, U.S. Geological Survey, https://pubs.usgs.gov/of/2001/ofr-01-0429/
Clark, R. N., Swayze, G. A., Livo, K. E., et al. 2003, JGRE, 108, 5131
Clark, R. N., Swayze, G. A., Livo, K. E., et al. 2024, Imaging Spectroscopy: Earth and Planetary Remote Sensing with the PSI Tetracorder and Expert Systems from Rovers to EMIT and Beyond, PSJ, 5, 276
Clark, R. N., Swayze, G. A., Murchie, S. L., et al. 2015, LPSC, 46, 2410
Clark, R. N., Swayze, G. A., Murchie, S. L., et al. 2016, LPSC, 47, 2900
Clark, R. N., Swayze, G. A., Wise, R., et al. 2007, USGS Digital Spectral Library splib06a, U.S. Geological Survey, Data Series, doi:10.3133/ds231
Colaprete, A., Elphic, R. C., Shirley, M., et al. 2023, LPSC, 54, 2910
Doelling, H. H., & Kuehne, P. A. 2013, Geologic Map of the Mollie Hogans Quadrangle, Grand County, Utah, Utah Geological Survey, Map 259DM, https://ngmdb.usgs.gov/Prodesc/proddesc_100871.htm
Green, R. O., Eastwood, M. L., Sarture, C. M., et al. 1998, RSEnv, 65, 227
Hanson, S. L. 2006, Western National Parks Assn. Research 06-11, Adrian College, https://npshistory.com/publications/wupa/lava-flows.pdf
Harshbarger, J. W., Repenning, C. A., & Irwin, J. H. 1958, Stratigraphy of the Uppermost Triassic and Jurassic Rocks of the Navajo Country, in Guidebook of the Black Mesa Basin, Northeastern Arizona: New Mexico Geological Society Guidebook, 9th Field Conf., ed. R. Y. Anderson & J. W. Harshbarger (Socorro, NM: New Mexico Bureau of Mines and Mineral Resources), 98, https://pubs.usgs.gov/pp/0291/report.pdf
Haynes, D. D., & Hackman, R. J. 1978, Geology, Structure, and Uranium Deposits of the Marble Canyon 1 Degree x 2 Degrees Quadrangle, Arizona, U.S. Geological Survey Miscellaneous Investigations Series Map I–1003, U.S. Geological Survey
Hock, A. N., Cabrol, N. A., Dohm, J. M., et al. 2007, JGRG, 112, G04S08
Hutengs, C., Ludwig, B., Jung, A., Eisele, A., & Vohland, M. 2018, Senso, 18, 993
Joeckel, R. M., Suarez, C. A., McLean, et al. 2023, Geosc, 13, 32
Kirk, A. R., & Condon, S. M. 1986a, in Basin Analysis Case Study: The Morrison Formation, Grants Uranium Region, New Mexico, ed. C. E. Turner-Peterson, E. S. Santos, & N. S. Fishman (Tulsa, OK: The American Association of Petroleum Geologists), 110, https://pubs.usgs.gov/imap/1957a/report.pdf
Kirk, A. R., & Condon, S. M. 1986b, USGS Miscellaneous Investigations Series Maps I-1957-A, -B, -C, -D, U.S. Geological Survey
McKee, E. D. 1938, The Environment and History of the Toroweap and Kaibab Formations on Northern Arizona and Southern Utah, Carnegie Institute of Washington Publication, 492, 268, https://ci.nii.ac.jp/ncid/BA39460884?l=en
McKee, E. D. 1954, GSAMm, 61, 133
Prettyman, T. H., Buxner, S., Steckel, A. V., et al. 2023, LPSC, 54, 1389
Siegler, M., Paige, D., Williams, J-P., & Bills, B. 2015, Icar, 255, 78
Siegler, M. A., Martinez-Camacho, J., Paige, D. A., P., J., et al. 2022, High Resolution Models of Polar Ice Stability, in Lunar Polar Volatiles Conf. 2703, 5025
Shoemaker, E. M. 1960, PhD thesis, Princeton Univ.
Squyres, S. W., Arvidson, R. E., Baumgartner, E. T., et al. 2003, JGRE, 108, 8062
Thompson, D. R., Candela, A., Wettergreen, D. S., et al. 2018, AsBio, 18, 934
Thompson, D. R., Wettergreen, D. S., & Peralta, F. J. C. 2011, Journal of Field Robotics, 28, 542
Ulrich, G. E., & Bailey, N. G. 1987, U.S. Geologic Survey Miscellaneous Field Studies Map MF-1956, U.S. Geologic Survey, https://ngmdb.usgs.gov/Prodesc/proddesc_5526.htm
Wagner, M., Heys, S., Wettergreen, D., et al. 2005, in The 8th Int. Symp. on Artificial Intelligence, Robotics and Automation in Space (i-SAIRAS 2005), ESA SP-603, ed. B. Battrick, 5
Wettergreen, D. S., Cabrol, N. A., Whittaker, W., et al. 2005, LPSC, 36, 2316